UNDERSTANDING THE INFLUENCE OF UNDERCOOLING AND ATOMIC
ORDERING ON THE EMERGING PROPERTIES OF MARGINAL METALLIC
GLASSES

A THESIS SUBMITTED TO
THE GRADUATE SCHOOL OF NATURAL AND APPLIED SCIENCES
OF
MIDDLE EAST TECHNICAL UNIVERSITY

BY

CAN OKUYUCU

IN PARTIAL FULFILLMENT OF THE REQUIREMENTS
FOR
THE DEGREE OF MASTER OF SCIENCE
IN
METALLURGICAL AND MATERIALS ENGINEERING

AUGUST 2023

Approval of the thesis:

UNDERSTANDING THE INFLUENCE OF UNDERCOOLING AND ATOMIC ORDERING ON THE EMERGING PROPERTIES OF MARGINAL METALLIC GLASSES

submitted by **CAN OKUYUCU** in partial fulfillment of the requirements for the degree of **Master of Science in Metallurgical and Materials Engineering, Middle East Technical University** by,

Prof. Dr. Halil Kalıpçılar
Dean,
Graduate School of **Natural and Applied Sciences** _____

Prof. Dr. Ali Kalkanlı
Head of the Department,
Metallurgical and Materials Engineering, METU _____

Prof. Dr. Yunus Eren Kalay
Supervisor,
Metallurgical and Materials Engineering, METU _____

Examining Committee Members:

Prof. Dr. Benat Koçkar
Mechanical Engineering, Hacettepe University _____

Prof. Dr. Yunus Eren Kalay
Metallurgical and Materials Engineering, METU _____

Assoc. Prof. Dr. Sezer Özerinç
Mechanical Engineering, METU _____

Assist. Prof. Dr. Eda Aydoğan Güngör
Metallurgical and Materials Engineering, METU _____

Assist. Prof. Dr. Irmak Sargın
Metallurgical and Materials Engineering, METU _____

Date: 07.08.2023

I hereby declare that all information in this document has been obtained and presented in accordance with academic rules and ethical conduct. I also declare that, as required by these rules and conduct, I have fully cited and referenced all material and results that are not original to this work.

Name, Surname: Can Okuyucu

Signature:

ABSTRACT

UNDERSTANDING THE INFLUENCE OF UNDERCOOLING AND ATOMIC ORDERING ON THE EMERGING PROPERTIES OF MARGINAL METALLIC GLASSES

Okuyucu, Can
Master of Science, Metallurgical and Materials Engineering
Supervisor: Prof. Dr. Yunus Eren Kalay

August 2023, 107 pages

Marginal metallic glasses are a new and exciting field of study under materials science and solid-state physics. The physical laws and thermodynamics behind their first formation and emerging properties have attracted scientists for years. This study mainly focuses on the atomic ordering of the amorphous, liquid, and devitrified amorphous/crystalline phases. The influence of medium-range order and undercooling on different atomic configurations were investigated in detail. The physical and chemical properties of these alloys were investigated by advanced characterization methods. The model system to investigate these effects was chosen as Al-RE alloys. Structural and chemical reasonings for the emerging properties of Al-based marginal metallic glass formers were intensely discussed. Crystallization kinetics during devitrification was examined by thermal analyses. The mechanical property enhancement of Al-RE alloys was investigated by nanomechanical and analytical electron microscopy characterizations. At the end of this study, the correlation between atomic ordering and physical properties has been tried to be enlightened.

Keywords: Metallic Glass, Al-RE Alloys, Characterization, Medium-Range Order

ÖZ

AŞIRI SOĞUTMA VE ATOMİK DÜZENLERİN MARJİNAL METALİK CAMLARDA ORTAYA ÇIKAN ÖZELLİKLER ÜZERİNDEKİ ETKİLERİNİ ANLAMAK

Okuyucu, Can
Yüksek Lisans, Metalurji ve Malzeme Mühendisliği
Tez Yöneticisi: Prof. Dr. Yunus Eren Kalay

Ağustos 2023, 107 sayfa

Marjinal metalik camlar, malzeme bilimi ve katı hal fiziği alanlarında yeni ve heyecan verici bir araştırma konusudur. İlk oluşumları ve ortaya çıkan özelliklerinin arkasındaki fiziksel yasalar ve termodinamik, yıllardır bilim insanlarının ilgisini çekmektedir. Bu çalışma, temel olarak amorf, sıvı ve devitrifiye amorf/kristal fazların atomik düzenlerine odaklanmıştır. Orta menzilli düzen ve aşırı soğutmanın farklı atomik yapılar üzerindeki etkisi detaylı olarak araştırılmıştır. Bu alaşımlarıdaki fiziksel ve kimyasal özellikler ileri karakterizasyon yöntemleriyle incelenmiştir. Bu etkileri araştırmak için model sistem olarak Al-NTE alaşımları seçilmiştir. Al bazlı marjinal metalik cam oluşturucularında ortaya çıkan özelliklere ilişkin yapısal ve kimyasal gerekçeler yoğun bir şekilde tartışılmıştır. Devitrifikasyon sırasındaki kristalleşme kinetiği termal analizlerle incelenmiştir. Al-NTE alaşımlarında mekanik özelliklerin artışı nanomekanik ve analitik elektron mikroskopi karakterizasyonlarıyla araştırılmıştır. Bu çalışmanın sonunda, atomik düzen ve fiziksel özellikler arasındaki ilişki aydınlatılmaya çalışılmıştır.

Anahtar Kelimeler: Metalik Cam, Al-NTE Alaşımları, Karakterizasyon, Orta Erim Düzeni

Dedicated to my dear family…

ACKNOWLEDGMENTS

There are uncountably many people and things that bring this road today. As it is, I would like to give my deep appreciation and acknowledgment to some of them. First and foremost, I would like to express my most profound gratitude to Prof. Dr. Yunus Eren Kalay, who led the way in this research. I always see him as a role model and a great mentor. During this journey, he is always the person I would like to be and hopefully surpass someday, as it should be in the case of an ideal master-apprentice relationship. His idealism, mentoring, and passion for research and science communication will always continue to amaze me and lead the way.

The road would not be this fun without my precious fellow labmates. My first appreciation is to Doğuhan Sarıtürk, who is in the high-performance computing part of this project. Our dozens of nights-long discussions will be remembered. One who always has enough energy to motivate around, Fatma Saadet Güven, deserves another standalone acknowledgment. Our countless study and fun events with the previous undergraduates, yet the current friends, Sabri Ufuk Arısan and Zeynep Ege Uysal, also deserve appreciation. It would be missed if I did not mention my dear previous labmates Tolga Han Ulucan, Gökhan Polat, Emel Erdal, Fatih Sıkan, Bengisu Yaşar Sarı, Anıl Erdal, and Mustafacan Kutsal. I should also express my deep appreciation to all the inspiring professors, specialists, technicians, and personnel of my department and university.

I could not achieve and continue this journey without my lovely family. They are the ones who made me who I am. Most people think they have a great family. Yet, maybe

TABLE OF CONTENTS

LIST OF TABLES

Tables

LIST OF FIGURES

Figures

xiv

xv

xvi

CHAPTER 1

INTRODUCTION

Thousands of years ago, when Thales started to search for the meanings of natural phenomena occurring around us, the first seeds of philosophy sprouted. He gave the highest importance to *logos* rather than *mythos*. Upon that time, philosophy evolved into alchemy. Chemistry followed, and other fundamental scientific fields came next. Engineers entered the stage when the clock shows the ancient era and started to invent things for human favor. The major disciplines were chemical, civil, mechanical, and electrical engineering. They are all glued with interdisciplinary fields, such as metallurgical and materials engineering. Names of prehistorical periods like the Stone, Bronze, and Iron Ages prove the importance of materials engineering. From those years to these decades, metallurgists and materials engineers have studied the materials around us and tried understanding the structure and property relationships along all unit scales. From conventional steels and ceramics to advanced optophotonic materials, this field conducts research on the materials at the edge of the current scientific knowledge.

The marginal metallic glasses are one of the most exciting materials set for today's solid-state scientists. Their atomic arrangements and microstructural evolutions are new, and their corresponding behaviors are promising for engineering applications. However, their metastable nature limits the widespread usage of these metals. For these reasons, this thesis will focus on cutting-edge findings on marginal metallic glass systems. Some yet-unexplained features of these metals will be tried to be cleared by logos, just like the path of Thales.

1.1 Understanding the Materials Tetrahedron

Materials science starts with the well-known materials tetrahedron. It gives all the required definitions of materials engineering – structure, property, performance, processing, and characterization in the core (Figure 1.1). While engineering mostly lies along the performance and processing sides, science focuses mainly on structure and property. But all the lines and corners are alive, thanks to the characterization core.
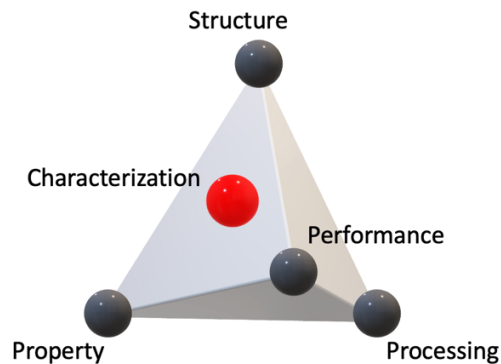
Figure 1.1 Materials tetrahedron

As this thesis will cover all the aspects of marginal glass, characterization will be the backbone of the study. In each step, the paths along corners will be connected using characterization.

1.2 Amorphous Metals

Metallic glass, i.e., amorphous metal, is a metal that lacks long-range order. The atoms within the material do not show any periodicity or regular arrangement. Since it has no crystal structure, it also has no crystalline defects. This disordered nature gives superior mechanical properties considering their crystalline counterparts. For example, no plastic deformation is observed in their structure, and these metals can

exhibit their theoretical strength values. They generally have higher hardness, strength, toughness, elasticity, and corrosion resistance. Also, controlled devitrification may further enhance their mechanical properties.

The term "amorphous metal" usually represents the alloys whose nucleation and growth routes were suppressed during solidification and metastably frozen into an utterly disordered state, i.e., a glassy state. They gain tremendous viscosity increment during this rapid cooling. They also exhibit a glass transition temperature, just like traditional glassy materials, and their amorphous solid forms usually have a viscosity of around 10^{12} Pa.s.

1.2.1 History of Metallic Glasses

The first examples of metallic glasses were brought into the stage in the middle of the 20th century. One of the first recognizable studies of those years came from the California Institute of Technology in 1960. For the first time in history, Klement, Willens, and Duwez produced an amorphous gold-silicon alloy [1]. They published their findings in a half-page-long paper in Nature. For those times, the highly disordered configuration was only seen in some thin films deposited at very low temperatures. Hence, the findings of Klement et al. drew the attention of other scientists. Turnbull et al. followed this initial study with the discovery of thermal evidence of glass transition in the Au-Si-Ge system for the first time [2]. A year after, they also found evidence of glass transition in the Au-Ge-Si system [3]. Later, they developed a series of Pd-Si-X (X= Ag, Cu, Au) amorphous alloys with relatively low cooling rates of 10^2 K/sec and thickness values of more than 0.5 mm [4].

One of the drawbacks of metallic glasses was the maximum possible thickness of the produced materials since the production requires rapid solidification techniques to bypass the nucleation and growth during solidification. However, even in those years, scientists started to obtain higher thicknesses by modifying the composition of the desired materials thermodynamically and achieving better production routes.

Turnbull and his group produced a series of Pd-P-X (X = Ni, Co, Fe) amorphous metals with thickness values around 1 mm [5].

Parallel to the extension of our understanding of the thermodynamical insight of the production and evolution of metallic glasses, Ruhl et al. developed several amorphous Nb-Ni and Ta-Ni alloys with splat quenching technique and found that one can produce metallic glass with other elements than the metalloid group of periodic table [6].

After successful experimentations in Turnbull's group, Chen and Miller produced metallic glasses with another rapid cooling technique called centrifugal spinning [7,8]. Two other scientists who developed and optimized the same process for those years were Liebermann and Graham [9]. They also studied the optimization of the produced ribbons by centrifugal spinning. This method has gained importance over the years. It is still one of the most preferred techniques to obtain a glassy metal for different sets of compositions with different production parameters, such as cooling rates of 10^6 K/sec, and with different properties. This technique nowadays is mainly referred to as melt spinning, and the produced materials were identified as melt-spun ribbons.

For years, numerous scientists have observed metallic glass formation and glass transition for their systems. Such scientists include Inoue, Egami, Kendall, Kelton, Napolitano, and Voyles. Year by year, they tried to understand the fundamentals of glass formation, enhance the properties of these materials, characterize them, and increase the maximum possible volume of the final product to fit these materials into suitable applications. One of the first commercially usable patented bulk metallic glasses (BMG) used in real-life applications was the Vitreloy 1, an alloy composed of Zr, Ti, Cu, Ni, and Be. This material family is first introduced in the paper written by Peker and Johnson [10]. As of today, several metallic glasses can be produced and used in bulk, including this material family.

Recently, alloy systems suitable for the glassy state are started to be developed with the contribution of artificial intelligence (AI). In 2018, a combined study by scientists

from Stanford's SLAC, NIST, and several universities like Northwestern published an article on the impact of AI on the design of glassy metals [11]. They have reported that they could analyze 2000 potential alloy systems per day. One can compare the fact that it took around three days to make all the experimentations on the literature on metallic glass from its foundation, which is around fifty years of progress.

1.2.2 Production Methods

As mentioned above, the critical cooling rate requirement of up to millions of degrees per second is necessary to produce marginal metallic glass. The most used methods to achieve such cooling rates are usually melt spinning, splat quenching, gas atomization, magnetron sputtering, laser ablation, and sometimes high-energy ball milling, depending on the precursor state. Each method has its own advantages and disadvantages, which will not be covered during this study. However, several examples can be given, such as one almost always cannot avoid the nanocrystalline formation beside the amorphous state with mechanical milling or the composition of the produced amorphous metals will most likely shift from the desired one with laser ablation since the precursor plasma state during production is forming locally depending on the focus of the laser.

The main factor to consider for all the abovementioned methods is always the critical cooling rate to achieve enough viscosity increment for freezing and suppressing the nucleation. But, among others, mechanical milling has some other important factors than the cooling rate since the precursor state is also solid.

A fundamental approach to obtaining a glassy metal is centrifugal spinning, i.e., melt spinning. The detailed production pathway can be seen below (Figure 1.2). In melt spinning, a melt is usually produced by induction coils in a controlled atmosphere. A water-cooled metal wheel, usually copper, is placed under the feeding system. The centrifugal forces create a tangential speed on the touching zone of the wheel to the melt coming from the induction coils at the orders of tens of meters per second. The

cooling rate and the amount of undercooling are optimized by changing the tangential speed of the wheel. In the end, the melt-spun material solidifies rapidly in the form of ribbons that are thrown by the high-speed wheel.
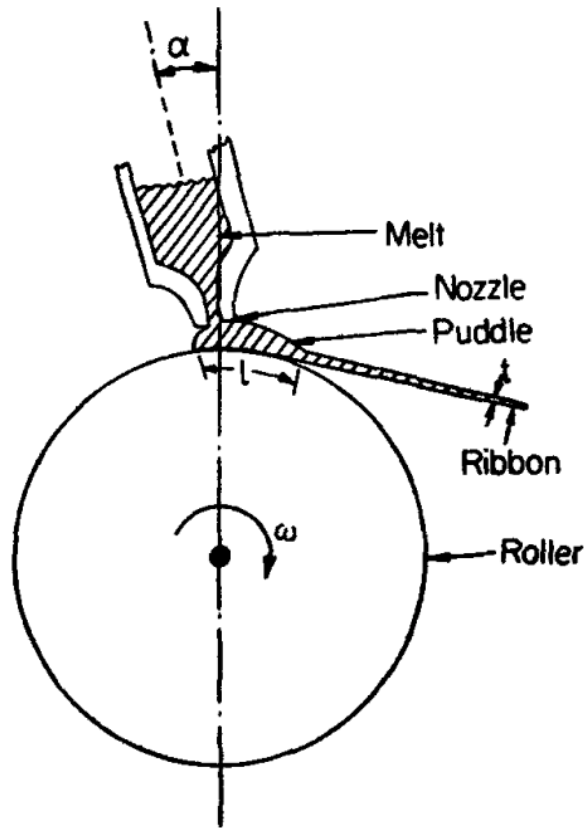
Figure 1.2 Schematic of a melt spinning procedure. Adopted from [12]

1.2.3   Application Areas and Future Potentials

Bulk metallic glasses are currently used in a variety of applications. These can be counted as high-efficiency transformers due to their low magnetization loss, flowmeters due to their high corrosion resistance and mechanical properties, and pressure sensors for the automobile industry due to their sensitivities to the signals and pressure endurance. Also, they are used in different sports equipment such as golf clubs, the inner core of golf balls, softball and baseball bats, tennis racquets, and skis. Several electronic devices have metallic glass casings, considering their high

wear resistance. Moreover, their wear-resistance properties make it possible to use them as a coating to protect the power plant boiler tubes and petroleum drill pipes.

Although the mass production and shaping challenges draw back the wide usage of these promising alloys, their combination of excellence at different properties attracts attention for their use in aerospace and military applications. Nowadays, they are implemented for the kinetic energy penetrators of military vehicles as a replacement for depleted uranium. They are also used for the solar wind ion collectors of NASA's space probes. As of today, scientists are trying to overcome all these challenges for the production and stability of metallic glasses with enormous funding from different scientific and military purpose agencies.

Rather than directly implementing glassy metals into different products and applications, these alloys hide the potential to contribute to the theoretical knowledge of humans to understand the nature surrounding us. Their first formations are a thermodynamical challenge since the viscosity increment must overcome the rate of nucleation and growth. The Gibbs free energy required for these processes, the role of thermal and kinetic undercooling, their different short to medium-range ordered amorphous configurations, and the number crystal density for their devitrified products are the subjects that still need further explanations. Solutions to these different topics may favor the invention of yet-unimaginable applications. For example, a fair basis for the millions of orders of magnitude higher nucleation density for their first devitrification product, compared with the predictions of classical nucleation theory (CNT), can enhance our understanding of the nucleation phenomena in atomistic scale. From water harvesting devices in deserts to cancer formation in the human body, up to the stellar objects, somehow, they all start with nucleation. As one can realize, the future and the potential for investigations focused on amorphous metals are all tremendous and exciting.

1.3 Thermodynamics and Kinetics of the Metallic Glass Formation

The key to obtaining an utterly disordered metal is bypassing the crystallization event during solidification. These methods usually need higher cooling rates than conventional production methods. Depending on the composition, metallic glass can be produced within a cooling range of tens of K/s to millions of K/s. The main factor in determining the critical cooling rate requires a comprehensive understanding of solidification thermodynamics and kinetics. The thermodynamic and kinetics perspective will be covered later in this thesis. Yet, several studies are in the literature on the glass formation ability (GFA) of metals. The fundamental coverage of the empirical rules to obtain a glassy metal is first listed by Inoue [13,14]. The Inoue criteria suggest negative heat of mixing between components, atomic size mismatch above 12% for the constituent elements, and a multicomponent system containing more than three elements.

A semi-quantitative approach is developed by Cohen and Turnbull to determine the GFA of systems [15]. They argued that all liquids, including ionic and metallic liquids, have increased glass formation tendency while the reduced melting temperature is decreasing. They also propose that the increased amount of impurity content also depresses the reduced melting temperature, thus, improving glass-forming tendency due to the molecular asymmetrization. The reduced melting temperature is defined as

$$\tau_m = \frac{kT_m}{h_v}$$

where T_m is the thermodynamic crystallization temperature, and h_v is the molecular heat of vaporization. The findings revealed a rule of thumb for the glass-forming tendency. It means that the alloys near eutectic regions, in terms of their compositions, have lower τ_m, thus, greater GFA. They also suggest an idea for the stability of these alloys against crystallization. They explained that the crystallization of a eutectic material requires chemical diffusive motion over several atomic

diameters, while pure metals require an atomic motion at less than one atomic diameter. In terms of these findings, the GFA is also getting higher for the low melting eutectics.

Turnbull also suggested a quantitative parameter called reduced glass transition temperature, $T_{rg} = T_g/T_m$, to determine the GFA. The glass-forming tendency increases with the reduced glass transition temperature [16]. Turnbull also proposed that the viscosity must increase very rapidly within the transition from liquid to glass at some temperature. Within these studies, Turnbull was able to calculate the required amount of cooling rates for the alloys to achieve necessary undercooling, thus, enough viscosity increment that yields greater glass-forming ability with respect to the reduced glass transition temperature.

Therefore, the competition of nucleation rate and viscosity increment during rapid solidification is the determining factor for the glass formation ability of an alloy. The nucleation of a random cluster can be either in the form of homogeneous or heterogeneous. During nucleation, the change in Gibbs free energy, ΔG_r, is

$$\Delta G_r = \left\{ -\frac{4}{3}\pi r^3 \Delta G_v + 4\pi r^2 \gamma_{SL} \right\} S(\theta)$$

where the ΔG_v is the free energy per volume due to the liquid-to-solid phase transformation, γ_{SL} is the interfacial free energy of the solid-liquid interface, and the r is the radius of the spherical nucleus. Note that the geometry of the nucleus is assumed to be spherical. The term $S(\theta)$ stands for the consideration of the heterogenous nucleation, which is named as the wetting factor, and the θ is the wetting angle. Then, the wetting factor can be expressed as

$$S(\theta) = 0.25(2 + \cos\theta)(1 - \cos\theta)^2$$

Hence, the critical nucleus size, r^*, for a cluster to nucleate can be found by the derivation of the change in the free energy.

$$r^* = -\frac{2\gamma_{SL}}{\Delta G_v}$$

Also, the required Gibbs free energy (ΔG^*), i.e., the energy barrier for nucleation, can be expressed as

$$\Delta G^* = -\frac{16\pi\gamma_{SL}{}^3}{3\Delta G_v{}^2} S(\theta)$$

In this equation, ΔG^* is inversely proportional to the ΔG_v. ΔG_v can also be furtherly expressed as

$$\Delta G_v = -\frac{L_v \Delta T}{T_m}$$

where the L_v is the latent heat of fusion, T_m is the melting temperature, and the ΔT is the amount of undercooling. During cooling from the melt, the T_m is the point where the free energies of both the liquid and the solid phases are equal to each other, and the ΔG^* is infinite. It means that the solid cannot form under these conditions. It also means that the liquid can be undercooled from its melting temperature, without any nucleation, until enough time has been spent to exceed r^* for the clusters. For the lower undercooling amounts, the atomic mobility is high, but the energy barrier for the nucleation is also high. So, the required time to initiate nucleation and freeze the liquid to a solid form is high. When the undercooling gets higher, the driving force for nucleation also gets higher. Then, the time for the nuclei to form gets lower. Conversely, atomic mobility gets lower for the higher undercooling and delays the nucleation. This competition is well-expressed with the time-temperature-transformation (TTT) diagrams for the alloys. Meanwhile, the same competition is also important to obtain a glassy metal, i.e., a frozen liquid.

The nucleation rate of the crystals during this process can be expressed as

$$I_v = \frac{A_v}{\eta(T)} \exp\left(-\frac{\Delta G^*}{k_B T}\right)$$

where the I_v is the crystal nucleation rate, A_v is a constant, $\eta(T)$ is the temperature-dependent viscosity, k_B is the Boltzmann constant, and T is the temperature of the material [17]. As stated earlier, this rate of nucleation competes with the viscosity

increment during rapid solidification. The viscosity of a melt generally obeys an Arrhenius type of equation, which can be expressed as

$$\eta = \eta_0 \exp\left(\frac{E}{RT}\right)$$

where η_0 is the viscosity at infinite temperature, E is the activation energy for the flow, and R is the gas constant. The modified version of this expression to better correlate the temperature dependence of the viscosity is the Vogel-Fulcher-Tammann (VFT) equation. Further modification into VFT yields

$$\eta = \eta_0 \exp\left(\frac{DT_0}{T - T_0}\right)$$

where D is the fragility index of glass, i.e., the strength of temperature dependence of relaxation time, and T_0 is the VFT temperature [18]. Lastly, D can be expressed as

$$D = \frac{\delta\mu S_c^* k_B^{-1}}{K}$$

where $\delta\mu$ is the chemical potential difference between liquid and glass states, S_c^* is the minimum entropy usually expressed as $k_B \ln 2$ or $k_B \ln 2^3$, and K is the proportionality constant which expresses the variation of heat capacity between two phases as hyperbolic dependent on temperature [18].

One can estimate the glass-forming tendency of a random system using these thermodynamical and kinetical backgrounds. However, a useful calculation, especially for the Al-based marginal metallic glasses, was done to visualize the glass formation range (GFR) of several Al-RE (rare earth) alloys. In 1998, Inoue reported the glass formation ranges for Al-RE (RE = Y, La, Ce, Pr, Nd, Sm, Gd, Tb, Dy, Ho, Er, Yb) binary systems by combining the thermodynamical calculations on undercooling and viscosity with the equilibrium phase diagrams. Results can be seen below figure (Figure 1.3).

11
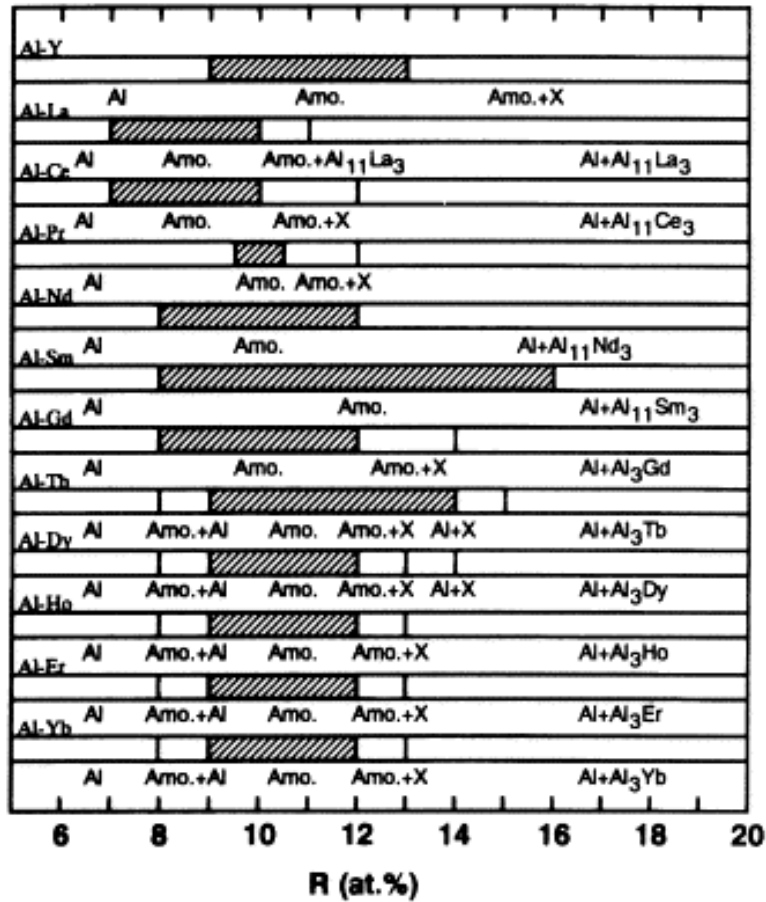
Figure 1.3 Glass formation ranges for different Al-RE binary systems. Adopted from [19]

1.4   Marginal Metallic Glasses

As the name implies, marginal metallic glasses, which are usually Al-Rare Earth (RE) types of alloys, are the subset of metallic glasses that forms and behaves differently than the bulk ones. Conventional bulk metallic glasses have a composition range near the eutectic zones. However, these alloys make amorphous metals at off–eutectic compositions. This is anomalous since the undercooling necessary to produce an amorphous metal will be higher at off-eutectic compositions, and obtaining a higher amount of undercooling is thermodynamically more difficult.

Not only their formation but also their further devitrification behaviors are different from the conventional amorphous metals. The number crystal density of their first devitrification product, i.e., pure fcc-Al, is orders of magnitude higher than the prediction of classical nucleation theory. The kinetics and diffusion thermodynamics of Al-RE systems are still insufficient to explain such behaviors.

For years, these marginalities have tried to be explained by our research group. Several studies focused on different types of Al-RE alloys. Their devitrification behaviors, crystallization kinetics, and local orders in an amorphous state were all investigated by some advanced characterization tools like in-situ synchrotron high-energy X-ray experiments, atom probe tomography, transmission electron microscopy, scanning electron microscopy, differential scanning calorimetry, and more. In this study, another candidate system was chosen to investigate such behaviors, which is Al-Y. Besides this, the pre-studied Al-Tb system is also used to explain the emerging mechanical properties of these amorphous metals and their devitrified products. Ultimately, all the new findings were compared with the other systems, such as Al-Sm binaries and some Al-RE-RE ternaries. All these systems are suitable models to explain the anomaly of the MMGs since they all exhibit amorphous configuration in a marginal form when the proper conditions are satisfied.

1.5   Characterization Techniques

As the key to understanding the reason behind the emerging properties of metallic glasses is characterization, one should extensively use characterization tools. However, the length scale to investigate these reasonings is on the order of atoms. Therefore, one should consider using cutting-edge characterization methods, such as synchrotron and neutron X-ray scattering, high-resolution transmission electron microscopy, or atom probe tomography. Resolving the features such as atomic-scale clusters and the heterogeneity in the amorphous configuration is essential to understand the related behavior of these glassy metals.

1.5.1   X-Ray Scattering

One can define the clustering either chemically or geometrically. When the importance is on the geometrical side, X-ray diffraction is the fundamental tool. Conventional X-ray diffraction (XRD), mainly with Cu Kα_1 radiation of 1.540598 Å, is one of the most used methods to understand the glassy metal. It gives good pre-insight of the structure. One can tell whether or not the metallic glass is correctly produced. Furthermore, the devitrified phases may also be investigated ex-situ.

However, two drawbacks of the lab-scale conventional X-ray scattering are the corresponding reciprocal length scale, i.e., the Q range of the spectrum, and the ability of the conducting in-situ experiments for extremely metastable materials. The clusters of our interest have, at most, a few nanometers of order in scale. Therefore, a radiation source capable of high Q_{max} and high brilliance is a must. Resolving such structural details with higher sensitivities in a nanocrystalline material requires synchrotron X-ray radiation or a pulsed neutron source. Also, the crystalline phase formation kinetics during devitrification occurs in nanoseconds since the amorphous state is highly unstable. Therefore, fast experimentation is also a must. Although high-quality data with conventional XRD requires hours or sometimes days, these data can be collected in seconds with advanced detectors and X-ray sources at synchrotrons, even at orders of magnitude higher qualities. In the end, synchrotron X-ray scattering can be considered a must for investigating amorphous metals.

The other consideration of the clusters was chemical, as stated above. For the chemical investigation at atomic length scale, small angle X-ray scattering (SAXS) and X-ray absorption spectroscopy (XAS) methods are the preferable ones.

Using SAXS simultaneously with wide-angle X-ray scattering (WAXS) can give precious information on our knowledge of crystalline phase formation. While the WAXS supplies information on the geometry, the collected SAXS signal can show the compositional gradient in the structure during crystallization. This chemical information, combined with the geometrical one, may reveal whether the chemical

or geometrical necessities drive the crystallization first. This data is crucial to determining the importance of medium-range order (MRO).

When using XAS, X-ray near-edge structure (XANES) and extended X-ray absorption fine structure (EXAFS) enlighten the clustering in the amorphous state. The chemical potential that drives the atoms together in short to medium-range ordered manner later can be the reason for the increased number crystal density during devitrification. The information from the XAS data can be combined with other experimental data to obtain high-quality RMC simulations. Ultimately, these simulations can enlighten the true configuration of the amorphous states.

1.5.2   Analytical Electron Microscopy

Analytical electron microscopy, including scanning electron microscopy (SEM) and transmission electron microscopy (TEM), is another powerful tool to characterize metallic glasses and their devitrified products. Especially using different TEM techniques supply essential data on this topic. SEM has its limits when investigating features within a scale of tens of Å to a few nm. However, observing the fracture surfaces, mainly in the case of BMG, using secondary electron imaging (SEI) with SEM gives auspicious results. Also, some chemical analyses, thanks to the inserted detectors on the SEM, such as energy dispersive spectroscopy (EDS) and wavelength dispersive spectroscopy (WDS), provide general information on the composition. One can gather information on the chemical homogeneity and the compositional consistency with these tools. Backscattered electrons (BSE) can be used to visualize heterogeneity if it is noticeable and the composed elements have a higher difference in atomic number. This is crucial since the contrast mechanism for backscattered imaging yield is based on the orbit-momentum movement of the source electrons around the composed elements. A higher atomic number yields higher BSE. When the difference in the atomic number gets higher for the components, the contrast also gets higher. Even electron-backscattered diffraction (EBSD) can be used for suitable cases to obtain information on the orientation of the newly formed crystalline phases

during devitrification. Recently, inserting micromechanical test equipment or heating stages into SEM made conducting some very useful in-situ experiments possible.

While SEM is a precious tool, TEM gains more importance on marginal metallic glass characterization. It can supply chemical information on the order of clusters of concern. Even determining the type of specific atom is possible with a chemical analysis called atomic-level electron energy loss spectroscopy (EELS) mapping. High-resolution transmission electron microscope (HRTEM) imaging with a spherical aberration (Cs) corrected TEM can visualize the lattice features atom by atom. High-resolution scanning transmission electron microscopy (STEM) provides chemically meaningful data at an atomic level. Selected area electron diffraction (SAED) patterns show whether the chosen few nanometers region is amorphous or not. If not, it can give information on the crystalline phase. Fast Fourier transformation (FFT) and inverse fast Fourier transformation (IFFT) can be used to visualize individual crystalline signals and filter out the rest of the structure. Bright-field (BF) and dark-field (DF) imaging supply different important data on the structure. However, the most important data comes from the fluctuation electron microscopy (FEM) when it comes to observing the MRO. FEM is the only experimental technique that is highly sensible to medium-range order within the electron microscopy methods, and nanobeam diffraction (NBED) comes next. Also, recently growing 4D microscopy with TEM includes the time domain to the analysis, which broads the possibilities for the characterization. Besides all, using in-situ tools with TEM leads to the development of cutting-edge experimentation.

Preparing a proper TEM specimen is key for the observations during analyses. Depending on the material type and the possible advantages and disadvantages, one can proceed with the old fashion route, which is the cutting, dimpling, grinding, punching, and electropolishing route. Other possibilities are using the focused-ion beam or ion milling.

1.5.3 Thermal Analyses

Most of the important parameters of the metallic glasses need thermal investigations to be found. Several signals that can be observed by thermal characterizations can be listed as the glass transition, crystallization, liquidification, and more. One can find or investigate the crystallization sequence, enthalpy required for the transformations, reaction kinetics, thermal stability, the fraction of the crystalline and the amorphous phases during devitrification, or the specific temperatures such as T_x and T_g. All of these are possible with differential scanning calorimetry (DSC) and differential thermal analysis (DTA). Other thermal analyses that can be useful for several cases are thermomechanical analysis (TMA), dynamic mechanical analysis (DMA), and thermogravimetry (TG).

1.5.4 Mechanical and Micromechanical Characterizations

A materials engineer needs to correlate the structure with the properties. For this reason, measuring the related properties of different configurations are important. One of the eye-catching properties of metallic glasses is the mechanical enhancement of these alloys, considering their traditional counterparts. To mechanically characterize the materials, conventional test methods are still applicable for most metallic glasses. Although the bulk production of the material and the standardization of the geometry are the two problems for these experiments, still, standardized or off-standard tensile tests, compression tests, and microhardness measurements are conducting for these materials.

However, especially for MMGs, scientists need more focused, in-depth mechanical characterization methods. Usual MMG has a thickness of around 40 μm and a width of a few mm. Their devitrified products have a length of nanometers. For these reasons, micromechanical characterization techniques are often used. The mainly used ones are micropillar compression and nanoindentation. One can even prepare a pillar on the ribbon, compress and analyze it micromechanically, then prepare a TEM

specimen on the deformed region using FIB and further structurally analyze it and conclude the results.

1.5.5   Other Characterization Techniques and Simulations

There are uncountably many characterization techniques for glassy metals. Using a tool or a technique in favor of the characterization of metallic glasses is a skill for scientists. Other than the techniques mentioned above, atom probe tomography (APT) is highly used to observe the chemical distribution of the components in the amorphous state in 3D. Scratch testing is used to observe the wear resistance behavior of these metals. A vibrating sample magnetometer (VSM) is used to determine the magnetic properties and so on.

Other than real-life characterization experiments, simulations gain importance and become indispensable as experimentation. The main reason, especially for the MMGs, is the difficulties of production and experimentation. One can observe the amorphous configuration of these glassy metals by Reverse-Monte-Carlo (RMC), Molecular Dynamics (MD) simulations, or ab-initio models. One can also approximate the corresponding properties of these alloys, analyze the short to medium-range orders and even visualize the local clusters. All of these are possible within very short time intervals, thanks to the recent developments in high-performance computing and artificial intelligence. Using high-performance parallel computing and suitable simulation methods, one can construct realistic models in minutes that normally may take months to produce, characterize and analyze.

1.6   Previous Studies and the Progression of the Research Question

As in the case of the breadcrumbs of Hansel and Gretel, there are vital research papers and people that led the way here. One of the first comprehensive Al-RE marginal metallic glass investigations centered on the structure and property relationship was made by Dr. Kalay in 2008. Dr. Kalay investigated and

characterized the crystallization behavior of a highly driven $Al_{90}Sm_{10}$ marginal metallic glass produced by a melt spinner and high-pressure gas atomization [20,21]. Many papers followed during his Ph.D. at Iowa State University [22–25]. The questions started to emerge in those years. Why do these metals have an amorphous structure at off-eutectic compositions, even though it is thermodynamically easier to have one at eutectic compositions? Also, their corresponding mechanical properties were very promising, and the structural reason for these emerging properties was not enlightened yet for those years.

The investigations continued at Middle East Technical University (METU), where Dr. Kalay continued his academic studies as a professor. The first project on this crucial subject at METU was investigating the crystallization kinetics of these marginal glass former alloys. The candidate system was determined as Al-Tb, with the consideration of its glass formation ability. Demirtas and Kalay conducted several mechanical and TEM experiments to observe the structure and property relationship of its amorphous and devitrified states [26]. Observations showed that the number crystal density of the first devitrified product of this system, which is pure fcc-Al, is way higher than the predictions of classical nucleation theory. Demirtas and Kalay, following W.L. Johnson's studies [27], have found that the number nucleation density of fcc-Al is on the order of 10^{21} crystal/m^3 [26].

Later, Ovun, Kramer, and Kalay focused on the structural modeling of liquid and amorphous Al-Tb alloy with inverse Monte Carlo (IMC) simulations [28]. These studies draw attention to the composition of the specific alloys, the amount of undercooling, and the importance of the possible structural medium-range ordering in the liquid state. Is much higher undercooling obtained because of the small pure Al domains? Is there a special ratio of Al/RE that pushes the glass formation range (GFR) beyond the eutectic region?

All these questions needed some strong evidence to support them. To do that, Yildirim et al. carried out in situ high-temperature high-energy X-ray diffraction (HEXRD) experiments on the Al-Tb system using different amorphous precursors.

The role of liquid and gaseous state precursors was investigated regarding the phase selection hierarchy in these systems. It is found that the different precursor states yield different phase selections during devitrification [29]. The behavior during devitrification for the melt-spun MMG was also pointing to the possible ordering in the liquid. It means that the liquid and the gaseous states for the exact same composition solidify into different amorphous configurations, thus structures. So, is liquid not homogeneous?

After all these strong experiments supported the liquid MRO idea, Ulucan et al. conducted a well-reliable reverse Monte Carlo (RMC) simulation to find the proofs for the anomalous nucleation in the Al-Tb system that contain a hint of medium-range ordering for these amorphous metals and their liquids [30]. They constrained their RMC simulations with extended X-ray absorption fine structure (EXAFS), synchrotron $S(Q) - Q$, and ab-initio data. The EXAFS data were collected at ALBA Synchrotron, Spain, with a team of Kalay, Okuyucu, Yasar, and Sari. Ulucan et al. proposed the idea that the pure Al clusters, identified by the Voronoi analyses, in the amorphous structure were the nucleation domains for the fcc-Al crystals during devitrification.

In the same year of Ulucan's studies, Okuyucu et al. studied another Al-RE system, which is Al-Sm. The idea was to produce and characterize an Al-Sm alloy under far from equilibrium conditions that is not MMG but is at the corner of amorphization, considering its GFR in terms of composition. The research showed that even the crystalline Al-RE alloy, which is fully supersaturated solid solution fcc-Al, under an extensive amount of undercooling, has very promising mechanical properties for these types of alloys [31].

Years later, Sariturk and Kalay focused on the Molecular Dynamics (MD) simulations of the $Al_{90}Sm_{10}$ MMG and its liquid state [32]. They cooled down a liquid from 2300 K to 300 K and analyzed the local structural arrangements using Voronoi tesselation. They discovered that the liquid is chemically inhomogeneous

and contains large pure Al regions divided by a network of Sm-rich clusters at high temperatures.

Complex experimental setups were necessary to observe the Al-RE liquid's local atomic arrangements. Some of the problems of such achievement can be listed as the first obtainment of the Al-RE MMG due to the amount of undercooling necessary, the stable observation of the liquid phase at high temperatures since the RE is a highly oxidizable component, and the observation of the clues of structural ordering with HEXRD without oxidizing the material but also penetrating through it with X-rays while the signal collected by the detector is not affected from outside such as the holder equipment or so. There were a couple of tries at Synchrotron SOLEIL, France, both with Ulucan, Okuyucu, Sikan, and Kalay, using different experimental conditions and setups. Yet, all failed due to the problems listed above. Also, a possible suitable configuration was found at Diamond Synchrotron, but the visit failed due to the Covid-19 pandemic, although the proposal was accepted. As it stands today, there are a couple of successful observations of the liquid structure using HEXRD, even if they are at relatively lower temperatures, that will be discussed later in this thesis.

As the journey continues, all of the questions have gained importance through the years. We have had new questions and explanations on the first formation, anomalous nucleation, emerging properties, and the MRO of the amorphous and liquid state of these Al-RE MMGs. Throughout this thesis, we will discuss and evolve these questions by reviewing the previous studies at the Metals Development Laboratory (MDL) of Dr. Kalay, and we try to develop more comprehensive answers to them. Also, we will accomplish a broad sense of this subject by connecting these structural and local atomic arrangements to physically measurable properties. In the end, this study aims to relate some physical properties to the yet unexplained structural features to predict and understand the influence of structure on its emerging properties under far-from-equilibrium conditions.

CHAPTER 2

STRUCTURES OF MARGINAL METALLIC GLASSES

2.1   Introduction

The reasons for the unexpected behaviors of marginal metallic glasses, such as unpredictably higher number crystal density upon devitrification, formation of amorphous metal under off-eutectic compositions, and highly enhanced mechanical properties, remained unclear so far. All the possible explanations for these phenomena are hidden in the atomic interactions within the amorphous configuration. For this reason, our research group carried out detailed investigations on the structure for years. Al-RE systems were chosen as a raw model system for such structural evaluations. Some binaries like Al-Tb, and Al-Sm alloys and ternaries like Al-Sm-Tb, and Al-Y-Tb systems have been investigated so far. Since these Al-RE alloys are an excellent raw model system to investigate these anomalies, another unstudied combination of Al-RE was chosen as a candidate system to proceed for further possible explanations of the unclear parts in the literature.

This system is decided as an Al-Y binary since its glass-forming ability is similar to other well-studied systems, and its atomic radii mismatch is similar to the Sm and Tb. Yttrium is also a good X-ray scattering atom under experimental conditions. The composition is determined as $Al_{90}Y_{10}$ for further analysis since it is in the glass formability range for this binary alloy, according to Inoue [19]. The general perspective on the structural reasonings of these anomalies and emerging properties seen at marginal metallic glasses are given in this chapter, combining the recently conducted AlY experiments and the current literature.

2.2   Experimental Procedures

The pre-determined alloy composition, $Al_{90}Y_{10}$, was produced by a single block Cu wheel melt spinner with a tangential speed of 30 m/s under the He atmosphere. Rapid solidification procedures are essential to produce such alloys since one needs around a million Kelvin per second cooling rates to achieve amorphous configuration for these systems. Previous studies in our group show evidence of the local structure and devitrification path change concerning different precursors [29]. For this reason, a liquid precursor was necessary to correlate the results with the previous studies. After all these considerations, the melt spinning technique was chosen as a production method. The samples were produced at the Materials Preparation Center of the Ames Laboratory, USA. When the alloys were produced, the composition of each batch was checked with wavelength-dispersive spectroscopy (WDS) and cross-checked with energy-dispersive spectroscopy (EDS). The final thickness of the produced ribbons was around 30 – 40 micrometers.

DSC analyses were done using Perkin Elmer Diamond differential scanning calorimetry at METU Central Laboratory. Reference sample measurements with an empty Al pan were also taken for the baseline correction. For all DSC experiments, 10 mg ribbons were cut into rectangular shapes. They were inserted in Al pans, and the pans were covered with Al lids. Experiments were conducted with 40 °C/min heating rates in an N_2 atmosphere. Isochronal heating traces were recorded and analyzed.

Analytical microscopy studies were conducted by TEM. Either JEOL JEM 2100F 200kV HRTEM or FEI Tecnai G^2 F20 S/TEM were used for the investigations. Bright-field (BF) and scanning transmission electron microscopy (STEM) high-angle annular dark field (HAADF) imaging were used to investigate the structure. EDS mapping is used to reveal the chemical structure of the alloy. Selected area electron diffraction patterns (SAEDP) were collected from the different parts of the structure. High-resolution transmission electron microscopy imaging (HRTEM) and fast Fourier transform (FFT) patterns were used to identify the local structures.

Camera length calibration was performed before solving the SAED patterns. Gatan Microscopy Suite 3 (GMS3) DigitalMicrograph software is used for the TEM data analysis.

TEM specimens were either prepared by electropolishing or a focused ion beam (FIB). For the electropolishing route, the samples were first punched into 3 mm diameter disks and ground into thicknesses lower than a few microns. After that, Fischione Model 110 Twin Jet Electropolisher is used for electropolishing. The electropolish solution was a mixture of 75% methanol and 25% nitric acid at 235 K. Liquid nitrogen was used to cool the polishing solution. For the FIB route, samples were prepared by Pt deposition, Ga milling, and lift-out steps. The thinned specimens were welded into suitable lift-out grids using OmniProbe.

X-ray diffraction experiments were done using Bruker D8 Advance diffractometer under Bragg-Brentano geometry using Ni-filtered Cu K_α radiation. The scan rate for the experiments was 1 °/min.

Synchrotron light source experiments were conducted at ALBA Synchrotron, Spain. In-situ heating HEXRD data were collected with a Mythen array detector in transmission mode at the BL04-MSPD beamline. The wavelength used in these experiments was selected with a double Si monochromator system, which corresponds to 0.49618 Å.

2.3   Results and Discussions

2.3.1   Initial Structural and Chemical Characterization

After the melt-spun ribbon samples were produced, their initial chemical compositions were determined with WDS. When the samples came into our laboratory, their chemical compositions were validated with EDS using SEM. EDS analyses were done several times on the air and the wheel sides. The average of the data with consistent ZAF correction can be seen below (Table 2.1). ZAF correction

25

considers the effect of atomic number (Z), absorption (A), and fluorescence excitation (F) when making quantitative analysis. The results of EDS were in good agreement with the WDS data. It can be concluded that the composition of the ribbons is $Al_{90}Y_{10}$.

Table 2.1 EDS Results of the melt-spun ribbons

Composition of the initial Al-Y melt-spun ribbons (at%)	
Al	89.76
Y	10.24

Their structural states were confirmed using XRD with Cu Kα radiation. Since the cooling rate may differ at the air and the wheel side of the ribbons, data were collected separately. It is seen that the cooling rates on each side were enough to freeze the liquid and obtain an amorphous phase. As can be seen from the resultant XRD data, the $Al_{90}Y_{10}$ MMG has its characteristic pre-peak and amorphous hump (Figure 2.1). The main hump is a standard feature for amorphous materials. However, the pre-peak is a very distinctive feature of the MMGs. This pre-peak at the XRD data can hint at some correlation in atomic level for the amorphous state. It is argued in the literature that the Al-based MMGs have short to medium-range ordered correlations [24,25,28,30]. The corresponding reciprocal length scale, i.e., Q, for the pre-peak and the side-peaks corresponds to the RE-RE distances in the clusters. It is already validated for other Al-based MMGs with partial RE-RE structure factors and will be discussed later in this chapter. Moreover, these distances are also the same distances of the intermetallics formed due to the devitrification process. For these reasons, it can also be argued that the Al-Y MMGs have the same short- to medium-order correlation.
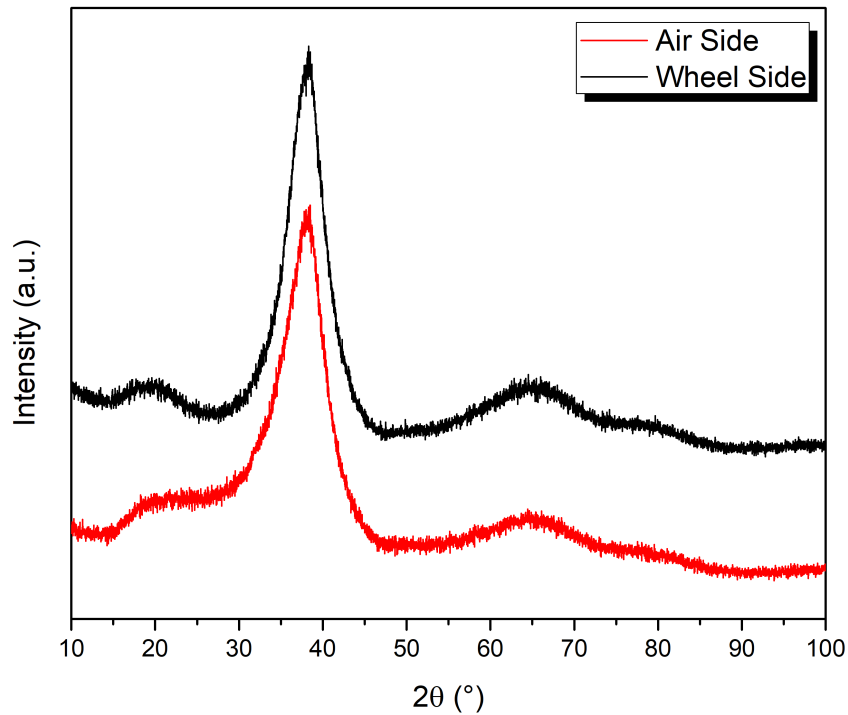
Figure 2.1 XRD results of the melt-spun $Al_{90}Y_{10}$ ribbons

2.3.2　　　Understanding and Measuring the Medium Range Order

There are three types of atomic correlations in the materials. These are short, medium, and long-range orders. The short-range order (SRO) is based on the pair correlations. It considers the bonding of an atom with its neighbors when defining the order. Therefore, SRO is usually lower than 0.5 nanometers. For the crystalline materials, it is said that they exhibit long-range order. If atoms are distributed in a Bravais lattice so that they obey a type of point group symmetry, they form a unit cell. The unit cell must include the motif, has a minimum volume, and contains atoms in a symmetrical manner. When a translational symmetry operation for that unit cell is applied in 3 dimensions, the structure extends to infinity. This is how a defect-free

crystalline material is defined. The order that goes up to infinity is called long-range order (LRO). In practice, this order starts from 3 nanometers.

The order between SRO and LRO is defined as MRO. It usually exists between 0.5 to 3 nanometers. The MRO considers pair-pair correlations. This means that the correlation of an atom with its shortest neighbor and, again, the correlation of the shortest neighbor with its shortest neighbor must be somehow ordered.

Detecting an LRO is comparably more straightforward than the others. It has characteristic Bragg reflections in the diffraction spectrum. Using conventional X-ray diffractometers is usually enough if a sufficient amount of that particular phase with LRO is in the structure. To detect SRO and MRO, some advanced-level diffraction techniques like data collection with high brilliance, brightness, and energy X-ray source, i.e., synchrotron light source, are usually necessary. Neutron and electron diffraction techniques are also used. One needs a high-quality peak-to-noise ratio and a high reciprocal length range coverage to analyze the short to medium-range correlations correctly. All the factors affecting the diffracted beam intensity must be collected and calculated. Some of these are parasitic intensity, intensity due to temperature diffuse scattering, intensity due to Compton scattering, and intensity due to elastically scattered X-rays. The information regarding the structure comes from the elastically scattered X-rays. After eliminating the other factors affecting intensity, the structural part of the intensity can be calculated from the intensity of elastically scattered X-rays. This structural base is defined as the total structure factor and represented with $S(Q)$. $S(Q)$ can be calculated by

$$S(Q) = \frac{I(Q)}{\langle f(Q) \rangle^2} + 1 - \frac{\langle f(Q)^2 \rangle}{\langle f(Q) \rangle^2}$$

where $f(Q)$ is the atomic scattering factor. Another important function is derived when the Fourier transform of the $S(Q)$ is taken. It is the pair distribution function and is represented as $\rho(r)$. It can be derived from the experimental data using the following formulation.

$$\rho(r) = \rho_0 + \frac{1}{2\pi^2 r} \int_{Q_{min}}^{Q_{max}} Q[S(Q) - 1] \sin(Qr) dQ$$

where ρ_0 is the average atomic density. $\rho(r)$ is a statistical function that gives all the particle-particle distances in the material as a histogram. When visualizing the pair distribution function, the peak profiles and the areas underneath those peaks give crucial information on the local orders. The peak positions are the points where the neighbor atoms are mostly collected. The distance from an atom center to a certain peak gives the average distance between these atoms. For the materials that exhibit LRO, i.e., solid-phase crystalline materials, these peak points are rather certain. However, the peak profile, including the shape, broadening, i.e., full-width-at-half-maximum (FWHM), and position, may deviate from its certain position due to the defects that promote disordering or thermal fluctuations. Therefore, the peak profiles can also be used to comment on the disordering.

When the pair distribution function is further modified, $4\pi r^2 \rho(r)$ can be obtained. It is the radial distribution function (RDF) and gives the average number of atom centers between distances r and $r + dr$ from the center of an average atom. It should be noted that this average is an average over the surroundings of each atom in the material and also an average over the time domain of the measurement for the liquid phase. Therefore, it represents the minimum structure in the sample.

For each case, these functions are random for the amorphous materials. Nevertheless, this randomness is a questionable thing. The first noticeable peak of these functions becomes important to analyze the short-range order correlations in the amorphous configuration. Meanwhile, the peaks corresponding to 0.5 to 3 nanometers in real space give crucial information on the MRO correlation. Meanwhile, the area underneath the first peak of the radial distribution function supplies the atomic coordination number, and it is calculated as

$$N_{coordination} = \rho \int_{r_1}^{r_2} \rho(r) 4\pi r^2 dr$$

Furthermore, the atomic pair distribution function is represented as

$$G(r) = 4\pi r[\rho(r) - \rho_0]$$

The functions $S(Q)$ and $G(r)$ builds our comments on the structural features of metallic glasses. They are the equivalent of themselves in the reciprocal and the real space, respectively. This is why one applies a Fourier transformation to convert one another. An example $S(Q)$ data for the $Al_{90}Tb_{10}$ and $Al_{91}Tb_9$ MMGs is shown below (Figure 2.2). Note that the distinct features of MMG, i.e., pre-peak and side-peak, exist at the total structure factor function.
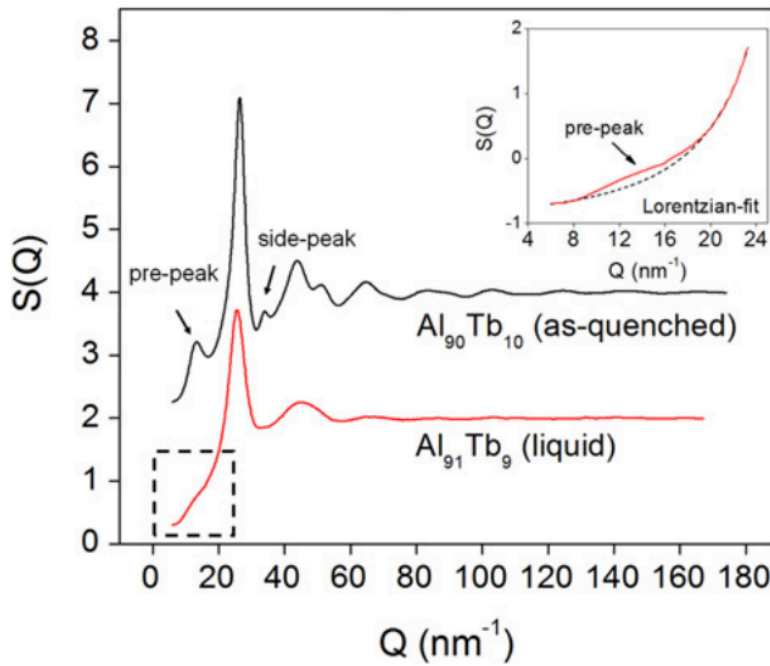
Figure 2.2 An example total structure factor function for as-quenched $Al_{90}Tb_{10}$ and liquid $Al_{91}Tb_9$ at 1174 K. Adopted from [25]

2.3.2.1   Insight of Structure Factor

So far, the experimental measurement of the total structure factor and the conversion of it to an atomic pair distribution function is covered. But a standalone structure factor definition can also be given as

$$S(Q) = \frac{1}{N} \langle \left| \sum_{i=1}^{N} e^{iQr_i(t)} \right|^2 \rangle$$

where Q is the wavevector, N is the total number of atoms in the system, and $r_i(t)$ is the time-dependent distance between atoms. Also, the conversion between the structure factor and the pair distribution function can be represented as

$$S(Q) = 1 + 4\pi n \int r^2 [\rho(r) - 1] \frac{\sin Qr}{Qr} dr$$

An example of the radial distribution function for $Al_{90}Sm_{10}$ MMG is given below with respect to temperature (Figure 2.3). This MD-simulated pattern shows the characteristic second-peak splitting of MMG with temperature.
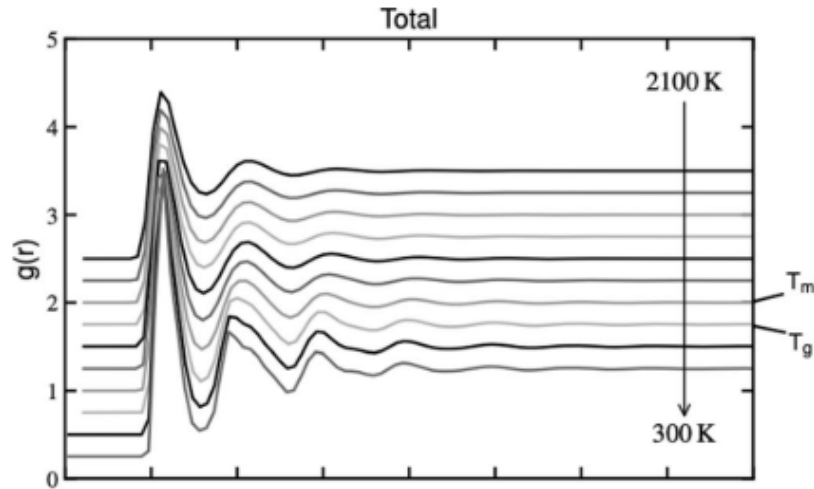
Figure 2.3 MD-simulated total radial distribution function of $Al_{90}Sm_{10}$ with temperature. Adopted from [32]

2.3.2.2   Network Clusters

Not only the total structure factor and the total RDF functions supply information on the structure. Instead, detailed investigations need partial structure factor and partial RDF data. For example, partial functions in Al-based MMGs can be in the form of Al-Al, RE-RE, and Al-RE partials, and these partials reveal the true reasons for the local atomic arrangements in the amorphous state. The relationship between pre-peak and side-peak with the MRO is based on the investigation of RE-RE partials. The study of partial structure factors in as-quenched and liquid $Al_{89}Sm_{11}$ marginal glass former at 1313 K reveals that the pre-peak and the side-peak of the amorphous phase correspond to the interplanar spacings of (002) and (211) planes in the tetragonal $Al_{11}Sm_3$ intermetallic [24] (Figure 2.4). This phase is body-centered tetragonal and stable between 1351 and 1733 K for this system, according to the phase diagram. This is particularly important because it can be argued that this structure also exists in the amorphous solid and its parental liquid state in the pseudo form. The pre-existing MRO in the molten state may persist during rapid solidification and form a network of pseudo-tetragonal clusters in the amorphous solid. The crystalline t-$Al_{11}Sm_3$ and the clustered pseudo version are shown below (Figure 2.5).
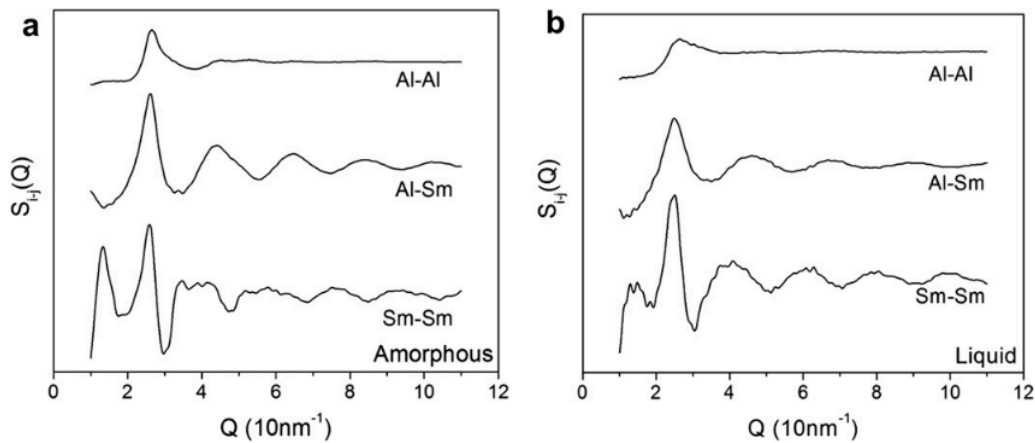
Figure 2.4 Calculated partial structure factors for (a) as-quenched and (b) liquid $Al_{89}Sm_{11}$ marginal glass former at 1313 K. Adopted from [24]
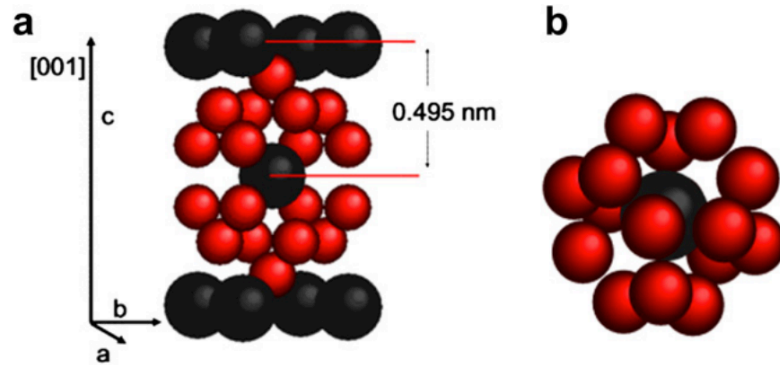
Figure 2.5 (a) Tetragonal $Al_{11}Sm_4$ phase, and (b) the possible pseudo-crystalline cluster that forms MRO in the amorphous phase. The red dots are the Al atoms, and the black dots are the Sm atoms. Adopted from [24]

For the t-$Al_{11}Sm_4$ phase, the center Sm atom has 8 Al atoms at 0.325 nm and another 8 Al atoms at 0.327 nm distance. When coordination number (CN) calculations were done for the Al and Sm-centered Voronoi polyhedra models, it was seen that the Sm-centered clusters are highly coordinated and have higher coordination than the Al-centered clusters (Figure 2.6). This is also persistent in the liquid state. The Al-centered clusters have a CN of around 14, with a first neighbor Al coordination of about 87%. Whereas, Sm-centered clusters have a CN of about 16, with a first neighbor Al coordination of about 94% and %87, for the amorphous and the parental liquid phase, respectively. The coordination behavior of centered-Sm with the nearest Al atoms at the t-$Al_{11}Sm_4$ phase is precisely the same as the candidate Sm-centered network cluster with 16 Al atoms at its first shell neighbors.
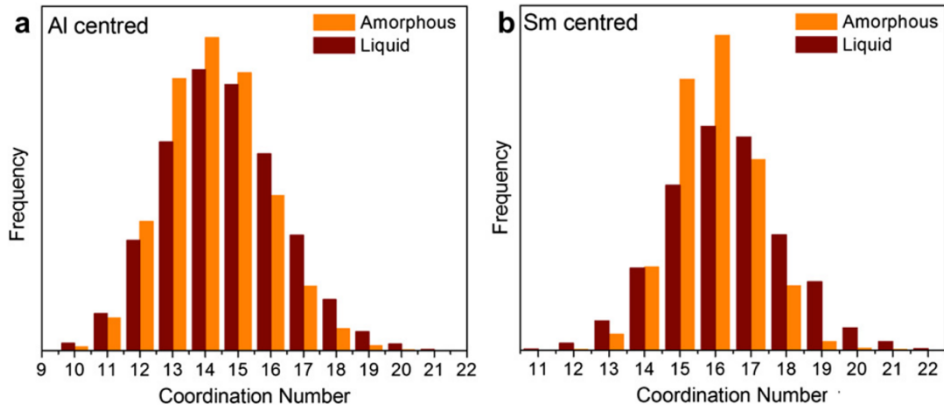
Figure 2.6 Coordination number histogram for the Al and Sm-centered clusters. Adopted from [24]

When the atom probe tomography data for another Al-RE MMG, $Al_{90}Tb_{10}$, is investigated, a similar separation is seen in the amorphous state (Figure 2.7). It is seen that the Tb-centered clusters divide the pure Al regions in the structure [25].
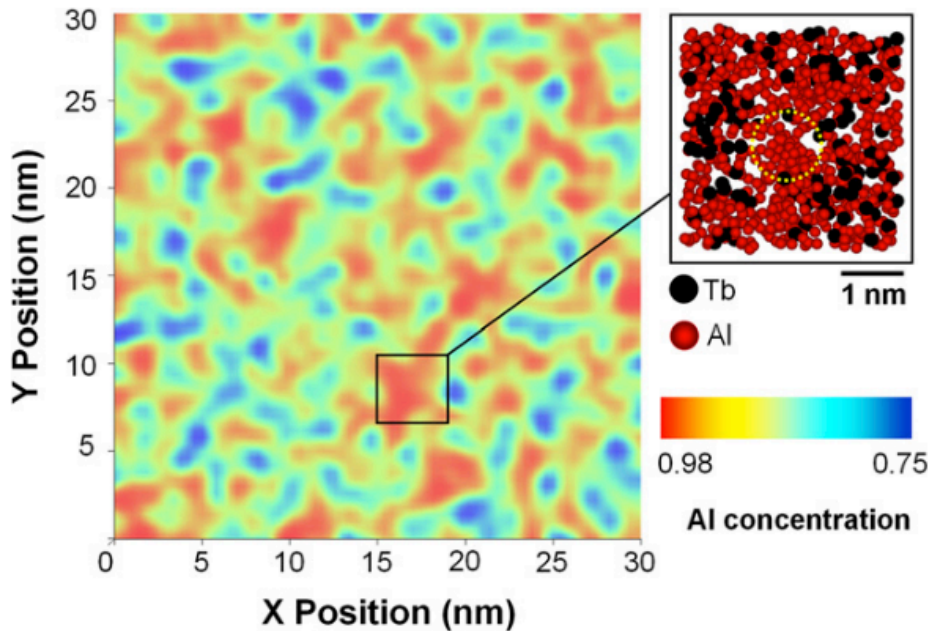
Figure 2.7 2D Al concentration map of the as-quenched $Al_{90}Tb_{10}$. Inset shows the schematic for the 3D APT data. Colors indicate the concentration limits. Adopted from [25]

Finally, the fluctuation electron microscopy (FEM) data of the $Al_{90}Tb_{10}$ MMG shows a clear indication of MRO, with two different types, including pseudo-fcc-Al and another [25] (Figure 2.8). Since FEM is a fundamental technique to sense MRO, these findings were significant.
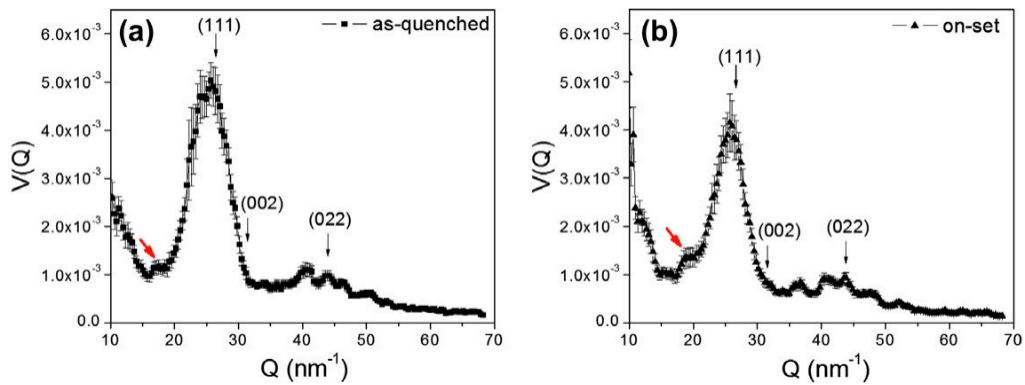
Figure 2.8 FEM analyses of (a) as-quenched and (b) annealed $Al_{90}Tb_{10}$ specimen to the onset of fcc-Al crystallization. The arrows indicate pre-peak. Adopted from [25]

All these data means that the amorphous state was divided into nearly pure Al regions, and these regions were surrounded and cut by the RE-rich clusters. Both Al and RE-rich clusters exhibit a type of MRO. Also, there is strong evidence that these medium-range ordered structures exist in the parental liquid state. It fundamentally and existentially means that the liquid and the amorphous configurations are not random.

Later in this thesis, these medium-range ordered clusters will be connected with the emerging properties of marginal metallic glasses and their devitrified amorphous/crystalline composites.

2.3.3   Synchrotron Radiation Studies

After reviewing the other Al-based MMGs, the research is focused on the Al-Y system. The question is whether this medium-range ordered clustering is related to the size difference of the atoms, or are there other factors determining the type of the order in amorphous and liquid states? Is there a role of thermodynamics, diffusion, solid-state physical laws, or chemistry?

Y has a lot of common and comparable properties with other rare earth elements, like the ones used in previous studies for MMGs, which are Sm and Tb. Their atomic radii, electronegativity, coordination tendencies, oxidation states, paramagnetic behaviors, and other chemical properties are relatively similar. For these reasons, Y is often considered as RE, although it is not. Other factors like their abundance, atomic mass, and density differences make them different. While Sm and Tb are in lanthanides, Y is a transition metal at the periodic table. Sm and Tb are in f-block with electron configurations $[Xe]4f^66s^2$ and $[Xe]4f^96s^2$, respectively. Meantime, Y is in a d-block with an electron configuration of $[Kr]4d^15s^2$.

Considering the information mentioned above, a set of in-situ heating high-energy X-ray diffraction experiments were conducted at the ALBA synchrotron with Kalay and Acar. The amorphous nature and the devitrification behavior of $Al_{90}Y_{10}$ MMG were investigated. The results were plotted as a 2D film (Figure 2.9). Indexing the formed phases during heating was done using Pearson Crystallography Database [33] and CaRIne Crystallography [34] software. HEXRD experiments showed that the initial phase formed during heating was the fcc-Al, as expected. Later, the remained amorphous phase was devitrified into a tetragonal intermetallic (IM) phase. The crystallization of a trigonal IM follows this. These two IM phases coexist within a short time interval during heating. The tetragonal phase diminished and was extinct after a short time/temperature interval. Meanwhile, the fcc-Al has remained in the structure from its first formation to the end of the experiment.
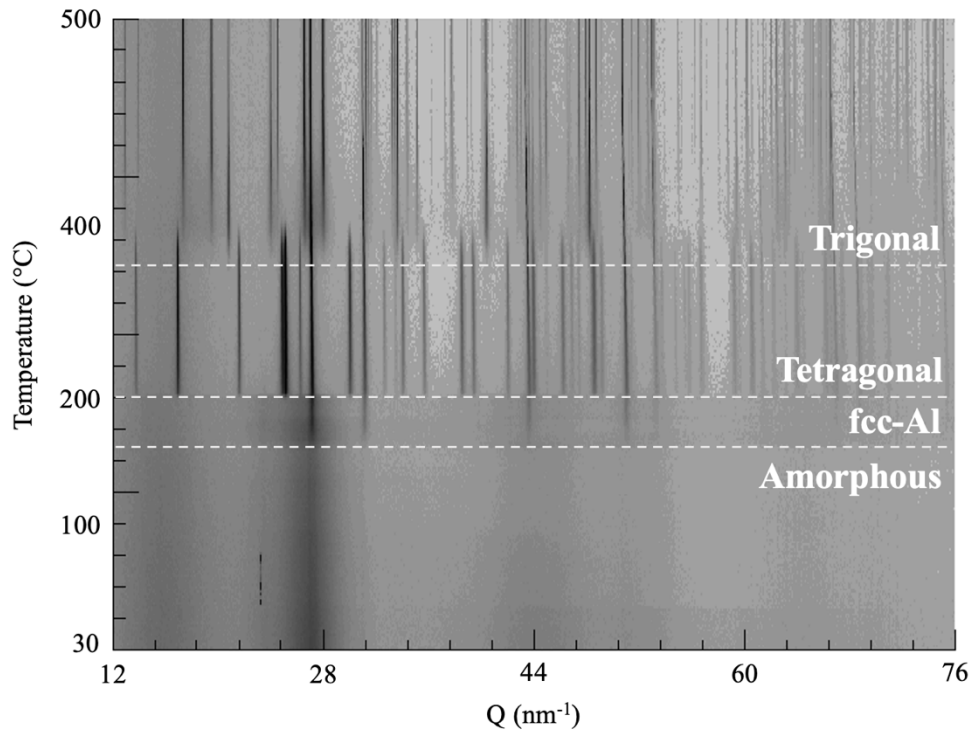
Figure 2.9 2D film plot shows the in-situ heating HEXRD result of melt-spun $Al_{90}Y_{10}$. Texts represent the newly formed phases

One thing that should be noted for this in-situ HEXRD profile is the temperature intervals given at the y-axis. Not all temperature intervals consist of an equal set of experiments since the temperature ramp during heating is not happening in equal time intervals. For this reason, the y-axis of the above 2D film plot is calibrated with the number of experiments at those specific temperatures. The y-axis, normally, gives the number of experiments cumulatively added to one another from bottom to top. The correlation is given below (Figure 2.10).
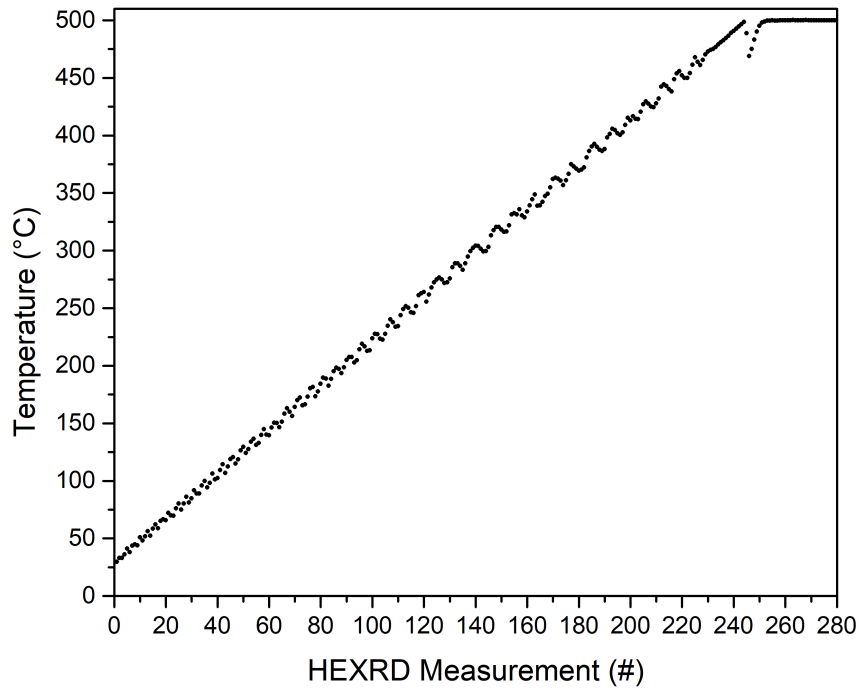
Figure 2.10 Corresponding temperatures of each HEXRD run

Indexing the fcc-Al and trigonal IM was relatively straightforward with the current literature. The space group of fcc-Al is $Fm\bar{3}m$ with a space group number of 225, and the space group of trigonal β-Al₃Y is $R\bar{3}m$ with a space group number of 166. However, no strong evidence for the tetragonal phase was found in the literature. For this reason, DICVOL simulations [35] were run on the HEXRD data. The unmatched interplanar spacing values were measured from the spectrum. They were put into DICVOL, and all the Bravais lattices except monoclinic and triclinic were searched. The only possible structure was a tetragonal lattice with a strong match. The indexed hkl values with the interplanar spacings, including the deviation from the theoretical values, were given below (Table 2.2). At this point, the unmatched phase was identified as tetragonal.

Table 2.2 Indexed hkl values for the tetragonal IM phase, including its interplanar spacings and deviations from the calculated interplanar spacing data as % error

hkl	d (Å)	% error
002	4.86	0.23
101	3.88	0.20
110	2.99	0.31
103	2.57	0.03
112	2.54	0.99
103	2.57	0.74
112	2.54	0.21
004	2.43	0.15
104	2.1	0.29
200	2.11	0.13
005	1.94	0.04
202	1.94	0.16
114	1.88	0.17
210	1.89	0.50
211	1.85	0.29
105	1.76	0.38
203	1.77	0.08
212	1.76	0.54
006	1.62	0.81
115	1.63	0.17
213	1.63	0.07
204	1.59	0.18
214	1.49	0.02
220	1.49	0.23
116	1.42	0.13
205	1.43	0.61
222	1.43	0.51

After simulations, it is concluded that the formed IM phase after the crystallization of fcc-Al has a tetragonal crystal structure with a possible composition of $Al_{1-x}Y_x$. It should be noted that the tetragonal systems have space group numbers between 75 – 142. Since the space group numbers are increasing from 0 to 230 with an increased symmetry, it can be argued that the first IM that the MMG devitrified into is less

ordered than the second one. The trigonal β-Al$_3$Y phase with 166 space group is more ordered than the tetragonal one. Therefore, the symmetry in the overall system is increased as the temperature increases. In the end, the following devitrification sequence was determined.

$$Amorphous \rightarrow fcc - Al \rightarrow fcc - Al + Tetragonal\ IM$$
$$\rightarrow fcc - Al + \ Trigonal\ IM$$
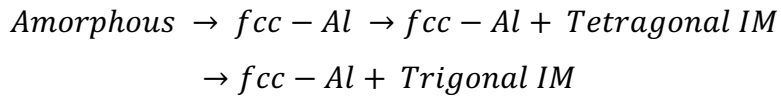
The decomposition of the amorphous phase into these crystalline products will eventually end with the formation of the liquid. Since the experimental setup at the MSPD beamline was not suitable for the liquid state characterizations, the heating was cut at 500 °C. In the meantime, a DSC experimentation with a heating rate of 40 °C/min validates the same devitrification sequence as the synchrotron studies (Figure 2.11). A DSC trace of the same material shows the formation of devitrification products fcc-Al, tetragonal IM, and trigonal IM.
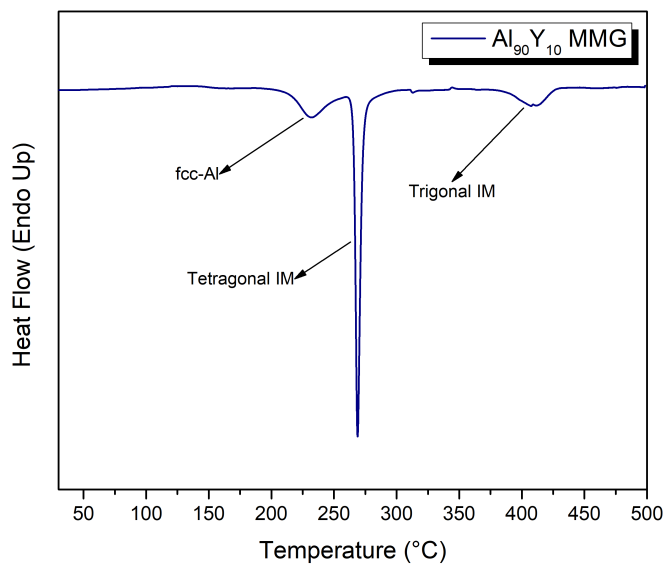
Figure 2.11 DSC trace of a melt-spun Al$_{90}$Y$_{10}$

When the DSC trace is analyzed in detail, an interesting signal is seen just before the crystallization of fcc-Al nanocrystals (Figure 2.12). The nucleation of fcc-Al begins near 195 °C for the 40 °C/min heating rate. Just before its formation, another reaction with an onset of 140 °C is occurring. It is more dominant at higher heating rates and cannot be resolved easily for lower heating rates. Although it is similar to the glass transition, it is definitely not since the glass transition is an endothermic event. One should also note that this type of signal is exclusive to the Al-Y system, and it is not seen at different Al-based MMGs, like Al-Tb and Al-Sm.
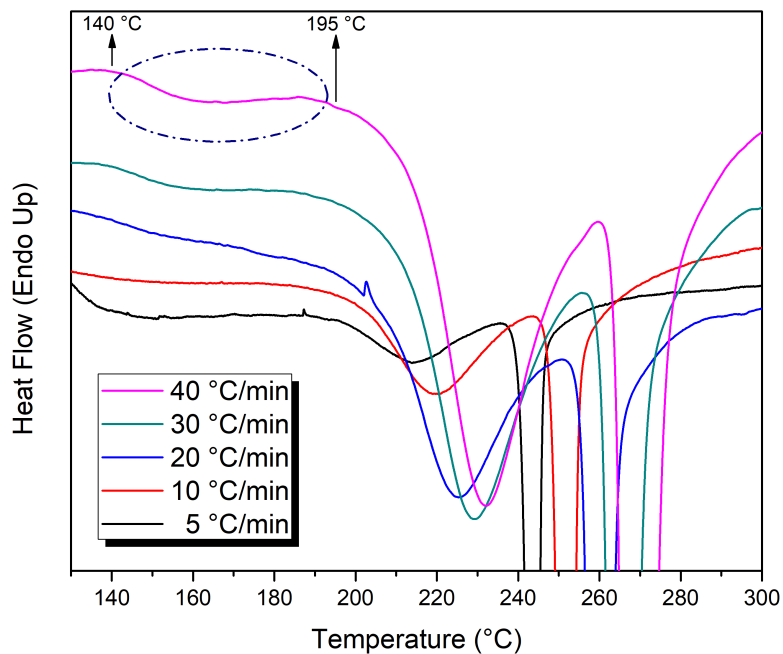
Figure 2.12 Zoomed DSC traces of melt-spun $Al_{90}Y_{10}$ with different heating rates

This signal was associated with either phase separation in the amorphous state or the existence of a highly metastable phase within a very short time domain. It was argued that the observed reaction might have a spinodal decomposition nature. One possibility is that the amorphous phase decomposes into two different phase configurations just before the crystallization of the fcc-Al. The other possible

explanation is that one of the highly populated clusters with a high number of atoms acted as a seed and just bonded with a few new atoms during heating and satisfied r* so that it has nucleated. The heterogeneity in the amorphous phase is prominent for MMGs, and the distribution and diffusion of the atoms may yield such phenomena. If the path of diffusion has interacted with these near-r* clusters, a highly metastable phase may form and disappear. When the diffusion continues, these nuclei break their bondings with these moving atoms and become extinct again. All in all, further investigations are necessary to support these ideas and explain this phenomenon. Note that this DSC signal could not be associated with any features from the HEXRD, but it exists one way or another since it is observed and validated at multiple tries. The reason why the phase provoking this DSC signal was not observed by HEXRD can be the corresponding Q-range of the HEXRD experimentation. If the formation mechanism of this phase has a chemical and spinodal decomposition nature, the corresponding Q-range might not be enough to resolve this phase formation. Lower Q-range coverage might be necessary to resolve this phase formation. For this purpose, small-angle X-ray scattering (SAXS) experiments should be conducted. It is also logical if the resultant phase of this transformation/separation is based on the chemical decomposition and has higher d-spacing values.

2.3.4   Analytical Electron Microscopy Studies

The structure of the amorphous phase and the first devitrification products were characterized using TEM. The initial melt-spun $Al_{90}Y_{10}$ ribbon was prepared by electropolishing and analyzed using bright-field imaging (Figure 2.13). The BF image indicates no crystalline features. Also, the selected area electron diffraction pattern shows a characteristic amorphous signal with no crystalline spots. Therefore, the amorphous nature of the melt-spun $Al_{90}Y_{10}$ ribbon was once more validated.
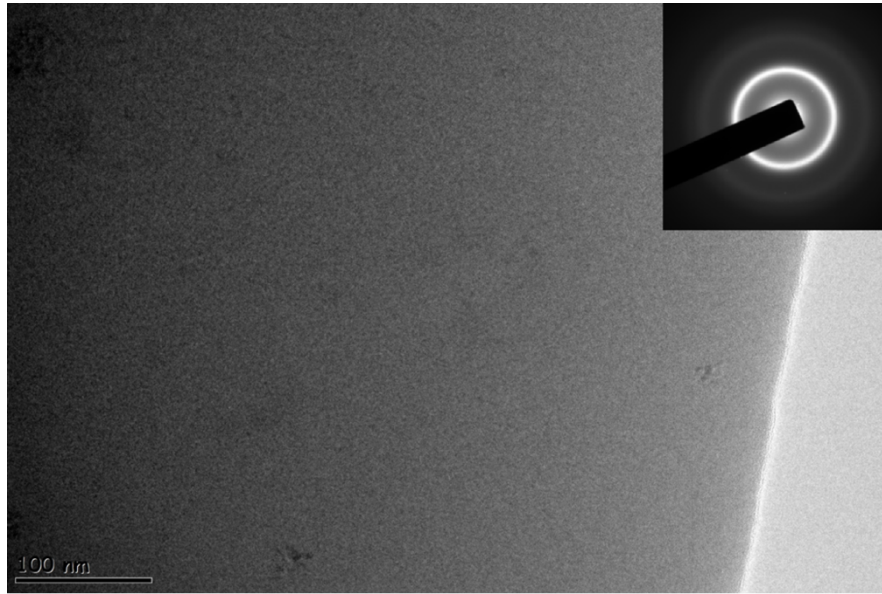
Figure 2.13 BF imaging of as-spun $Al_{90}Y_{10}$ ribbon. Inset shows the corresponding SAED pattern

After that, the DSC device was used as a controlled furnace. TEM specimens were prepared to investigate the structure of the devitrified material at specific temperatures. The specimens were heated to certain elevated temperatures, and then an interrupted quenching procedure was applied to freeze the microstructure. The first material to be investigated was chosen as the material that gives a phase transformation signal at DSC (Figure 2.12). Therefore, the material was heated up to 165 °C, where the unknown phase should be in the middle of its formation. When the BF-TEM image was investigated, the structure seemed amorphous but with a slight contrast that indicates heterogeneity (Figure 2.14). Moreover, the corresponding SAED pattern indicated a fully amorphous microstructure. However, interestingly, the HRTEM images revealed a type of lattice fringes that indicates a crystalline phase (Figure 2.15) (Figure 2.16). Since the SAED pattern shows only an amorphous signal, this was quite unexpected. How has the SAED pattern obscured such a crystalline phase? One possible answer to this question is that the crystalline phase exists in a trace amount. It is rather possible since most of the HRTEM images indicated an amorphous configuration.
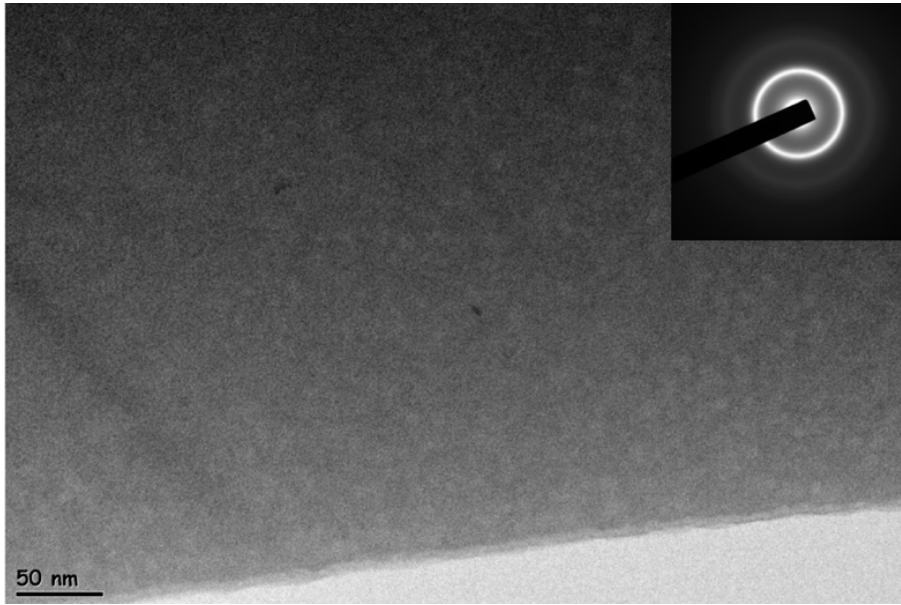
Figure 2.14 BF-TEM image of the $Al_{90}Y_{10}$ specimen heated up to 165 °C. Inset shows the corresponding SAED pattern
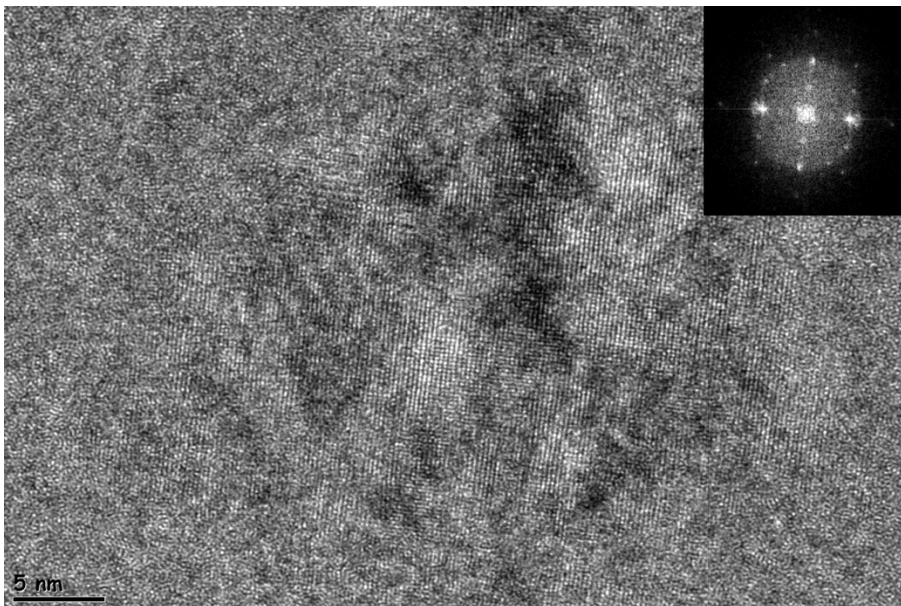
Figure 2.15 HRTEM image of the unknown crystal. Inset shows the FFT pattern processed from this crystal
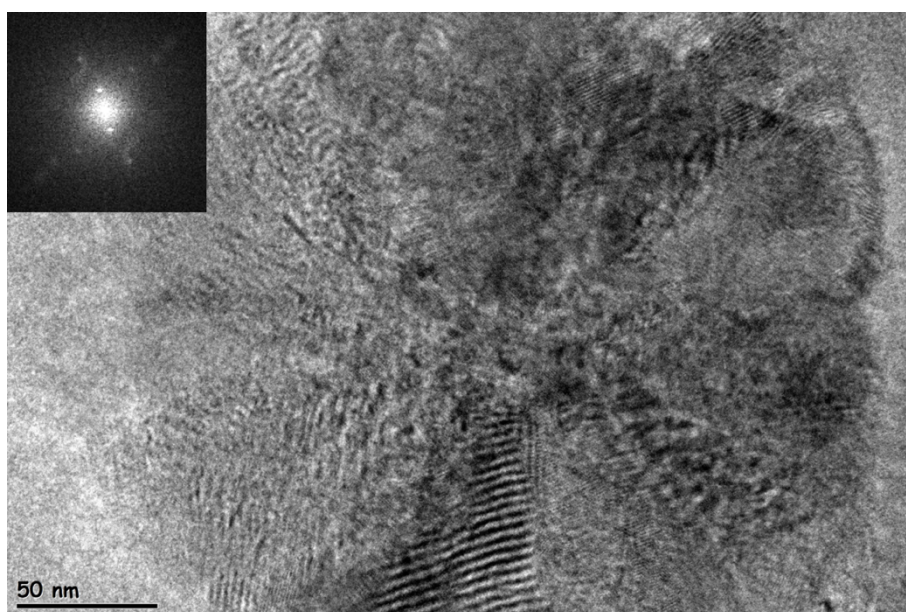
Figure 2.16 HRTEM image of the unknown crystal. Inset shows the FFT pattern of this crystal. Note that the FFT signal is highly affected by the Moiré fringes

To identify this crystal, the distances between the spots through the transmitted beam at the FFT signal were measured. These reciprocal space lengths were converted to real space distances. After this conversion, the corresponding interplanar spacing values were put into DICVOL simulations [35]. The simulations have found 9 different solutions for the structure. Eight of them were orthorhombic, while one of them was hexagonal. However, one of the orthorhombic solutions had a considerably higher figure of merit (FOM). Although the hexagonal structure is more symmetrical than the orthorhombic one, the solution for the hexagonal one has occupied more than 4 times of volume in the space. This is most probably the reason for the higher FOM for the orthorhombic structure. At this stage, both the less symmetrical orthorhombic with high FOM and the very high volume hexagonal with high symmetry can be the solution for this crystal. Since there is no evidence of such transformation in the literature, further investigations are necessary to identify its true structure.

Later, a specimen heated up to the mid-point of the fcc-Al crystallization signal was investigated. This time, an amorphous matrix was surrounded by highly populated crystals (Figure 2.17). The population of these crystals indicated a high nucleation density, as in the case of other Al-RE MMGs. When the SAED pattern was indexed, it was figured out and correlated that the formed crystals were fcc-Al, as expected. Another BF-TEM image was taken from a grown crystal. The spot pattern was collected from its <110> zone axis. It was also identified as an fcc-Al phase (Figure 2.18). A further HRTEM analysis shows lattice fringes of a fcc-Al nanocrystal with higher magnifications (Figure 2.19).
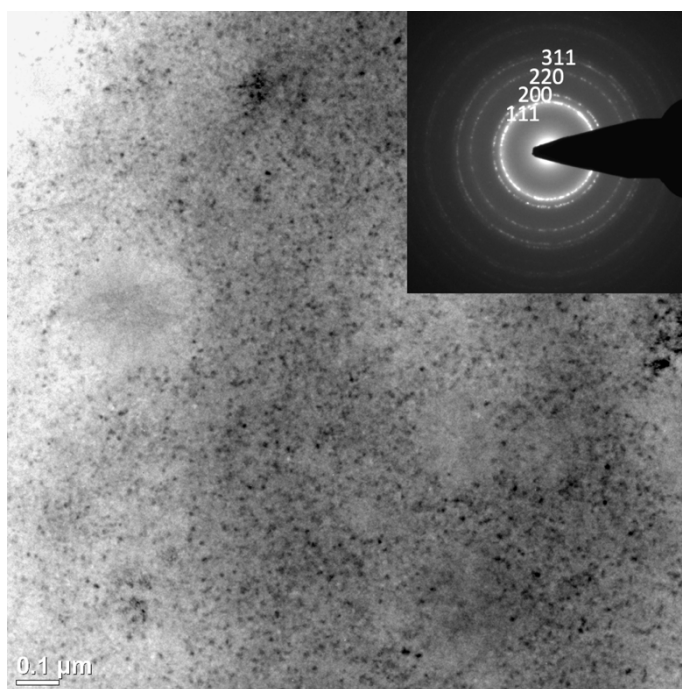
Figure 2.17 BF-TEM imaging of the amorphous matrix nanocrystalline $Al_{90}Y_{10}$. Inset shows the corresponding SAED pattern
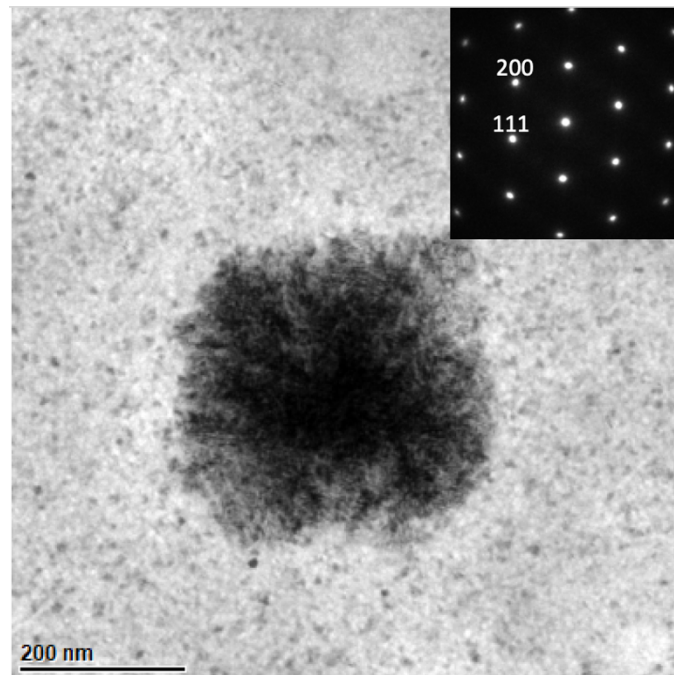
Figure 2.18 BF-TEM shows a grown fcc-Al crystal. Inset shows the corresponding spot pattern collected from its <110> zone axis
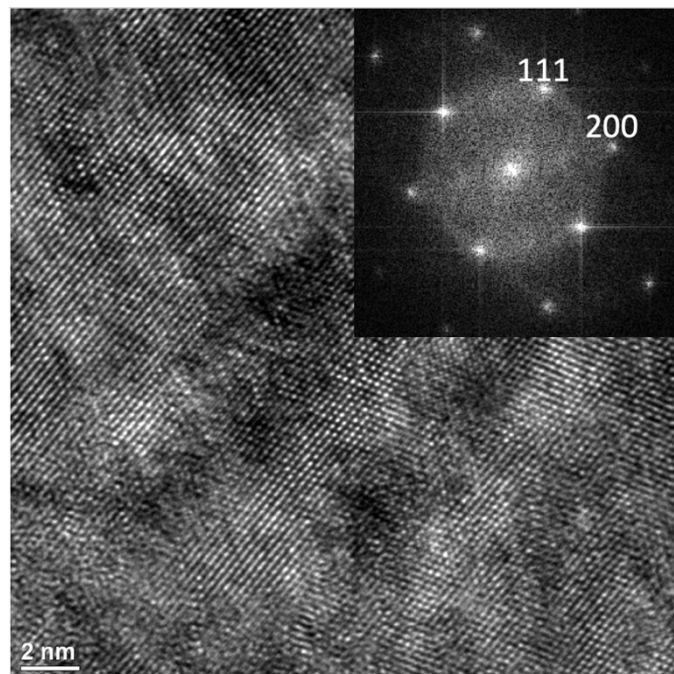
Figure 2.19 HRTEM image of the fcc-Al nanocrystal. Inset shows the indexed FFT pattern of this crystal

As a further investigation, an EDS mapping was done to this specimen in STEM-HAADF mode (Figure 2.20). The results were in good agreement with the crystallographic analysis. The devitrification product, fcc-Al, can also be identified from this chemical analysis. As can be seen from Figure 2.20, these crystals contain Al. Furthermore, the amorphous matrix is very rich in RE. This is particularly important since, during the devitrification of an Al-RE MMG, the yttrium atoms were rejected by the Al-rich clusters. Then, the consumed amorphous phase during the crystallization of the Al-rich nuclei becomes rich in yttrium. The continuation of this process yields higher Y content in the amorphous phase and causes a soft impingement. The severe soft impingement eventually restricts the growth and controls the morphology of the fcc-Al crystals, which yields a homogeneous distribution and a spherical shape of the crystals. Of course, this impingement effect between the fcc-Al crystals and the RE-rich amorphous phase is related to the medium-range ordered nearly pure Al domains and the RE-rich clusters in the initial amorphous configuration of this MMG.
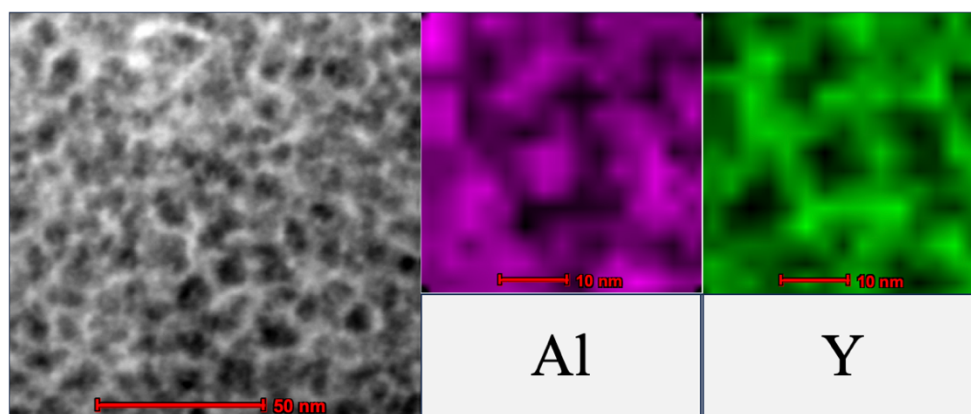
Figure 2.20 Elemental mapping of the amorphous matrix nanocrystalline $Al_{90}Y_{10}$ collected with STEM-HAADF imaging

2.3.5   Effect of Laser Ablation on the Structure

Now, the question becomes, does the atomic configuration of Al-Y MMG also change with parental states and undercooling levels? For this reason, for the first time in the literature, an Al-based marginal metallic glass was produced with a laser ablation method. A laser ablation with a femtosecond pulse capability was used at the UNAM facility. The production was done by U. Taylan from the Ortac Group.

Until today, the effect of solid, liquid, and gaseous precursors was investigated for the MMGs. For the first time, the effect of plasma precursor was investigated with this production route. When a laser pulse is focused and hits the specimen in an inert liquid solution, the localized heat converts the material into plasma. Later, the material solidifies in nanoscale powder form inside the solution. During this process, the cooling rate exceeds 10^{12} K/sec [36]. Therefore, this method should be suitable for MMG production. The initial results were obtained by XRD using Cu K$_\alpha$ (Figure 2.21). The laser-ablated solution was dropped onto a silicon wafer, and the wafer was dried. XRD of an empty Si wafer was also taken to be subtracted from the original data. The result of the performed XRD experiment was rather featureless, indicating a possible amorphous phase formation. Also, there were two distinguishable sharp peaks in the data. These two peaks were related to an intermetallic (IM) phase. Although one needs more peaks to match the exact phase, the peaks had a good match with the Al$_2$Y Friauf-Laves phase. This phase is also identified as a Frank-Kasper phase [33]. It should be noted that the precursor Al$_{90}$Y$_{10}$ specimen for the ablation was produced with a vacuum arc-melter. Therefore, the initial as-cast structure was crystalline and had grown dendrites in it. Also, its composition was validated using EDS. Since the area of the surface on which the laser was focused was a few microns, it is possible that the plasma composition deviated locally during the movement of the laser. Hence, RE-rich parts in the microstructure may preferentially solidify into an IM phase rather than an amorphous state. It is also logical considering the GFR of the Al-Y system. If the yttrium content

is higher than 13 at%, it is beyond the GFR and should not have an amorphous phase, according to Inoue [19].
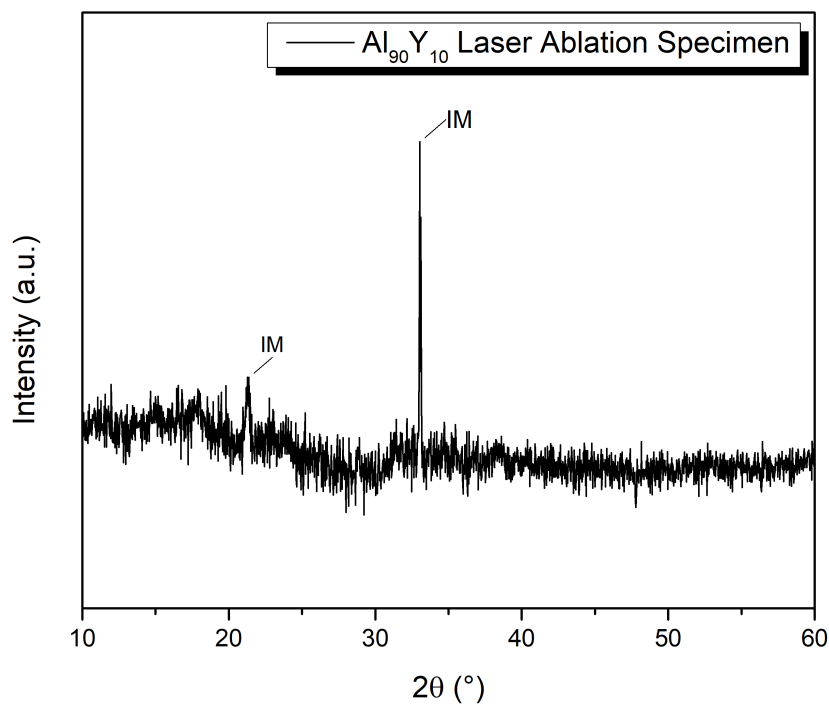
Figure 2.21 XRD result of the laser ablated $Al_{90}Y_{10}$ specimen (IM: intermetallic phase)

Later, the produced solution was investigated using TEM (Figure 2.22). There were aggregated nanoscale powders in the BF image. Although the overall signal was weak in the SAED pattern, it was concluded that the powders were possibly in an amorphous state since there was no hint of crystalline spots.
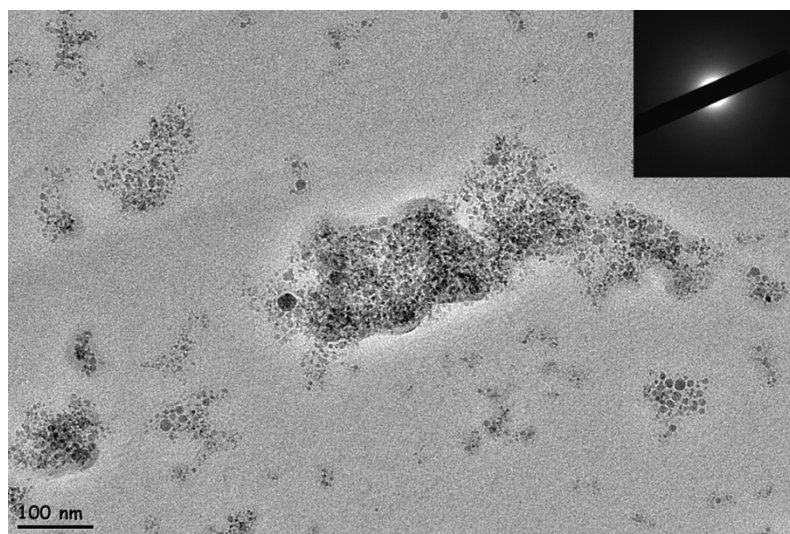
Figure 2.22 BF-TEM image of a laser ablated $Al_{90}Y_{10}$. Inset shows the corresponding SAED pattern

The HRTEM image validates the aggregated nanoscale powders seen in the BF image. (Figure 2.23). The FFT processing of the powders revealed the possible amorphous nature. The pattern, again, did not contain any crystalline features.
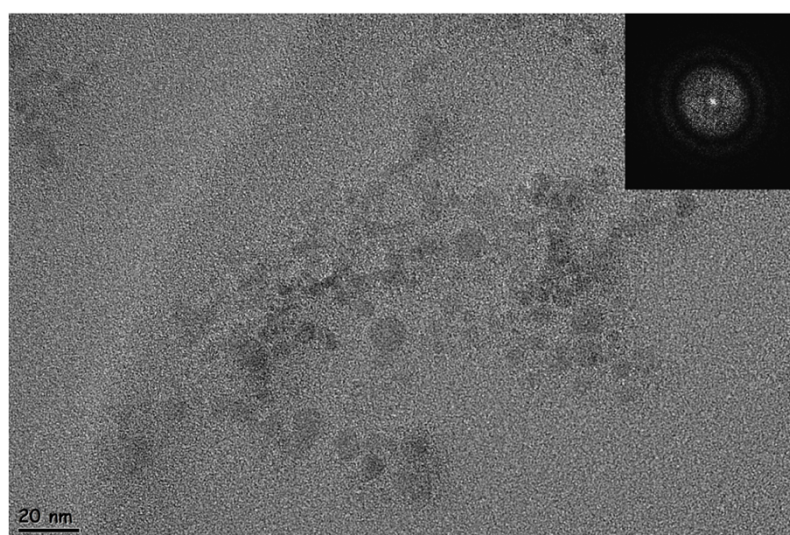
Figure 2.23 HRTEM image of the laser ablated specimen. Inset shows the FFT pattern from the powders

Interestingly, EDS showed that the composition of the laser-ablated powders was shifted incredibly from the initial composition. A slight shift to the Al-rich compositions for the amorphous phase was expected, considering the RE-rich phase formation observed during XRD analysis. However, the shift was beyond the GFR of the system. The average composition of the amorphous material was $Al_{97}Y_3$ (Table 2.3). Hence, nearly pure amorphous Al with 3 at% Y was obtained with laser ablation. It should be noted that this is way beyond the predictions of Inoue [19].

Table 2.3 Average of the EDS analyses collected during the TEM investigation of laser-ablated Al-Y

Composition of the laser-ablated Al-Y MMG (at%)	
Al	~97
Y	~3

This tendency was correlated with the cooling rate of femtosecond pulsed laser ablation. Since it is millions of orders of magnitude higher than the required cooling rate for MMG production, it should yield extensively higher undercooling. The undercooling must be so high that the normally crystalline-expected composition was frozen into an amorphous state. Nevertheless, further investigations are necessary to discover the effects of laser ablation on amorphous metal formation and its possible ordering. One should also note that the amount of the produced particles were too less and the data collection was weak for the XRD and SAED experiments since there was no distinguishable amorphous signal.

CHAPTER 3

CRYSTALLIZATION KINETICS DURING THE DEVITRIFICATION OF MARGINAL METALLIC GLASSES

3.1   Introduction

In this chapter, the crystallization kinetics of marginal metallic glasses was investigated in detail, with the help of thermal characterizations. Among Al-based marginal glass formers, the Al-Y system was chosen for this analysis. In the literature, crystallization kinetics of MMGs were investigated for the other Al-RE systems, such as Al-Tb, Al-Sm binaries, and Al-Sm-Tb ternary [23,26]. Therefore, the aim of this chapter is to combine the recent findings from the Al-Y system and the literature to make a comprehensive discussion on this topic. As a result, the influence of the crystallization kinetics of a highly driven glassy alloy on its emerging properties was tried to be revealed. By doing this, the effect of local atomic orders on the crystallization kinetics was also discussed.

3.2   Experimental Procedure

Thermal analyses were conducted using DSC. As in the previous chapter, a ribbon melt-spun $Al_{90}Y_{10}$ marginal metallic glass was produced by a single block Cu wheel melt spinner with a tangential speed of 30 m/s under the He atmosphere. The samples were produced at the Materials Preparation Center of the Ames Laboratory, USA, and the composition of the alloy was determined by WDS and EDS.

DSC analyses were done with various heating rates to make necessary kinetics calculations. The heating rates were decided as 5, 10, 20, 30, and 40 °C/min. For these experiments, the Perkin Elmer Diamond differential scanning calorimetry from

METU Central Laboratory was used. Reference sample measurements with an empty Al pan were also taken for the baseline correction. All of the DSC experiments were conducted with 10 mg of rectangularly cut ribbons. They were inserted in Al pans, and the pans were covered with Al lids. Experiments were conducted in an N_2 atmosphere, and the isochronal heating traces were recorded and analyzed.

3.3   Results and Discussions

3.3.1   DSC Analyses

DSC traces recorded with 5, 10, 20, 30, and 40 °C/min heating rates from room temperature to 500 °C can be seen below (Figure 3.1).
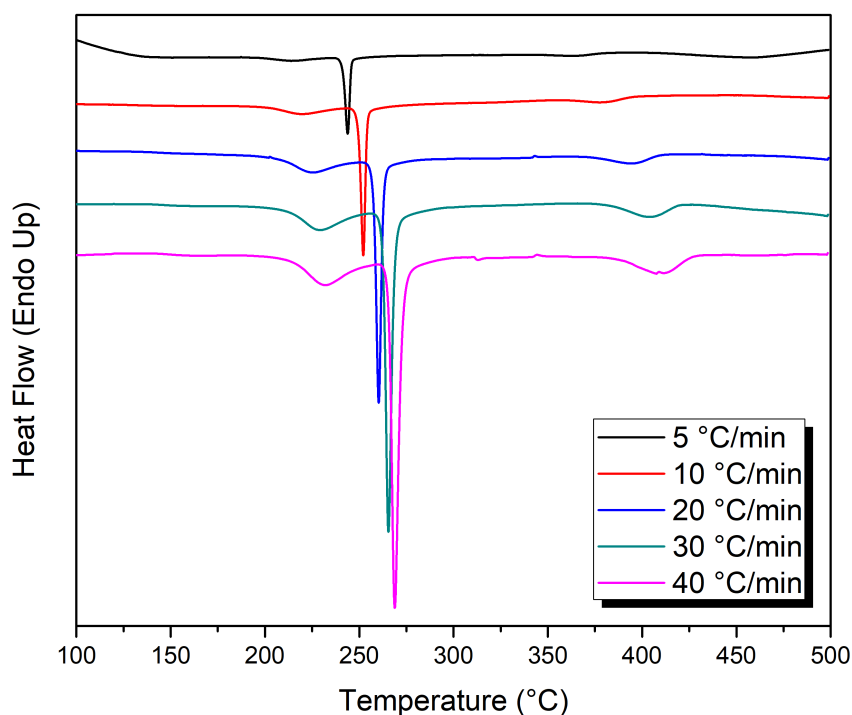
Figure 3.1 DSC traces of $Al_{90}Y_{10}$ with various heating rates

For this study, the crystallization of the fcc-Al was investigated in detail. The regions where the fcc-Al is crystallized can be seen below (Figure 3.2).
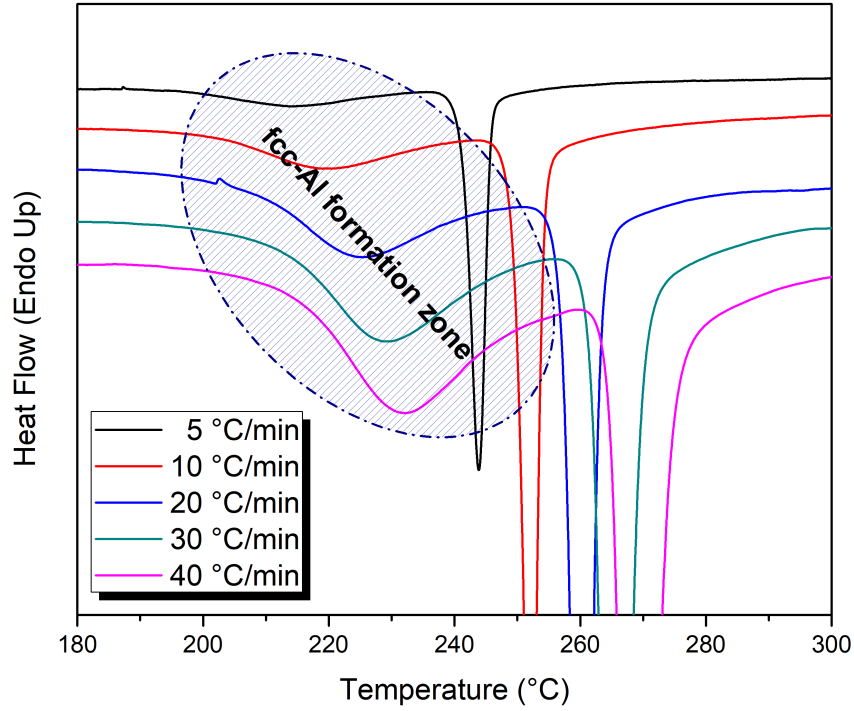
Figure 3.2 Formation zone of the fcc-Al for the $Al_{90}Y_{10}$

3.3.2 Kissinger and Ozawa Analyses

To establish a well-built kinetics model, a widely used Kissinger analysis was performed [37,38]. The following equation was used for various heating rates.

$$\ln\left(\frac{\beta}{T(x)^2}\right) = \frac{E_c(x)}{RT(x)} + \ln\left(\frac{E_c(x)}{k_0 R}\right)$$

As a result, $\ln(\beta/T^2)$ vs. $1000/T$ curves were obtained (Figure 3.3). From these curves, activation energies for the devitrification products were calculated and tabulated (Table 3.1).
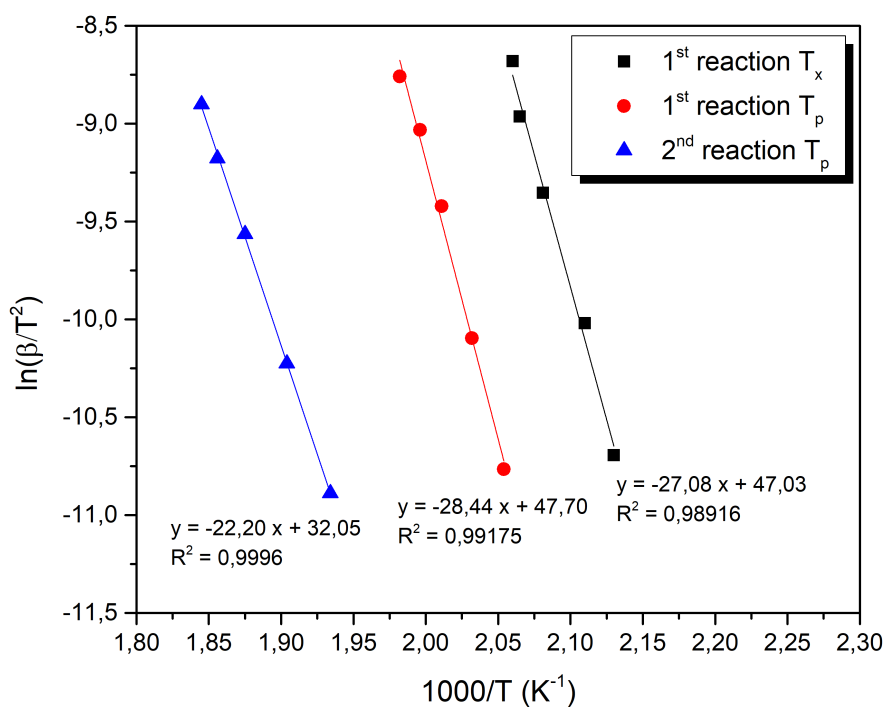
Figure 3.3 Kissinger Analysis of $Al_{90}Y_{10}$

Table 3.1 Calculated activation energies of the first and the second exothermic reactions of the $Al_{90}Y_{10}$ specimen using Kissinger's method

Kissinger E_c (kj/mol)	
T_{X1}	224
T_{P1}	236
T_{P2}	185

The findings of the Kissinger analysis were crosschecked with the results coming from the Ozawa analysis [39,40]. For this method, the following equation was used to interpret the data.

$$\ln(\beta) = -1.0516 \frac{E_c(x)}{RT(x)} + C$$

After the calculations, the results of the Ozawa analysis were plotted (Figure 3.4). Also, the calculated activation energies from the Ozawa analysis were tabulated (Table 3.2).
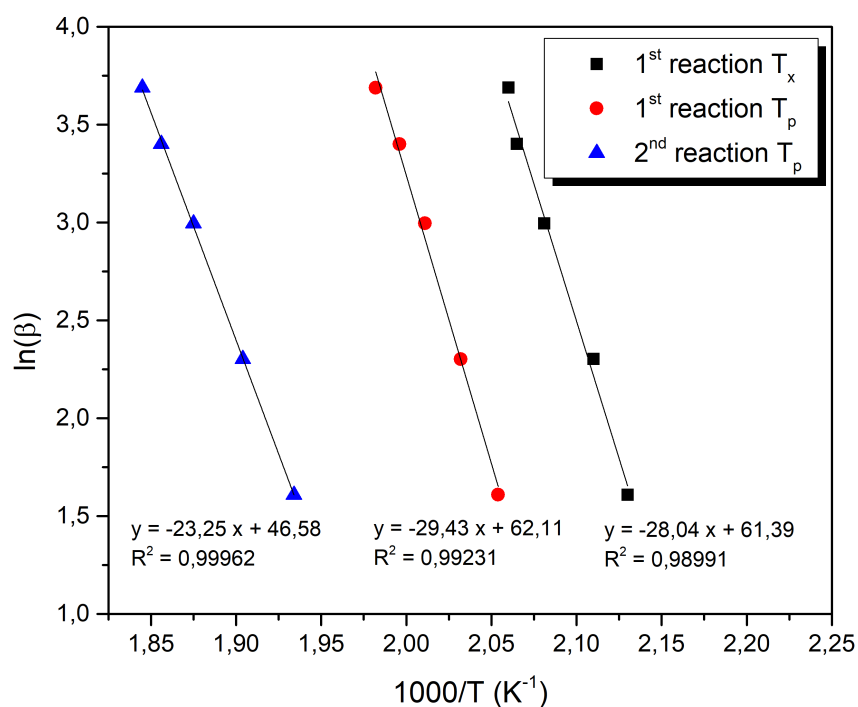
Figure 3.4 Ozawa Analysis of $Al_{90}Y_{10}$

Table 3.2 Calculated activation energies of the first and the second exothermic reactions of the $Al_{90}Y_{10}$ specimen using Ozawa's method

Ozawa E_c (kj/mol)

T_{X1}	232
T_{P1}	244
T_{P2}	194

When these values are compared with the other Al-RE MMG systems, it was found that the required energy for the fcc-Al crystallization is around the same as the other systems. It was known that the nucleation density for fcc-Al is orders of magnitude higher than the predictions of classical nucleation density for these systems. Considering the TEM images in the previous chapter and this similar activation energy that is calculated, it can be easily said that the same thing is also valid for the Al-Y system. The comparison of the activation energies for the fcc-Al crystallization event of Al-based MMGs can be seen below (Table 3.3).

Table 3.3 Comparison of the calculated activation energies for fcc-Al crystallization in different compositions

Al-based MMG	Kissinger E_c (kj/mol)	Ozawa E_c (kj/mol)
$Al_{90}Y_{10}$	236 ± 7	244 ± 6
$Al_{90}Tb_{10}$ [41]	298 ± 1	291 ± 1
$Al_{90}Sm_{10}$ [20]	171 ± 3	171 ± 2
$Al_{90}Sm_5Tb_5$ [42]	289 ± 9	282 ± 9

One of the main effects that determines the activation energy of fcc-Al is the RE content of the amorphous matrix. The type and the amount of RE elements in the matrix determine the local and general chemical instability of the system. When heat is induced in the system, the diffusion of the atoms lets the Al-rich clusters gain new

Al atoms so that they have enough activation energy to overcome the surface generation and exceed r*. The diffusivity of the Al and RE alloys is the other important factor. The formation of the crystalline product is affected by how easily the atoms can diffuse. This is directly related to the kinetics of the crystalline phase formation. Diffusion barriers and the path of diffusion may also be affected by the medium-range ordered clustering on the system. If the system has a network of near-r* Al-rich clusters surrounded by RE atoms, it can easily have crystalline products during devitrification since a small amount of heat would be enough to collect the necessary number of Al atoms in those near-r* Al clusters. Therefore, the cooling rate and the given undercooling to the system during its first MMG formation are also critical factors in determining its activation energy for the fcc-Al crystallization. If the cooling rate is high, the given undercooling, which eventually affects the local atomic ordering, is also high. If the amorphous phase has a higher degree of short to medium-range ordering, the structural relaxation of the system will be easier to happen. Also, when the activation energy for the crystallization is lower, it means that the total structural relaxation of the system would be higher. When compared with the other Al-RE marginal glass former systems, it is seen that the Al-Y system has similar behavior and a tendency for fcc-Al crystallization. Note that the activation energy for the lattice self-diffusion of Al is around 143 kj/mol [43].

CHAPTER 4

MECHANICAL PROPERTIES OF MARGINAL METALLIC GLASSES

This chapter is submitted as a research paper to a journal. The work contained in this chapter is conducted by Can Okuyucu (the writer of this thesis and the first author of the paper), as well as the authors Tolga Han Ulucan, Mohammad Abboud, Amir Motallebzadeh, Sezer Özerinç, İlkay Kalay, and the thesis supervisor Yunus Eren Kalay. Micromechanical characterizations were done by Mohammad Abboud, Amir Motallebzadeh, and Sezer Özerinç. Since this was an ongoing study, part of the figures, results, and data was also included in the thesis of Tolga Han Ulucan, published in 2020 [44]. After the detailed investigation of amorphous and devitrified phases in the previous chapters, several micro and nanomechanical characterizations and TEM investigations were carried out in order to broaden our understanding of the emerging properties of MMGs. In this chapter, the emerging properties are investigated and explained by relating them with the medium-range ordered amorphous configuration and the crystallization during devitrification. For this purpose, a well-studied MMG in our group, $Al_{90}Tb_{10}$, was chosen.

Rare Earth (RE) metallic glasses provide an effective model system to study the effect of nanocrystallites in an amorphous matrix on nanomechanical behavior. In this work, we achieved a series of Al-Tb metallic glass-crystalline composites with systematically varying crystalline content through annealing. The nanomechanical properties were detected using micropillar compression tests and nanoindentation for as-quenched amorphous and annealed amorphous/nanocrystalline composite specimens. The promising hardness increase after annealing from 2.8 GPa to 4.3 GPa and elastic modulus increment from 68 GPa to 92 GPa were discussed in detail, considering the structural features of Al-RE marginal metallic glass formers. The

increase in elastic modulus is associated with the nucleated fcc-Al nanocrystals that divide the amorphous matrix and thus cause branching of the shear bands. The correlation between the fcc-Al nanocrystals and the behavior of shear bands was discussed in detail.

4.1   Introduction

Al-Rare Earth (RE) metallic glasses have been the subject of recent research due to their unique crystallization products and peculiar devitrification behaviors [20,23–26,28–30]. For instance, the number of fcc-Al nanocrystals after the first devitrification event can reach 10^{25} crystals/m^3 [25,26,45] in the amorphous matrix. This value is orders of magnitude higher than the predictions of the classical nucleation theory [27]. A similar difference in crystal number density between the calculations and the experimental results has also been observed for other metallic glass systems [46]. In this respect, scientists have studied them many times [21,45,47–51]. The potential benefits of nanocrystal-embedded metallic glasses, i.e., high strength, toughness, and elasticity [19,52–59], motivate further studies to understand the alloy systems comprehensively.

The mechanical deformation of metallic glasses is primarily governed by shear band formation and propagation [60–64]. In amorphous metals, shear band formation and propagation take tremendous attention in materials science and solid-state physics. Particularly in marginal glass former systems, the nature of shearing in nanocrystal-embedded amorphous matrix remains enigmatic, primarily due to the elusive experimental requirements. Preparation of the marginal metallic glass, the suitable mechanical test specimen, and the suitable specimen for further characterization are all thorny and formidable steps for these types of studies. Even at the end of the first production, the specimens are no thicker than tens of microns. Traditional mechanical testing methods remain inadequate for these types of undersized ribbon specimens. For this purpose, micropillar compression and nanoindentation methods are often used. Previous studies show that the supersaturated solid solution form of

these Al-RE alloys with rapid solidification has almost a record hardness value among the Al alloys by nanoindentation testing [31]. These results for the crystalline far-from-equilibrium marginal glass former systems have drawn attention to the amorphous state of these alloys.

Scientists have widely investigated the shear phenomenon during the fracture of amorphous metals to correlate the mechanical properties and underlying mechanisms. Most studies focus on free volume change, dilatation, local viscosity changes, adiabatic heating, and the crystallization phenomena in these regions [65–70]. Spaepen et al. conducted several HRTEM analyses in the shear zone and observed an excessive void formation [67]. They concluded that the voids were formed due to the coalescence of excess free volume during deformation. Later, Yan et al. explained the crystallization phenomena near shear zones based on the polyhedral structure model and the viscous flow and free volume change in the shear transformation zone [65]. They argued that the nucleation activation energy in the transition regions near shear bands is much lower due to the compression effects [65]. From this aspect, they explained the preferential nanocrystallization by the inhomogeneous deformation during shearing. A similar study by Yan et al. found evidence of the precipitation of icosahedron-like clusters in these transition zones between the amorphous structure and the shear band [71]. Meanwhile, several studies explained the crystallization during shearing by the adiabatic heating phenomenon [70]. In contrast, other studies claim that the temperature increase due to adiabatic heating is insufficient to crystallize a new phase [72], whereas some studies support both of these ideas. Jiang et al. conclude that the nanocrystals formed in the compressive regions near shear bands are due to the kinetic effect, while the nanocrystals formed at the fracture surfaces are due to the adiabatic heating [73].

In this study, the behavior of shear band propagation is investigated in a nanocrystal-embedded marginal metallic glass matrix $Al_{90}Tb_{10}$ alloy. The influence of the as-quenched amorphous structure and the effect of nanocrystal evolution after annealing on the nanomechanical properties were also studied.

4.2   Experimental Procedure

Al-RE binaries were chosen as a model system to investigate the shear band mechanisms in both the fully amorphous state and the amorphous matrix-nanocrystalline state. Amorphous $Al_{90}Tb_{10}$ alloys were produced in ribbon form with the melt spinning using a water-cooled single-block Cu wheel. The tangential speed of the melt spinner was 30 m/s, and the production was done in the Ar atmosphere to prevent oxidation. The melt-spun ribbons had 2 to 3 mm in width and a thickness range of 30 – 50 μm.

The ribbon specimens were analyzed by an FEI Nova NanoSEM 430 scanning electron microscope (SEM). The composition of each specimen was verified by energy-dispersive X-ray spectroscopy (EDS).

A Seiko SII X-DSC7000 differential scanning calorimeter (DSC) was first utilized to determine the critical transformation temperatures by first heating – cooling – second heating cycles. Based on this data, DSC was then used as a controlled furnace to achieve certain levels of heat treatments on initially amorphous samples. This approach provided specimens with pre-determined temperatures to achieve samples with different stages of crystallization. For these experiments, 10 mg ribbons were inserted in Al pans and covered with Al lids. Measurements on an Al pan without any specimen served as reference samples and were used for baseline correction. All isochronal annealing experiments were done at 40 °C/min heating rates in an N_2 atmosphere. When the specimens reached critical temperatures, an interrupted quenching procedure was applied to freeze the structure accordingly. The DSC treatments supplied five samples – one with a fully amorphous microstructure and four with different amounts of crystalline phases, as summarized in Table 1.

Mechanical testing consisted of nanoindentation measurements and micropillar compression experiments. Nanoindentation tests employed An Agilent G200 Nanoindenter with a Berkovich tip. Due to the smooth surfaces on the air side of the specimen, there was no need for any surface preparation. The nanoindentation

measurements employed a strain rate of 0.05 s^{-1}, defined as the displacement rate of the indenter tip normalized by the penetration depth. This approach resulted in an increasing displacement rate, aiming at maintaining a relatively constant displacement rate over the increasing volume of plastic deformation. The measurements were performed in continuous stiffness measurement mode, which provided means for obtaining hardness and elastic modulus as a function of depth. Nanoindentation tests were repeated in at least 12 locations to get statistically significant data.

The micropillars used in mechanical testing were milled by an FEI Nova 600 Nanolab (OR, USA) focused ion beam (FIB) on the air-side surface of the melt-spun samples. The micropillars had nominal dimensions of 3 μm in diameter and about 7.5 μm in height. The same nanoindenter used for the indentation experiments was equipped with a flat diamond punch to perform the compression tests on the samples. The measurements employed displacement control with linear loading and unloading stages. Loading rates provided a strain rate of 5×10^{-4} s^{-1}.

Transmission electron microscopy (TEM) was performed on the cross-sections of selected micropillars upon deformation. The lift-out technique was employed using the same FIB that produced the micropillars. These specimens were analyzed with a JEOL JEM 2100F transmission electron microscope (TEM) in bright field (BF), high-resolution transmission electron microscopy (HRTEM), and selected area electron diffraction (SAED) modes. Microscopy data were further analyzed with Gatan Digital Micrograph GMS 3 software.

4.3   Results and Discussions

The below figure shows the initial DSC experiments, revealing the critical temperatures for the related phase transformations (Figure 4.1). Previous studies on Al-Tb marginal metallic glasses validate the first two transformation signals as fcc-Al crystallization and intermetallic formation [26,30].

Based on the data presented in Figure 4.1, specimens for microstructural and mechanical analyses were prepared by controlled heat treatments with interrupted quenching experiments. The annealing aimed at achieving a range of microstructures, namely, a fully amorphous structure, fcc-Al nanocrystals embedded in an amorphous matrix, and a more complicated structure including intermetallic phases in addition to crystalline and amorphous domains. This was achieved by encapsulating the amorphous specimens in DSC holders, heating them to the temperatures designated in Figure 4.1, and quenching them to room temperature. The table summarizes the details of specimens heat-treated under different conditions (Table 4.1).
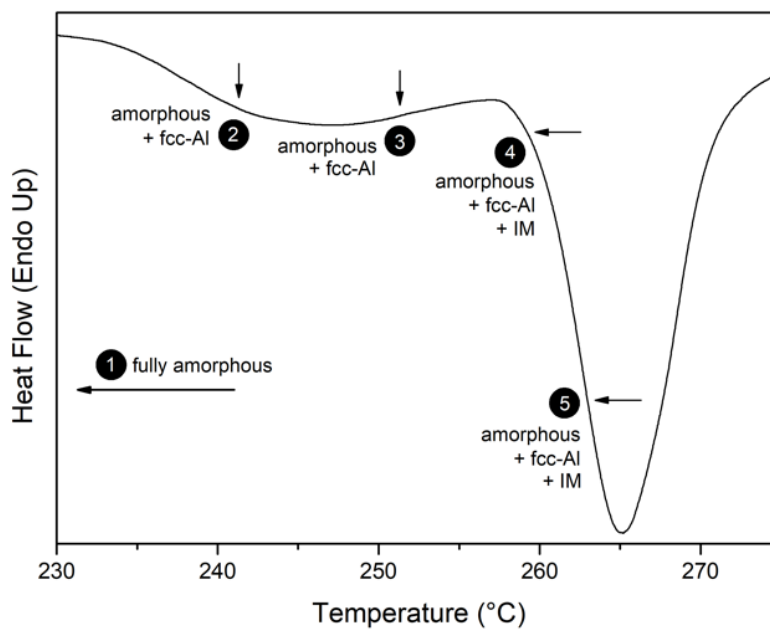
Figure 4.1 Continuous DSC trace of melt-spun ribbon $Al_{90}Tb_{10}$ shows the heat-treatment temperatures in detail

66

Table 4.1 A summary of the DSC experiments and the resulting structure of the samples

No.	Heat-Treatment	Structure
1	Room temperature – No heat treatment	Fully amorphous
2	Heated up to the beginning of the fcc-Al crystallization event + IQ	Amorphous + fcc-Al
3	Heated up to the middle of the fcc-Al crystallization event + IQ	Amorphous + fcc-Al
4	Heated up to the end of the fcc-Al crystallization event and the beginning of the intermetallic (IM) formation event + IQ	Amorphous + fcc-Al + IM
5	Heated up to the deeper regions of the IM formation event + IQ	Amorphous + fcc-Al + IM

IQ: interrupted quenching

The cooling rate slightly differs between the air and wheel sides of the rapidly solidified ribbons produced by the melt-spinner [26]. In this study, the air side of the heat-treated ribbons was preferred to perform the nanoindentation measurements and have the micropillars to maintain consistency in the cooling rates and eliminate the effects of different initial amorphous configurations on the mechanical properties and characterization results.

4.3.1   Micropillar Compressions

The following figure shows representative hardness-displacement curves for each sample (Figure 4.2(a)). The inset of the figure shows individual measurements and the calculated average for specimen 1 with no annealing. The inset demonstrates the excellent repeatability of the measurements. The main figure shows that the hardness increases with the annealing temperature. For each case, hardness decreases with increasing penetration depth. The depth sensitivity tends to diminish with increasing depth.

This figure also summarizes the hardness and elastic modulus data as a function of annealing temperature (Figure 4.2(b)). The hardness and elastic modulus, in general, increase with increasing annealing temperature. The as-prepared sample has a

hardness and elastic modulus of 3.0 GPa and 68 GPa, respectively, which rise to 4.6 GPa and 92 GPa for the 263 °C-annealed sample. Previous Vickers indentations on fully amorphous $Al_{90}Tb_{10}$ melt-spun ribbons resulted in a hardness of 2.2 GPa [74]. These 50 g-loading measurements corresponding to an indentation depth of about 3μm agree with the 2.3 GPa hardness we obtained at an indentation depth of 2 μm.

Higher hardness at smaller depths suggests an indentation size effect [74]. The indentation size effect is a well-known phenomenon in crystalline materials, usually explained by models based on geometrically necessary dislocations [75]. However, data on amorphous materials is more limited. Jang et al. [76] reported an indentation size effect in a Zr-based metallic glass explained by the increasing number of shear transformation zones with increasing indentation depth which facilitates the accommodation of plasticity at lower stresses. A quantitative model explaining this behavior in the case of amorphous metals has yet to exist.

The elastic modulus of amorphous metals tends to be lower than their crystalline counterparts due to the disordered atomic configurations and free volume leading to additional compliance at the atomic scale [57,77]. In our case, increasing annealing temperatures and the resulting crystallization cause an increase in the elastic modulus of the alloy. For annealing temperatures beyond 263 °C, the microstructure primarily consists of crystalline phases, and the elastic modulus values around 92 GPa are in close agreement with that of fully crystalline Al [78].
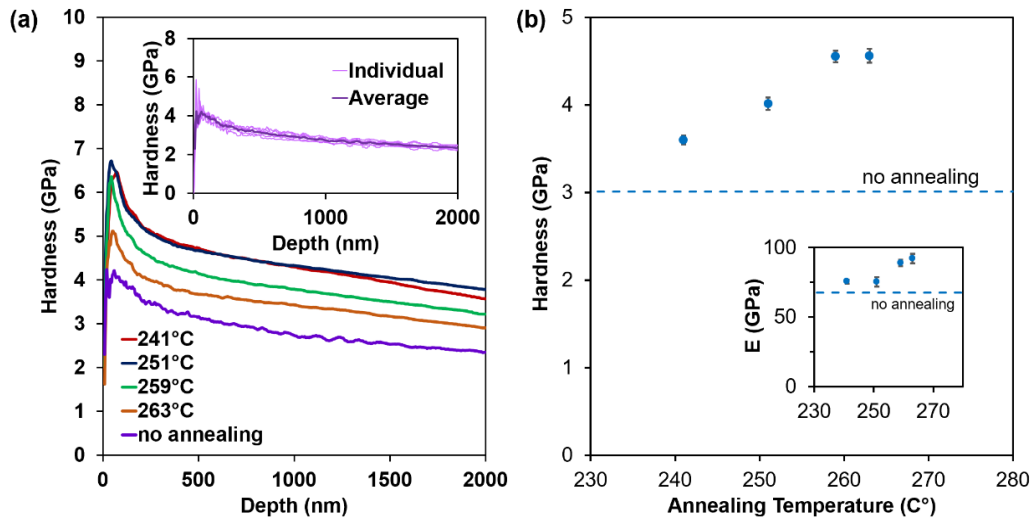
Figure 4.2 Load versus displacement data for the as-prepared sample (a), and the variation of hardness and elastic modulus with annealing temperature (b)

Figure 4.3 shows the stress-strain data of micropillar compression tests (Figure 4.3). All measurements exhibit linear elastic responses followed by strain bursts. The stress levels corresponding to the first strain burst increase with increasing annealing temperature, in agreement with the hardness results. The frequency and length of the strain burst also change with the annealing temperature. While the exact number of strain bursts and their magnitude varies from pillar to pillar, the general trend is an increasing number of smaller strain bursts with increasing annealing temperature. Any subsequent strain bursts required a higher stress level for further plasticity, resembling a strain hardening behavior.

The average yield point for the fully amorphous sample is about 0.8 GPa, which rises to 1.2 GPa for the 251 °C sample. Using a Tabor factor of 3 [79], these correspond to about 2.4 and 3.6 GPa hardness, respectively, which agrees with the nanoindentation results and previous literature findings [80,81].

The nature of the last strain burst before unloading provides insight into the mechanical response of the samples. All measurements employed displacement control with a strain rate of about 5×10^{-4} and a target peak displacement

69

corresponding to a strain of 12%. However, the data shows that the indenter went far beyond this specified limit for the case of the fully amorphous sample. This overshooting behavior diminishes considerably for the 241 °C samples and virtually disappears for 251 °C and higher annealing temperatures.

Interpretation of the results requires understanding the indentation system's dynamic behavior. A nanoindenter with electrostatic actuation is inherently load-controlled, and a pseudo-displacement control is made possible by a closed-loop system, using displacement measurement as feedback. The shear banding takes place within a few ms [82], a duration comparable to the frequency of the closed-loop system of conventional nanoindenters under standard operating conditions. As the shear banding results in an instantaneous softening within this period, a displacement burst occurs under virtually constant load, which is observed for the as-prepared samples.
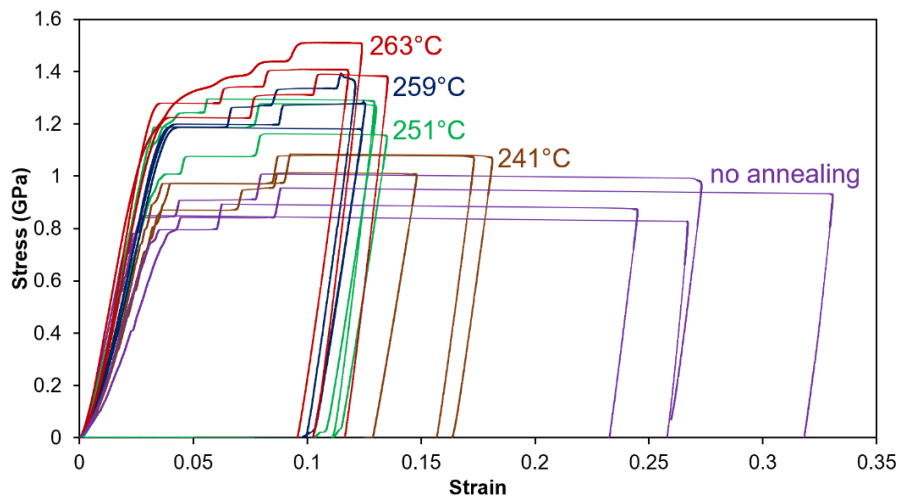
Figure 4.3 Stress vs. strain data of micropillars

The microstructural changes upon annealing reduce these unstable strain bursts. The crystalline phase of the 241 °C sample forms a network of obstacles to shear banding. When a shear band comes across a crystalline phase, it should either change its course by remaining in the amorphous matrix or go through the crystalline region

70

and induce a geometrically compatible dislocation activity or similar defects within the crystal phase to accommodate the severe shear. The additional energy required in both scenarios causes a rise in the load required for further deformation, stabilizing the closed-loop control of the nanoindenter. This effect is further pronounced for the higher heat-treatment temperature samples, where the nucleation and growth of intermetallics into the amorphous matrix start. Now the hardening behavior over the shear banding process is high enough that the nanoindenter can achieve its displacement target. A further increase in the annealing temperature to 259 °C does not appreciably increase strength, as the microstructure eventually reaches a saturated crystallinity level. As the annealing temperature increases, the number of strain bursts for a given displacement also rises, which correlates with the density of obstacles to shear banding by either the fcc-Al crystalline or intermetallic phases.

Figure 4.4 shows representative SEM images of the micropillars before and after testing, providing further insight into the deformation mechanism (Figure 4.4). The as-prepared sample exhibits a single major shear band that accommodates most of the plastic deformation. As the annealing temperature increases, the number of shear bands increases, and the amount of displacement realized by each shear band decreases. Eventually, at 263 °C, the deformation is mediated by a combination of homogeneous plasticity and shear banding, evidenced by the bulging behavior.
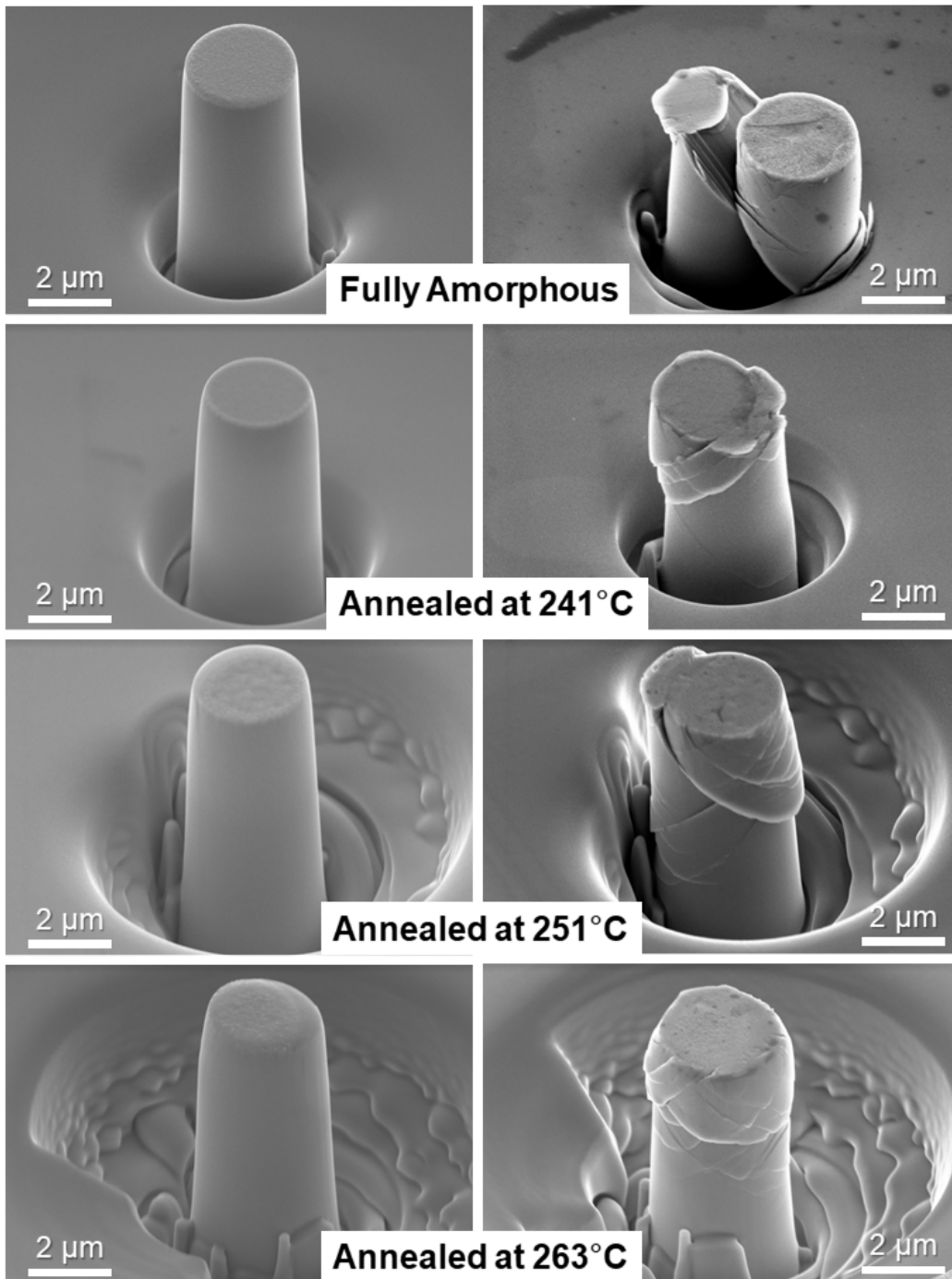
Figure 4.4 SEM images of the fabricated micropillars before and after compression
tests

4.3.2　Preparing the TEM Specimens

TEM allowed further analysis of shear bands on selected samples, namely, an as-prepared sample with a fully amorphous structure and the sample annealed at 251 °C with fcc-Al nanocrystals in an amorphous matrix. Deformed micropillars were prepared using FIB for the TEM analyses. The micropillars were highly deposited with platinum to protect the features in the deformed regions. After that, the cross-sections of the deformed pillars were thinned using Ga ions. In the end, the lift-out specimen was further thinned to its final thickness.

4.3.3　Observing the Shear Bands

The TEM figure below shows the vicinity of the shear bands in a fully amorphous specimen (Figure 4.5). The arrows indicate the shear band formation within the amorphous matrix, as represented in the bright-field image in Figure 4.5(a).

Figure 4.5(b) shows an HRTEM view of the marked region in (a), demonstrating a well-preserved shear band. The Fourier Transform pattern within the shear band region indicates nanocrystals of fcc-Al with sizes below 10 nm. These nanocrystals are much smaller than the fcc-Al nanocrystals developed during the continuous heating devitrification of metallic glasses [26], suggesting a crystallization phenomenon within the shear bands [70,72]. Several proposed mechanisms exist to induce such behavior: Yan et al. explained the crystallization by the difference between mechanical and thermal stability [71], whereas Wang et al. suggested a theory on local strains and excess free volume production during deformation [83]. Chang et al. attributed the behavior to adiabatic heating in the shear zone[70]. In contrast, Wright et al. suggested that the heat generation in these regions is insufficient to induce crystallization, as the corresponding temperature rise remains well below the glass transition temperature for most metallic glasses [68].
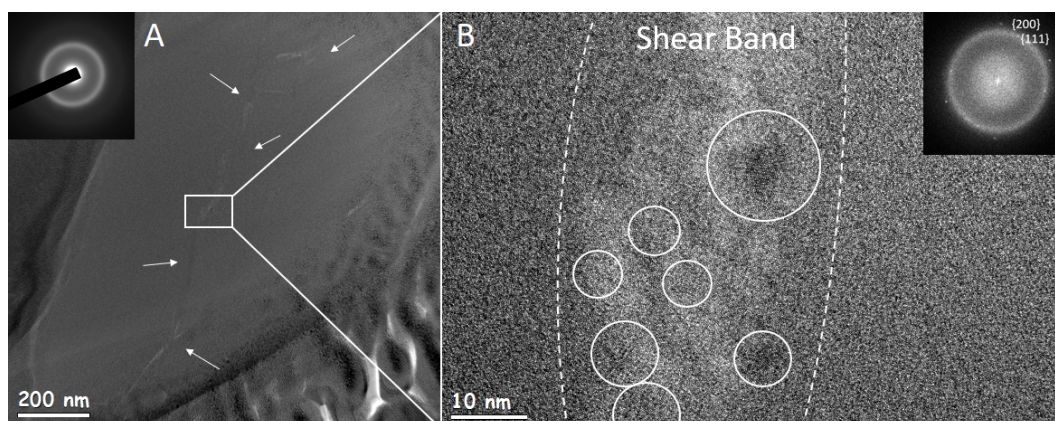
Figure 4.5 BF-TEM image shows a shear band in the fully amorphous deformed micropillar (a). The inset SAEDP of (a) validates the fully amorphous structure. HRTEM image shows the marked frame on the left (b). The inset in the HRTEM shows the FFT signal of the shear band region (b)

Our previous High-Energy X-Ray Diffraction (HEXRD) and atom probe tomography (APT) studies [20,25,29] proved that medium-range order (MRO) structures might exist in the amorphous state of certain marginal glass-forming alloys, including Al-Tb. These clusters cause a local atomic size effect, resulting in the as-quenched structure being divided into nano-scale regions by a network of MRO clusters. Upon heating the amorphous melt-spun ribbons, these MRO clusters act as the precursors of fcc-Al nanocrystals. We propose that the nanocrystalline fcc-Al may form within the shear band due to a temperature rise above the critical value for the crystallization of the MRO structure. Previous experimental and computational studies have shown that the temperature can be increased above glass transition temperatures because of the adiabatic nature of the shear band propagation [73,84]. Kawashima et al. emphasize the presence of MRO clusters while explaining the nanocrystallization near shear bands [85]. Also, Liu et al. mentioned the importance of atomic arrangement, free volume coalescence, and atomic transport mechanisms in shear regions to explain the localized shear band formation and inhomogeneous plastic deformation on metallic glasses [86]. They reported several deformation outcomes, such as nanocrystallization, straight shear band formation,

and branched shear band formation accompanied by nanocrystallization. Their discussion draws attention to the need for more conclusive studies on the atomic and microstructural features to adequately explain the micromechanical phenomena. However, the studies mentioned above observed similar crystallization events for similar structures. The formation and morphology of these crystals also match the properties of the crystals formed during deformation in this study. These crystals have a spherical shape with a diameter of 5 to 10 nanometers. Likewise, the morphological features of the shear band regions are comparable with the shear band formation accompanied by nanocrystallization. At this point, the literature suggests that the nanocrystal formation in Al-based metallic glasses only occurs in the compressive regions. In contrast, the tensile regions have a higher density of nanovoids [73].

The MRO clustering in the metallic glass changes the local viscosity. Therefore, during the deformation, the viscous flow properties will vary significantly. Such regional viscosity variations play a crucial role in the shear deformation of amorphous metals as atomic diffusion decreases the free volume. At the same time, shearing action promotes an increase in the free volume [72]. This competition between flow dilation and flow contraction due to local viscosity changes is proposed to generate ordering and disordering, respectively [72]. This agrees with the observations of brighter contrast in shear band zones, indicating a higher amount of free volume [72], suggesting a lower viscosity than the surroundings. According to Yan et al., the higher amount of free volume, i.e., higher energy in these regions, increases the driving force for the transformation [71]. As a result of the competing mechanisms mentioned above, some regions will be locally compressed and act as a preferential crystallization site for the Al-rich network clusters. The relation between the nucleation at the Al-rich network and viscosity is also correlated with the literature. Studies on the mechanically induced nanocrystallization of Al-based metallic glasses emphasize the change of crystallization behavior with composition [69,71].

While the as-prepared specimen does not possess any nanocrystals other than within the shear band region, the annealed specimen at 251 °C contains highly populated fcc-Al nanocrystals throughout the amorphous matrix. The below figure shows a series of SEM and TEM images of a partially devitrified and deformed specimen (Figure 4.6). During the FIB lift-out preparation, the TEM foil was positioned around the major shear band observed in the SEM.

Bright-field images show that the fcc-Al nanocrystals shown all have dendritic morphologies. HRTEM is used to investigate the interaction of the shear band with the fcc-Al nanocrystals. Processing the HRTEM image by FFT and IFFT shows that the shear band indeed cuts the dendrite arm of this nanocrystal. The observations suggest that the shear band propagates and goes through the nanocrystal dendrite arm instead of generating multiple secondary shear bands around the nanocrystal. It should also be noted that we have not observed any defects within these fcc-Al nanocrystals. The resultant IFFT image shows the broken dendrite arm from the pre-formed fcc-Al nanocrystal, a shear band, and a newly crystallized Al region in the shear band due to the MRO network.
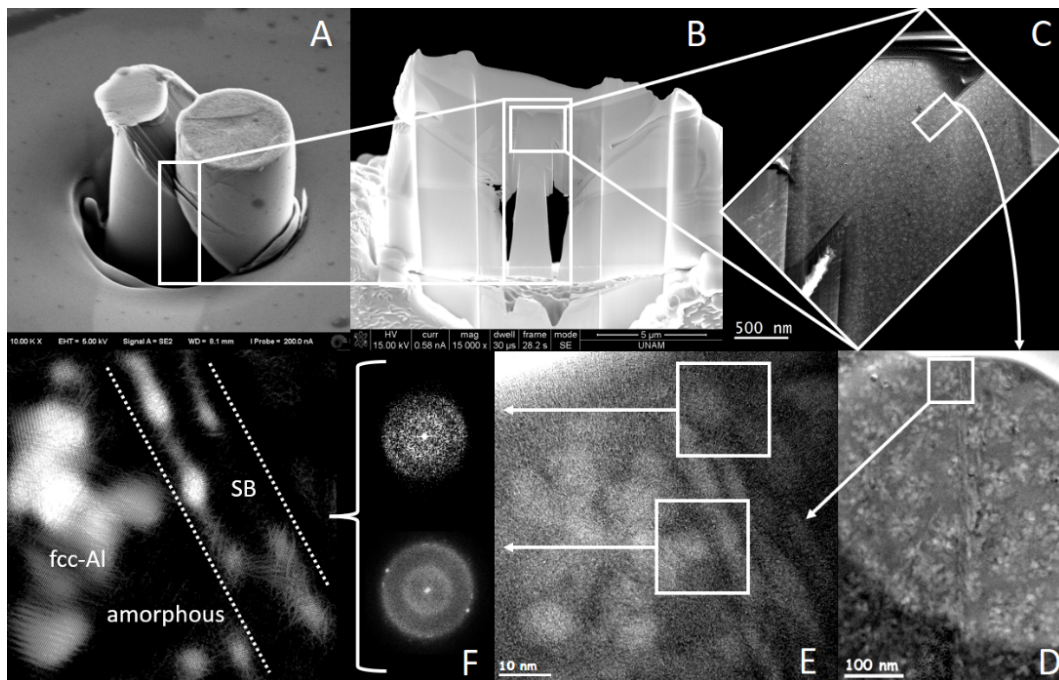
Figure 4.6 Partially devitrified deformed micropillar with fcc-Al nanocrystals and an amorphous matrix (a); FIB cross-sectioning for TEM analysis (b); BF-TEM image of the initially marked fracture surface – further thinned region shows the dendritic nanocrystals and a shear band in the marked frame (c); BF-TEM image shows the interaction of dendrite arms with the shear band (d); HRTEM of the interaction area (e); FFT and IFFT patterns of the interaction area (f)

The crystallization of the fcc-Al phase in the shear band region for this specimen is identical to the crystallization event observed in the fully amorphous specimen (Figure 4.7). The fcc-Al nanocrystals of 5 nm or smaller size should have been grown within the shear band regions.
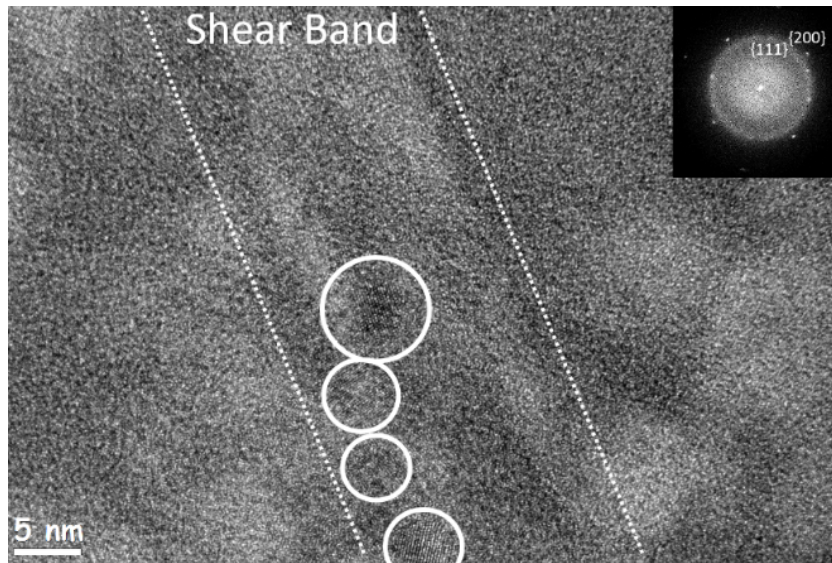
Figure 4.7 HRTEM image shows the partially crystalline specimen. The inset shows the FFT signal from the crystals in the shear band region

The cutting case for the dendrites along shear bands should alter with the size of these crystals. Fan et al. comment on the different zones of the shear bands proposed by Shao et al. [87] and emphasized that the dendrites prevent the generation of liquid-like zones surrounded by a solid-like zone [88]. This phenomenon, combined with the crystallization of the clusters from the amorphous state, suggests a competition between softening and hardening mechanisms under compression. The flow of material due to the localized deformations in the matrix and the critical dendrite arm spacing for the defect generation in the crystals are the essential parameters of this competition, in agreement with the micromechanical observations made in this work. The rare-earth solute rejection from the Al-nanocrystals into the matrix and the increasing crystalline amount with annealing temperature are believed to be the root causes of both strength and ductility enhancement for these devitrified metallic glasses, respectively, which also agrees with the micromechanical results.

4.3.3.1   Crystallization Near Shear Bands

In this study, we explored the links between the microstructure and the mechanical behavior in metallic glass – crystalline composites by investigating a range of microstructures in the AlTb system. Nanoindentation, micropillar testing, and high-resolution TEM data have been analyzed to explain the deformation mechanisms in a marginal metallic glass system. During deformation, locally lower viscosity regions create excess free volume, promoting the formation and propagation of shear bands. The higher viscosity regions under localized compression serve as nucleation sites for the Al-rich network clusters. The summary of this work regarding the crystallization phenomena during deformation can be seen in the below figures (Figure 4.8) (Figure 4.9).
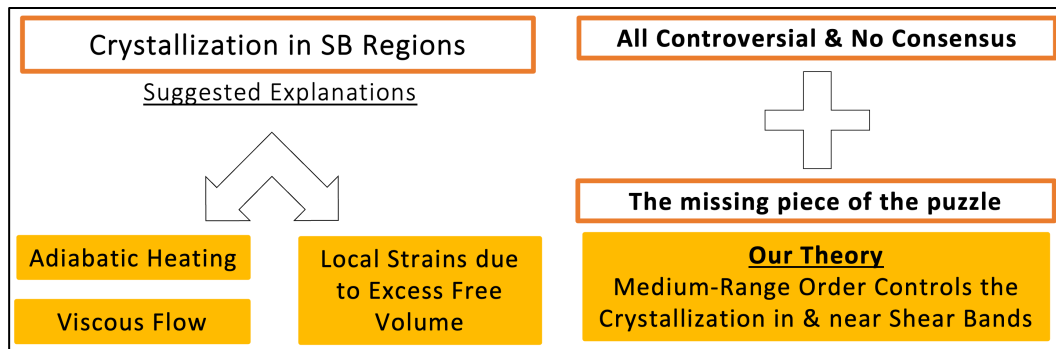
Figure 4.8 Explanation of the crystallization phenomena in the shear band (SB) regions
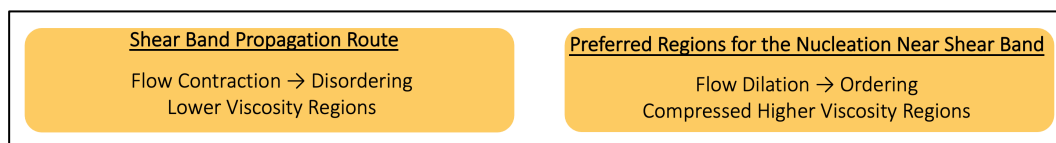
Figure 4.9 Important factors for shearing and nucleation

4.3.3.2   Crystalline-Shear Band Interactions in Amorphous Matrix

The nucleation and growth of the fcc-Al nanocrystals controlled by diffusion and the existence of medium-range order explain the portion of the property enhancement. In contrast, the size-dependent crystal morphology governs the energetically favorable interaction between the shear band and the crystal. Our observations indicate that the shear bands propagate through the matrix by directly shearing smaller dendrite arm nanocrystals. At the same time, the bigger armed crystals should accommodate plasticity by the crystal defect generation. During the crystallization of fcc-Al, the crystals have lower dendrite arm spacings in the nucleation dominant regime, and they have higher dendrite arm spacings in the growth dominant regime. Therefore, there should be some plasticity in the case of a grown fcc-Al crystal as a result of the crystalline defect generation. But for each case, the shear band cuts the crystals one way or another.

Ultimately, the findings reveal the interactions between crystalline and amorphous domains under deformation and provide clues for designing novel nanostructured alloys that combine high strength and damage tolerance.

CHAPTER 5

COMPREHENSIVE EVALUATION OF THE INFLUENCE OF UNDERCOOLING AND THE MEDIUM-RANGE ORDER

The function of this chapter is to evaluate and criticize the recent findings on the Al-based marginal metallic glass former systems and the current literature. Our recent understanding of the structural and chemical tendencies of MMGs and their corresponding properties is based on the cause-and-effect relationship. Although not all the causes have been clarified so far, we have obtained a base knowledge of the thermodynamics and kinetics of glassy metal evaluation. Several well-standing hypotheses exist, even for extreme cases like marginal metallic glass former systems. These include the ones which consider their first formation and devitrification.

Why and how a glassy metal is obtained in the first place? Which structural and chemical effects play a role in metallic glass formation? How did Turnbull's experiments evolve? All of these questions have been studied by cutting-edge characterization methods and computer simulations. However, there is no single parameter that can be used to predict and evaluate the structure and property relationship of metallic glasses. Especially for the marginal glass formers, predicting the atomic ordering and the effect of this ordering on its emerging properties is quite challenging. For this reason, this chapter will focus on and cover the possible explanations for these exciting features by connecting physically measurable quantities with the existence of outlier nanoscale mechanisms.

No matter how the evaluation should start with the birth of a glassy metal. As explained in previous chapters, the precursor of an amorphous metal can be a solid, liquid, or even a plasma state. Although the final products seem alike, they are not even the same. The only thing that is the same for these products is that they all have

an amorphous structure. However, the configuration of the amorphous phase is spectacularly different for each case. Some of these differences were discussed in detail in the previous chapters.

5.1   Medium-Range Order

Now, the question becomes, how the amorphous phase can differ? Indeed, it is all related to its order. Although it is stated that the amorphous phase is the phase in which there is no periodicity, there might be some types of correlations in the structure that exhibit an order. The amorphous phase indeed lacks the long-range order. However, one can define a type of short to medium-range order for these systems. There are variables like the Warren-Cowley parameter, bond angle distribution, Honeycutt-Andersen pairing, or bond order parameter to identify these short to medium-range order correlations. Resolving the pair or pair-pair correlations in atomic scale reveals these types of orders. Therefore, these atomic pairings that lack long-range order correlations exist in the amorphous phase. Hence, one can conclude that the amorphous phase is not random at all.

For the Al-based MMGs, it is known that the liquid precursor yields a higher amount of MRO in the system. What might be the reason for this? Do these medium-range ordered clusters also exist in the parental liquid state? For different Al-RE MMGs, our group discussed and studied the influence of all precursor states. The influence of plasma precursor on the $Al_{90}Y_{10}$ system was discussed in Chapter 2. The influence of solid precursor was also studied. We achieved 140 hours long high energy ball milling from an arc-melted $Al_{90}Sm_{10}$ solid crystalline specimen. In the end, an amorphous $Al_{90}Sm_{10}$ was obtained with a small amount of nanocrystalline phase in the batch (Figure 5.1). Although the melt-spun $Al_{90}Sm_{10}$ MMG has a characteristic pre-peak, which is previously attributed to the MRO and the RE-RE correlations in the system, the solid-precursor $Al_{90}Sm_{10}$ MMG had no distinct pre-peak in the XRD data. Hence, the structure seems more random than the melt-spun $Al_{90}Sm_{10}$ MMG.
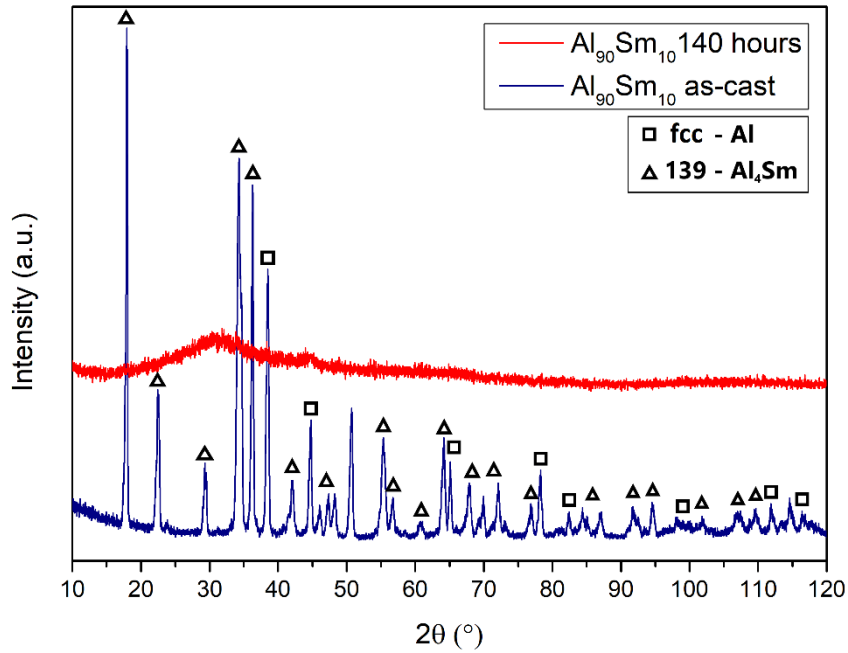
Figure 5.1 Comparison of the XRD data for arc-melted and ball-milled $Al_{90}Sm_{10}$

For the $Al_{90}Sm_{10}$ system, our group previously conducted an in-situ heating synchrotron high-energy X-ray diffraction experiment in transmission mode at Argonne National Laboratory, Advanced Photon Source. For the liquid structure analysis, specimens were sealed into carbon-lined quartz capillaries under an Ar atmosphere to prevent interactions and oxidations. The X-ray with a wavelength of 0.012450 nm was used for the experiments. The data was collected using a MAR charge-coupled device in Debye Scherrer geometry. The diffraction data of the empty carbon-lined quartz capillary was also collected and subtracted from the original data to eliminate its contribution. This unpublished study in our group indicates the formation of a hexagonal intermetallic first, followed by the formation of another tetragonal intermetallic during the liquefaction of as-cast $Al_{90}Sm_{10}$ specimen with a microstructure of fcc-Al & tetragonal IM (Figure 5.2). The formation of the t-Al_4Sm phase just before the complete liquefaction is particularly important since similar tetragonal Al-RE intermetallics with similar compositions

are also forming during the devitrification/liquefaction of other Al-RE systems inside the glass formation range. The RE-RE distance in these intermetallics was previously attributed to the characteristic pre-peak and the MRO in these systems. This argument was detailed in Chapter 2. Since the RE-centered Voronoi cells with high RE-RE correlations and 16 Al atoms in their nearest neighboring shell are the clusters that cause the formation of the pre-peak, it can be argued that the MRO persists at elevated temperatures where the liquid phase is forming for the Al-Sm system. The tetragonal IM phase transformation before complete liquefaction may also hint at the same type of correlation in the liquid state.
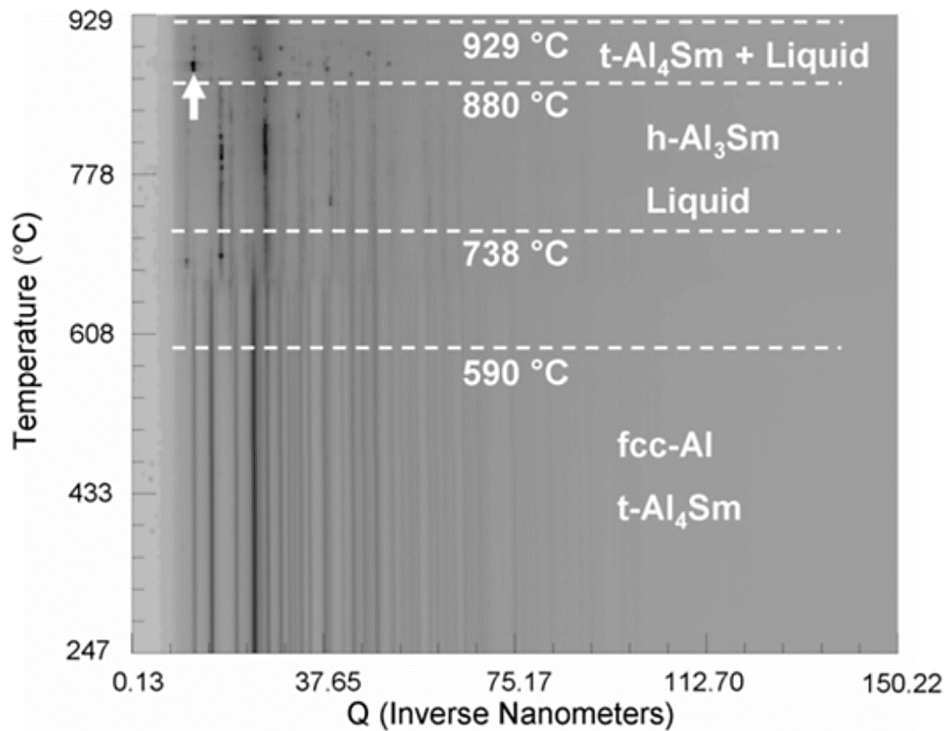

Figure 5.2 In-situ heating HEXRD experiment of as-cast $Al_{90}Sm_{10}$. Unpublished work by Prof. Dr. Y. E. Kalay

Later, several HEXRD experiments and MD simulations were run to reveal and prove the existence of a medium-range ordered network in the liquid state. A

previously conducted and unpublished HEXRD experiment up to 1393 K exhibits a dominant pre-peak and a slight side-peak in the liquid state (Figure 5.3.a). This finding is strong evidence of the presence of short to medium-range ordered clusters in the liquid. Note that the experimentation and data collection in the liquid state at these temperatures are also incredibly hard without any oxidation, and this experiment itself is a standalone progress in this field. Later, this HEXRD experimentation was validated with an MD-simulated model (Figure 5.3.b) by Sariturk and Kalay [32]. The MD-simulated model gives an insight into the local structure of the liquid, even at higher temperatures up to 2100 K. The MD-simulated data also revealed that the short to medium-range correlations persist in the liquid.
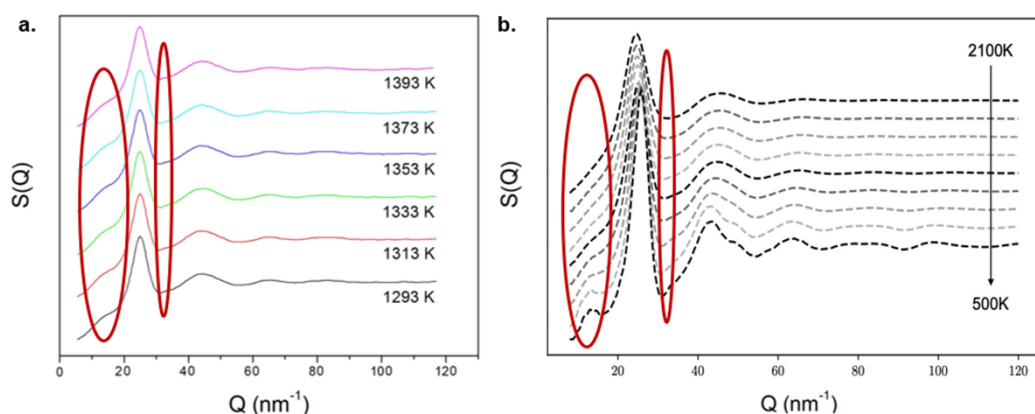
Figure 5.3 Experimental (a) and MD-simulated (b) S(Q)-Q data for liquid $Al_{90}Sm_{10}$. The red regions represent the positions of pre-peak and side-peak. The data at (b) was adopted from [32]

Yildirim et al. also conducted similar in-situ HEXRD experimentation on the $Al_{90}Tb_{10}$ system in 2016 [29]. This time, not the liquid state but the devitrification sequence of Al-Tb MMG was investigated using different precursors. The initial room temperature structures of the magnetron-sputtered and the melt-spun $Al_{90}Tb_{10}$ were found identical (Figure 5.4). However, the devitrification behaviors were utterly different (Figure 5.5). For the magnetron sputtered $Al_{90}Tb_{10}$ thin film with

parental vapor phase, the devitrification sequence was "amorphous state → fcc-Al → cubic IM phase". On the other hand, the devitrification sequence for the melt-spun $Al_{90}Tb_{10}$ ribbon with a parental liquid state has an additional hexagonal IM transformation, and the decomposition path was "amorphous state → fcc-Al → hexagonal IM → cubic IM phase". This difference and the additional hexagonal phase decomposition were attributed to the possible topological and chemical MRO in the parental liquid state.
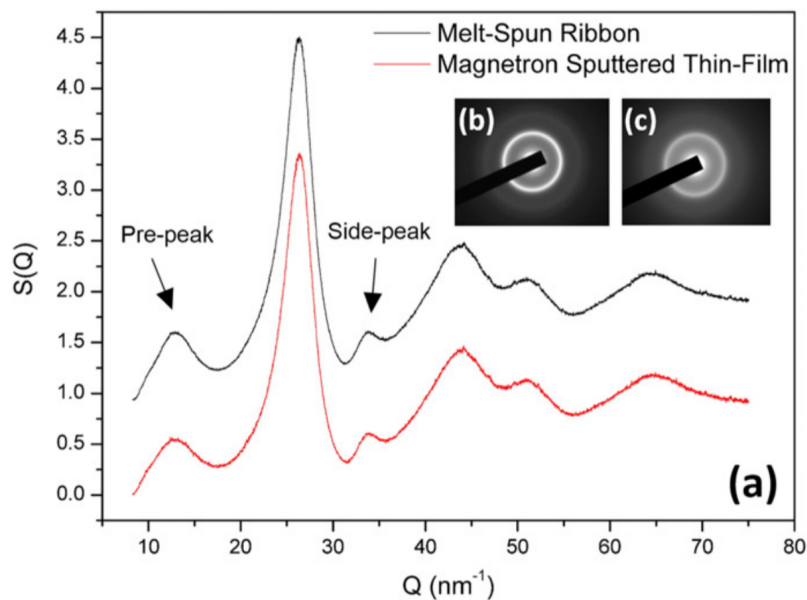
Figure 5.4 Initial S(Q)-Q data of melt-spun and magnetron-sputtered $Al_{90}Tb_{10}$ (a), SAED data of melt-spun $Al_{90}Tb_{10}$ (b), and SAED data of magnetron-sputtered $Al_{90}Tb_{10}$. Adopted from [29]
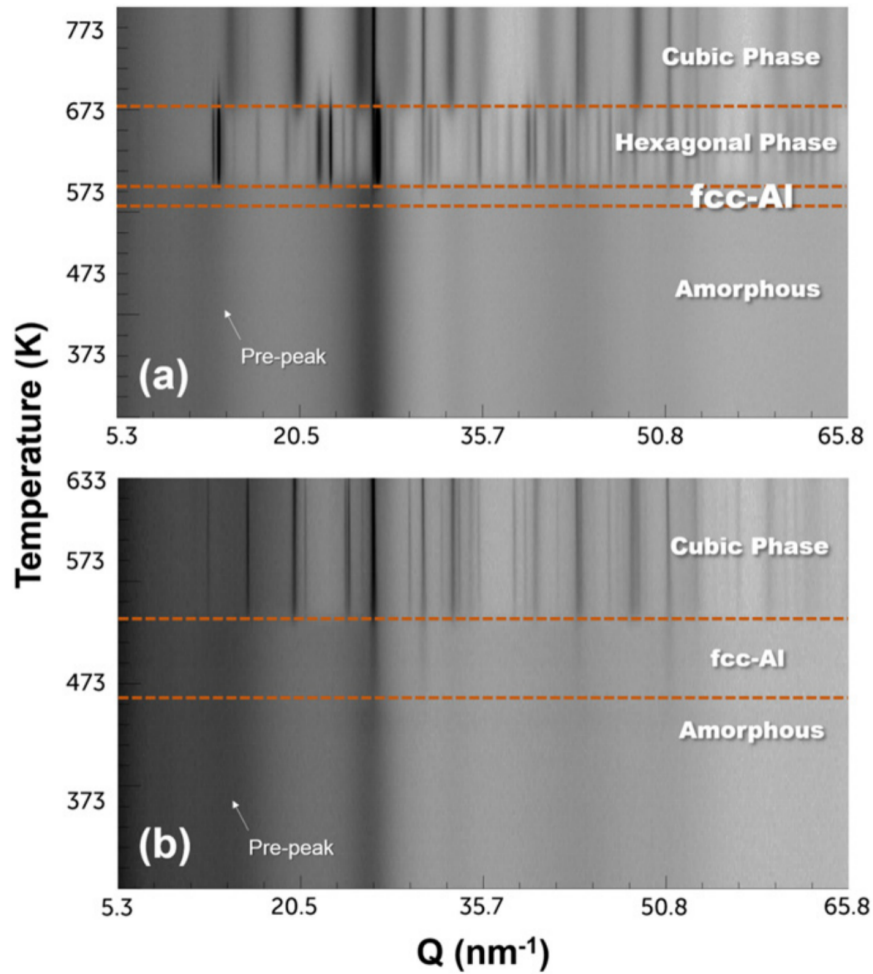
Figure 5.5 In-situ heating HEXRD patterns of melt-spun (a) and magnetron-sputtered (b) $Al_{90}Tb_{10}$. Adopted from [29]

5.2   Undercooling

The difference between the magnetron-sputtered and the melt-spun specimens above was not only their parental states. The cooling rates and the undercooling levels were also different. The cooling rate was around 10^6 K/sec for the melt-spun specimen, while it was around 10^9 K/sec for the magnetron-sputtered specimen. Since the melt and the vapor phase exist at different temperatures for the same pressure condition,

their undercooling levels were also varied. Therefore, one should also discuss the effect of undercooling on the glassy metal formation.

It is known that the undercooling must be high enough to form an amorphous phase in metals. Especially for the MMGs with off-eutectic GFR, it must be even higher. However, as seen in the above devitrification path study, increasing the undercooling upon a certain level may negatively affect the order, as well. This assumption may be valid if the MRO is formed during freezing. However, this may not be the case for the MMGs. As we discussed several times, the parental liquid state itself may have medium-range ordered clusters. Therefore, it would be beneficial to freeze the structure fast if one desires to observe this MRO in the amorphous state. Hence, it can be concluded that the increased undercooling levels may also increase short to medium-range correlations in the solid state if the parental state contains these types of correlations. Then, for the case mentioned above, the effect of parental state was more dominant than the effect of undercooling since our hypothesis is based on the liquid state presence of MRO.

The influence of undercooling should be discussed with its types. While thermal undercooling refers to the temperature difference between the melting point of a material and the temperature at which it can be cooled to form a glass, kinetic undercooling is related to the cooling rate of this event. Therefore, one should expect higher glass-forming ability with higher thermal and kinetic undercooling. However, this is not the case since a previous study by Kalay et al. achieved an amorphous phase formation for the gas-atomized marginal glass former Al-Sm specimens [21]. In the gas atomization procedure, the cooling rate can be as low as 10^2 K/sec, and it is normally not enough to obtain a marginal metallic glass. The successful formation of glassy Al-Sm with gas atomization should be directly related to thermal undercooling. Hence, although the role of kinetic undercooling is unarguably important, the main factor that determines the metallic glass formation is thermal undercooling with the contribution of constitutional undercooling.

In the end, increasing thermal undercooling during solidification will yield higher MRO correlations in the system, which is eventually the reason for the emerging properties, tendencies, and anomalous nucleation behaviors of MMGs.

5.3   Influence on Viscosity

The influence of undercooling and atomic ordering should be connected and somehow expressed with physically measurable quantities. The candidate quantities can be any material-specific property like magnetic permeability, density, viscosity, or optical refraction. There might be a type of correlation and a ruled pattern between these quantities and the order. However, the concept of viscosity can be further considered to make this connection since it is a well-studied concept for glass formation. An increased undercooling yields a tremendous viscosity increment during solidification from the liquid. Hence the viscosity increment beats the diffusion at some point, and the structure of a liquid will immediately freeze. Therefore, this viscosity increment is a critical factor for metallic glass formation. However, what if the viscosity of the liquid was also a determining factor for the undercooling, MRO, and eventually for the emerging properties? What if the MRO itself affects the viscosity of the liquid? An analytical approach was used to correlate and connect each factor.

First, a nucleation rate (I) was expressed, assuming the usual solidification.

$$I = A * \exp\left(-\frac{\Delta G}{RT}\right)$$

where ΔG is the change of Gibbs free energy for nucleation, R is the gas constant, T is the temperature, and A is the pre-exponential factor. The change in the Gibbs free energy can be expressed as

$$\Delta G = \Delta G_V + \Delta G_S$$

where ΔG_V and ΔG_S represent volume and surface free energy change, respectively. These terms can be further explained as

$$\Delta G_V = \frac{\Delta H_V * \Delta T}{T_m}$$

and

$$\Delta G_S = \gamma * A_S$$

where ΔH_V is the latent heat of fusion, T_m is the melting temperature, ΔT is the undercooling, γ is the interfacial energy, and A_S is the surface area of the critical cluster. This term can be related to the critical cluster size, S_C, that can be solidified/frozen into an amorphous phase.

Now, these terms can be connected using the Becker-Döring cluster equations, which provide a simple kinetic model considering the dynamics of coagulation, fragmentation of clusters, and the dynamic of phase transitions, like metastability, nucleation, and coarsening [89,90]. The Becker-Döring cluster equations can be modified to consider this amorphous phase transformation. In that case, the nucleation rate can be expressed with the effect of viscosity, η, on the material.

$$I = K * \eta * \frac{S_C^3}{\delta^2} * \exp\left(-\frac{2\gamma}{RT}\right)$$

where δ is the thickness of the diffusion layer, and K is the proportionality constant. Combining these equations will yield an analytical expression of the connection between undercooling, cluster size, and viscosity based on the classical nucleation theory and the Becker-Döring cluster equations.

$$\Delta T = K * \frac{T_m}{\Delta H_V} * \eta * \frac{S_C^3}{\delta^2} * \exp\left(-\frac{2\gamma}{RT}\right)$$

This relationship was visualized using NumPy and Matplotlib libraries via Python. All the materials constants were used for pure Al to see and discuss the general perspective of the Al-based MMGs. Since this is an analytical approach, the proportionality constant, K, was adjusted randomly to yield graphically meaningful data. In the end, the following visualizations were achieved (Figure 5.6) (Figure 5.7).
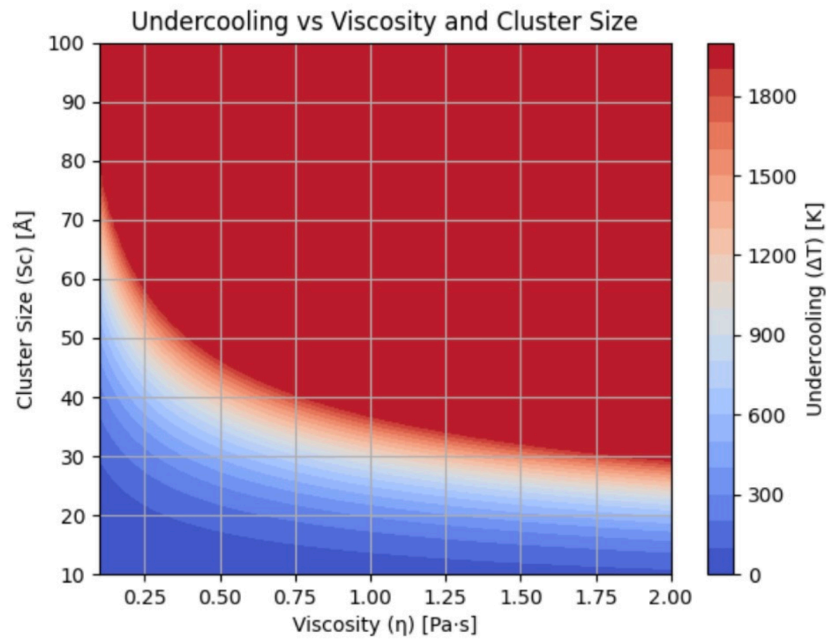
Figure 5.6 Analytical prediction of the relationship between cluster size, viscosity, and undercooling for Al-based MMGs
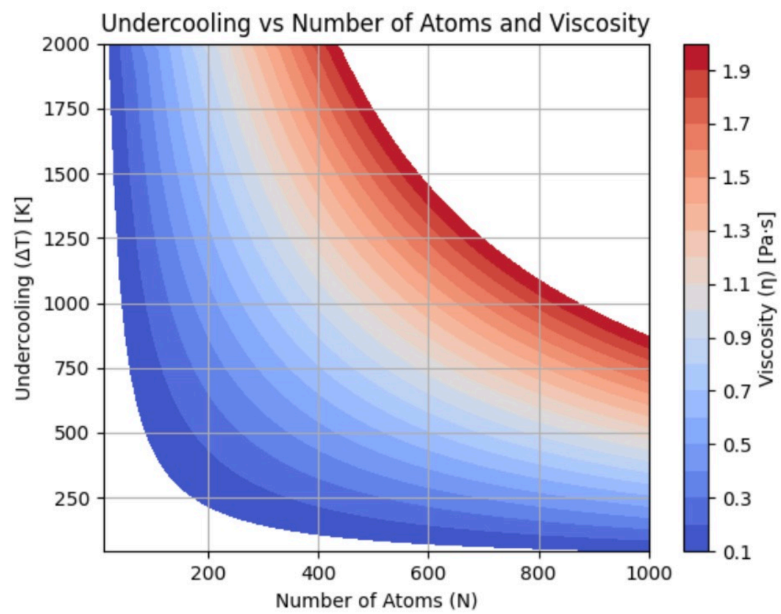
Figure 5.7 Analytical prediction of the relationship between the number of atoms in the clusters, viscosity, and undercooling for Al-based MMGs

One should conduct reliable experimentation to find these materials constant for each composition and determine a suitable proportionality constant to let the graph gain its meaning.

In the graphs, it is clearly seen that the increasing undercooling or viscosity yields the allowance of larger amorphous clusters. The number of atoms in these pockets will also increase with increasing undercooling. As can be seen, this undercooling amount that determines the clustering behavior is directly related to the viscosity. Also, remember that the MRO correlations diminish and disappear at considerably higher temperatures, even if they persist in the liquid state. After that specific temperature, the connectivity between these ordered pockets in the liquid will become extinct, and the correlations of the atoms will persist only in an SRO manner.

Finally, these interpretations can be used to estimate the atomic ordering, the necessary undercooling, and the emerging properties of a given MMG just by measuring its viscosity.

CHAPTER 6

CONCLUSION AND FUTURE RECOMMENDATIONS

6.1   Conclusion

Investigation of the clustering and ordering in atomic scale is a crucial subject not only for solid-state physics but also for other disciplines. Simply because the stars, planets, and galaxies are nucleating. Even the universe was nucleated at some point. The human being was and still is nucleating physically, biologically, culturally, and in evolutional manners. Therefore, the subject has its own profound scientific and philosophical importance.

Nevertheless, this thesis study has been focused on this crucial subject from a materials science and engineering background. For this reason, Al-based marginal metallic glass former systems were chosen as a role model. The pathways of symmetry and stability were followed from the undercooling of a parental material to the decomposition of an amorphous one. With this respect, the structure of marginal metallic glasses was deeply analyzed with in-situ advanced characterization tools. It was found that the amorphous phase was not random at all. In the atomic scale, there are clusters that exhibit short to medium-range correlations and form a network that divides the parental liquid phase into pockets with specific compositions. In this point, the influence of atomic ordering on the emerging properties of these materials and their devitrification products were investigated and discussed in detail. For this purpose, several micromechanical, X-ray, and electron scattering characterization methods were used on the selected Al-based MMG

former system. The evolution was based on the interaction of the shear bands and the nucleated nanocrystals or the pre-nuclei medium-range ordered clusters. It was found that enhanced mechanical properties can be achieved by controlling the MRO and devitrification from the MMG.

Later, the influence of undercooling on the atomic ordering and decomposition paths was investigated. The influence of parental states on the MMG formation and local structures was discussed, considering the thermal and kinetic undercooling. In the end, an analytical solution to relate these phenomena to physically measurable quantities was proposed. The potential physical quantity that might be affected by these atomic orderings and undercooling was decided as viscosity. It was argued that controlling and measuring the viscosity may enable us to predict and control the order, undercooling, and the resultant properties of the material.

6.2   Future Recommendations

Further investigations on the influence of undercooling and short to medium-range ordering on the marginal metallic glasses should include several cutting-edge experimentations. As discussed in previous chapters, there are some unknown crystalline phases during the decomposition of metallic glass, especially for Al-based marginal metallic glass systems. The reason behind the formation of such intermediate products is the metastability of the system. Increasing thermal and kinetic undercooling increases the overall instability of the system since they prevent the material from forming its equilibrium phases. Therefore, the devitrification of metallic glass often includes the decomposition of the amorphous phase into several intermediate phases before the complete equilibrium state is achieved. Identification and detection of these phases should contribute to our current understanding of atomic ordering, the effect of undercooling, and nucleation. These will eventually yield an increased knowledge of thermodynamics, kinetics, and the solid-state physics of phase transformation. To detect and identify these phases and their pre-nuclei clusters in the amorphous state, one should focus on high-resolution scanning

transmission electron microscopy (HRSTEM) methods. There are highly capable electron microscopy facilities in the world, such as the Ernst-Ruska Centre for Microscopy and Spectroscopy with Electrons (ER-C) in Germany. Their HRSTEM and in-situ data collection capabilities are a breakthrough in the field, thanks to their cutting-edge advanced TEMs. The experimentation with such tools would be appreciable and advanced.

On the other hand, in-situ high-energy X-ray scattering experiments, including structural and chemical ones, play a vital role in this research. These experiments should continue. Since the atomic ordering came from the parental liquid state, in which the atoms were not randomly distributed at all, these in-situ HEXRD experiments should focus on the liquid state. Moreover, measuring the physical quantities during these experiments will also be necessary to prove our hypothesis and relate the order and undercooling to a physically measurable quantity. As we focused on the viscosity, the high-temperature viscosity measurements of the liquid phase would be beneficial.

However, the investigation of a liquid state, especially for the Al-RE marginal metallic glass former systems, is highly challenging, as discussed in the previous chapters. For this reason, highly controlled inert atmosphere conditions should be satisfied. There are only a few devices in the world that are capable of in-situ high-temperature liquid viscosity measurements up to 1800 K, yet it is unclear whether the controlled atmospheric conditions are enough to prevent the oxidation of the RE elements for these devices. Even the addition of a single impurity atom to the system may change the short to medium-range correlations completely. Therefore, one should consider low Earth orbit research opportunities to collect data in perfect vacuum conditions. Ultimately, these experiments will supply the data based on the true atomic structure. We have been trying in-situ levitation melting HEXRD experiments in controlled atmospheric conditions at the synchrotron facilities, yet oxidation has been inevitable so far. Hence, these liquid HEXRD and viscosity experiments can be conducted at International Space Station (ISS). In future research, one can apply for these experiments with a written proposal since ISS

excepts research proposals worldwide at no cost. Also, the effect of the space environment and microgravity on clustering, atomic ordering, nucleation, undercooling, viscosity, and phase transformation might supply exciting and crucial information to our current knowledge and the scientific literature.

REFERENCES

[1] W. Klement, R.H. Willens, P. Duwez, Non-crystalline structure in solidified Gold-Silicon alloys, Nature. 187 (1960) 869–870. https://doi.org/10.1038/187869b0.

[2] H.S. Chen, D. Turnbull, Thermal evidence of a glass transition in gold-silicon-germanium alloy, Appl Phys Lett. 10 (1967). https://doi.org/10.1063/1.1754813.

[3] H.S. Chen, D. Turnbull, Evidence of a glass-liquid transition in a gold-germanium-silicon alloy, J Chem Phys. 48 (1968). https://doi.org/10.1063/1.1669483.

[4] H.S. Chen, D. Turnbull, Formation, stability and structure of palladium-silicon based alloy glasses, Acta Metallurgica. 17 (1969). https://doi.org/10.1016/0001-6160(69)90048-0.

[5] H.S. Chen, Thermodynamic considerations on the formation and stability of metallic glasses, Acta Metallurgica. 22 (1974). https://doi.org/10.1016/0001-6160(74)90112-6.

[6] R.C. Ruhl, B.C. Giessen, M. Cohen, N.J. Grant, New microcrystalline phases in the NbNi and TaNi systems, Acta Metallurgica. 15 (1967). https://doi.org/10.1016/0001-6160(67)90060-0.

[7] H.S. Chen, C.E. Miller, Centrifugal spinning of metallic glass filaments, Mater Res Bull. 11 (1976). https://doi.org/10.1016/0025-5408(76)90213-0.

[8] H.S. Chen, C.E. Miller, A rapid quenching technique for the preparation of thin uniform films of amorphous solids, Review of Scientific Instruments. 41 (1970). https://doi.org/10.1063/1.1684774.

[9] H.H. Liebermann, C.D. Graham, Production of amorphous alloy ribbons and effects of apparatus parameters on ribbon dimensions, IEEE Trans Magn. 12 (1976). https://doi.org/10.1109/TMAG.1976.1059201.

[10] A. Peker, W.L. Johnson, A highly processable metallic glass: Zr41.2Ti 13.8Cu12.5Ni10.0Be22.5, Appl Phys Lett. 63 (1993). https://doi.org/10.1063/1.110520.

[11] F. Ren, L. Ward, T. Williams, K.J. Laws, C. Wolverton, J. Hattrick-Simpers, A. Mehta, Accelerated discovery of metallic glasses through iteration of machine learning and high-throughput experiments, Sci Adv. 4 (2018). https://doi.org/10.1126/sciadv.aaq1566.

[12] R.C. Budhani, T.C. Goel, K.L. Chopra, Melt-spinning technique for preparation of metallic glasses, Bulletin of Materials Science. 4 (1982). https://doi.org/10.1007/BF02824962.

[13] A. Inoue, Stabilization of metallic supercooled liquid and bulk amorphous alloys, Acta Mater. 48 (2000). https://doi.org/10.1016/S1359-6454(99)00300-6.

[14] A. Inoue, High Strength Bulk Amorphous Alloys with Low Critical Cooling Rates (Overview), Materials Transactions, JIM. 36 (1995). https://doi.org/10.2320/matertrans1989.36.866.

[15] M.H. Cohen, D. Turnbull, Composition requirements for glass formation in metallic and ionic systems, Nature. 189 (1961). https://doi.org/10.1038/189131b0.

[16] D. Turnbull, Under What Conditions Can A Glass Be Formed?, Contemp Phys. 10 (1969). https://doi.org/10.1080/00107516908204405.

[17] J.F. Löffler, Bulk metallic glasses, Intermetallics (Barking). 11 (2003). https://doi.org/10.1016/S0966-9795(03)00046-3.

[18] N. Metatla, A. Soldera, The Vogel-Fulcher-Tamman equation investigated by atomistic simulation with regard to the Adam-Gibbs model, Macromolecules. 40 (2007). https://doi.org/10.1021/ma071788.

[19] A. Inoue, Amorphous, nanoquasicrystalline and nanocrystalline alloys in Al-based systems, Prog Mater Sci. 43 (1998) 365–520. https://doi.org/10.1016/S0079-6425(98)00005-X.

[20] Y.E. Kalay, L.S. Chumbley, I.E. Anderson, Crystallization behavior in a highly driven marginal glass forming alloy, J Non Cryst Solids. 354 (2008) 3040–3048. https://doi.org/10.1016/j.jnoncrysol.2007.12.006.

[21] Y.E. Kalay, L.S. Chumbley, I.E. Anderson, Characterization of a marginal glass former alloy solidified in gas atomized powders, Materials Science and Engineering A. 490 (2008) 72–80. https://doi.org/10.1016/j.msea.2008.02.032.

[22] N. Wang, Y.E. Kalay, R. Trivedi, Eutectic-to-metallic glass transition in the Al-Sm system, Acta Mater. 59 (2011) 6604–6619. https://doi.org/10.1016/j.actamat.2011.07.015.

[23] Y.E. Kalay, C. Yeager, L.S. Chumbley, M.J. Kramer, I.E. Anderson, Initial crystallization in a nanostructured Al-Sm rare earth alloy, J Non Cryst Solids. 356 (2010) 1416–1424. https://doi.org/10.1016/j.jnoncrysol.2010.05.005.

[24] Y.E. Kalay, L.S. Chumbley, M.J. Kramer, I.E. Anderson, Local structure in marginal glass forming Al-Sm alloy, Intermetallics (Barking). 18 (2010) 1676–1682. https://doi.org/10.1016/j.intermet.2010.05.005.

[25] Y.E. Kalay, I. Kalay, J. Hwang, P.M. Voyles, M.J. Kramer, Local chemical and topological order in Al-Tb and its role in controlling nanocrystal formation, Acta Mater. 60 (2012) 994–1003. https://doi.org/10.1016/j.actamat.2011.11.008.

[26] T. Demirtaş, Y.E. Kalay, Kinetics of fcc-Al nanocrystallization in Al90Tb10 metallic glass, J Non Cryst Solids. 378 (2013) 71–78. https://doi.org/10.1016/j.jnoncrysol.2013.06.020.

[27] J. Schroers, R. Busch, A. Masuhr, W.L. Johnson, Continuous refinement of the microstructure during crystallization of supercooled Zr41Ti14Cu12Ni10Be23 melts, Appl Phys Lett. 74 (1999) 2806–2808. https://doi.org/10.1063/1.124020.

[28] M. Ovun, M.J. Kramer, Y.E. Kalay, Structural modeling of liquid and amorphous Al91Tb9by Monte Carlo simulations, J Non Cryst Solids. 405 (2014) 27–32. https://doi.org/10.1016/j.jnoncrysol.2014.08.037.

[29] C. Yildirim, M. Kutsal, R.T. Ott, M.F. Besser, M.J. Kramer, Y.E. Kalay, The role of amorphous precursor in phase selection hierarchy in marginal metallic glasses, Mater Des. 112 (2016) 479–484. https://doi.org/10.1016/j.matdes.2016.09.060.

[30] T.H. Ulucan, I. Kalay, Y.E. Kalay, The Anomalous Nucleation in Al-Tb Metallic Glasses, Metall Mater Trans A Phys Metall Mater Sci. 52 (2021) 700–710. https://doi.org/10.1007/s11661-020-06111-6.

[31] C. Okuyucu, B. Kaygusuz, C. Işıksaçan, O. Meydanoğlu, A. Motallebzadeh, S. Özerinç, Y.E. Kalay, Al-Sm Alloys Under Far-From-Equilibrium Conditions, in: L. Perander (Ed.), Light Metals 2021, Springer International Publishing, Cham, 2021: pp. 85–91. https://doi.org/10.1007/978-3-030-65396-5_13.

[32] D. Sariturk, Y.E. Kalay, A Molecular Dynamics Study on the Local Structure of Al 90 Sm 10 Marginal Metallic Glass and Liquid, Metallurgical and Materials Transactions A. 54 (2023). https://doi.org/10.1007/s11661-023-07015-x.

[33] P. Villars, K. Cenzual, Pearson's Crystal Data - Crystal Structure Database for Inorganic Compounds (on DVD), Release 2016/17, (2016).

[34] C. Boudias, D. Monceau, CaRIne Crystallography v3.1, (n.d.).

[35] A. Boultif, D. Louër, Powder pattern indexing with the dichotomy method, J Appl Crystallogr. 37 (2004). https://doi.org/10.1107/S0021889804014876.

[36] B.R. Tull, J.E. Carey, M.A. Sheehy, C. Friend, E. Mazur, Formation of silicon nanoparticles and web-like aggregates by femtosecond laser ablation in a background gas, Appl Phys A Mater Sci Process. 83 (2006). https://doi.org/10.1007/s00339-006-3502-7.

[37] H.E. Kissinger, Reaction Kinetics in Differential Thermal Analysis, Anal Chem. 29 (1957) 1702–1706. https://doi.org/10.1021/AC60131A045/ASSET/AC60131A045.FP.PNG_V0 3.

[38] A.A. Soliman, Derivation of the Kissinger equation for non-isothermal glass transition peaks, J Therm Anal Calorim. 89 (2007) 389–392. https://doi.org/10.1007/S10973-006-8158-1/METRICS.

[39] T. Ozawa, A New Method of Analyzing Thermogravimetric Data, Bull Chem Soc Jpn. 38 (1965) 1881–1886. https://doi.org/10.1246/BCSJ.38.1881.

[40] X. Zhang, Applications of kinetic methods in thermal analysis: A review, Engineered Science. 14 (2021) 1–13. https://doi.org/10.30919/ES8D1132.

[41] C. Yıldırım, Structural And Dynamical Evolution Of Nanocrystals, Middle East Technical University, 2013.

[42] E. Erdal, The Effects Of Chemical Short-Range Order On Crystallization Pathway In Ternary Marginal Glass Forming Alloys, Middle East Technical University, 2021.

[43] S.L. Robinson, O.D. Sherby, Activation energy for lattice self-diffusion in aluminum, Physica Status Solidi (a). 1 (1970). https://doi.org/10.1002/pssa.19700010333.

[44] Tolga Han Ulucan, Local Structure and Chemistry in Marginal Glass Forming Alloys, Middle East Technical University, 2020.

[45] D.R. Allen, J.C. Foley, J.H. Perepezko, Nanocrystal development during primary crystallization of amorphous alloys, Acta Mater. 46 (1998) 431–440. https://doi.org/10.1016/S1359-6454(97)00279-6.

[46] X. Wu, S. Lan, Z. Wu, X. Wei, Y. Ren, H.Y. Tsang, X. Wang, Multiscale structures of Zr-based binary metallic glasses and the correlation with glass forming ability, Progress in Natural Science: Materials International. 27 (2017) 482–486. https://doi.org/10.1016/J.PNSC.2017.08.008.

[47] N. Wang, Y.E. Kalay, R. Trivedi, Eutectic-to-metallic glass transition in the Al-Sm system, Acta Mater. 59 (2011) 6604–6619. https://doi.org/10.1016/j.actamat.2011.07.015.

[48] G. Wilde, H. Sieber, J.H. Perepezko, Glass formation in Al-rich Al-Sm alloys during solid state processing at ambient temperature, J Non Cryst Solids. 250-252 (II) (1999) 621–625. https://doi.org/10.1016/S0022-3093(99)00147-7.

[49] W.G. Stratton, J. Hamann, J.H. Perepezko, P.M. Voyles, X. Mao, S. V. Khare, Aluminum nanoscale order in amorphous Al92 Sm8 measured by fluctuation electron microscopy, Appl Phys Lett. 86 (2005) 1–3. https://doi.org/10.1063/1.1897830.

[50] K.K. Sahu, N.A. Mauro, L. Longstreth-Spoor, D. Saha, Z. Nussinov, M.K. Miller, K.F. Kelton, Phase separation mediated devitrification of Al88Y 7Fe5 glasses, Acta Mater. 58 (2010) 4199–4206. https://doi.org/10.1016/j.actamat.2010.04.011.

[51] K.F. Kelton, Time-dependent nucleation in partitioning transformations, Acta Mater. 48 (2000) 1967–1980. https://doi.org/10.1016/S1359-6454(99)00455-3.

[52] I. Lobzenko, Y. Shiihara, T. Iwashita, T. Egami, Shear Softening in a Metallic Glass: First-Principles Local-Stress Analysis, Phys Rev Lett. 124 (2020). https://doi.org/10.1103/PhysRevLett.124.085503.

[53] H. Guo, P.F. Yan, Y.B. Wang, J. Tan, Z.F. Zhang, M.L. Sui, E. Ma, Tensile ductility and necking of metallic glass, Nat Mater. 6 (2007) 735–739. https://doi.org/10.1038/nmat1984.

[54] D.C. Hofmann, J.Y. Suh, A. Wiest, G. Duan, M.L. Lind, M.D. Demetriou, W.L. Johnson, Designing metallic glass matrix composites with high toughness and tensile ductility, Nature. 451 (2008) 1085–1089. https://doi.org/10.1038/nature06598.

[55] A. Inoue, A. Takeuchi, Recent development and application products of bulk glassy alloys, Acta Mater. 59 (2011) 2243–2267. https://doi.org/10.1016/j.actamat.2010.11.027.

[56] C. Suryanarayana, A. Inoue, Metallic Glasses, in: Ullmann's Encyclopedia of Industrial Chemistry, Wiley-VCH Verlag GmbH & Co. KGaA, Weinheim, Germany, 2012. https://doi.org/10.1002/14356007.a16_335.pub2.

[57] W.H. Wang, The elastic properties, elastic models and elastic perspectives of metallic glasses, Prog Mater Sci. 57 (2012) 487–656. https://doi.org/10.1016/j.pmatsci.2011.07.001.

[58] Y. Shen, J.H. Perepezko, Al-based amorphous alloys: Glass-forming ability, crystallization behavior and effects of minor alloying additions, J Alloys Compd. 707 (2017) 3–11. https://doi.org/10.1016/J.JALLCOM.2016.11.079.

[59] T. Egami, T. Iwashita, W. Dmowski, Mechanical Properties of Metallic Glasses, Metals 2013, Vol. 3, Pages 77-113. 3 (2013) 77–113. https://doi.org/10.3390/MET3010077.

[60] M. Seleznev, A. Vinogradov, Shear Bands Topology in the Deformed Bulk Metallic Glasses, Metals (Basel). 10 (2020) 374. https://doi.org/10.3390/met10030374.

[61] R.T. Qu, Z.Q. Liu, G. Wang, Z.F. Zhang, Progressive shear band propagation in metallic glasses under compression, Acta Mater. 91 (2015) 19–33. https://doi.org/10.1016/j.actamat.2015.03.026.

[62] S.X. Song, T.G. Nieh, Direct measurements of shear band propagation in metallic glasses - An overview, Intermetallics (Barking). 19 (2011) 1968–1977. https://doi.org/10.1016/j.intermet.2011.06.018.

[63] B. Hou, M. Zhao, P. Yang, Y. Li, Capture of shear crack propagation in metallic glass by high-speed camera and in-situ SEM, in: Key Eng Mater, Trans Tech Publications Ltd, 2015: pp. 162–170. https://doi.org/10.4028/www.scientific.net/KEM.626.162.

[64] W.H. Jiang, F.E. Pinkerton, M. Atzmon, Mechanical behavior of shear bands and the effect of their relaxation in a rolled amorphous Al-based alloy, Acta Mater. 53 (2005) 3469–3477. https://doi.org/10.1016/J.ACTAMAT.2005.04.003.

[65] Z. Yan, J. Yan, Y. Hu, S. Dang, Crystallization in Zr60Al15Ni25 bulk metallic glass subjected to rolling at room temperature, Sci China Technol Sci. 53 (2010) 278–283. https://doi.org/10.1007/S11431-009-0315-X.

[66] C.A. Pampillo, Localized shear deformation in a glassy metal, Scripta Metallurgica. 6 (1972) 915–917. https://doi.org/10.1016/0036-9748(72)90144-5.

[67] J. Li, F. Spaepen, T.C. Hufnagel, Nanometre-scale defects in shear bands in a metallic glass, Http://Dx.Doi.Org/10.1080/01418610208240056. 82 (2009) 2623–2630. https://doi.org/10.1080/01418610208240056.

[68] W.J. Wright, T.C. Hufnagel, W.D. Nix, Free volume coalescence and void formation in shear bands in metallic glass, J Appl Phys. 93 (2003) 1432. https://doi.org/10.1063/1.1531212.

[69] W.H. Jiang, F.E. Pinkerton, M. Atzmon, Deformation-induced nanocrystallization: A comparison of two amorphous Al-based alloys, Journal of Materials Research 2005 20:3. 20 (2005) 696–702. https://doi.org/10.1557/JMR.2005.0090.

[70] H.J. Chang, D.H. Kim, Y.M. Kim, Y.J. Kim, K. Chattopadhyay, On the origin of nanocrystals in the shear band in a quasicrystal forming bulk metallic glass Ti40Zr29Cu9Ni8Be14, Scr Mater. 55 (2006) 509–512. https://doi.org/10.1016/J.SCRIPTAMAT.2006.05.037.

[71] Z.J. Yan, J. Yan, Y. Hu, W.X. Hao, Microstructure evolution of Zr65Al7.5Cu12.5Ni10Ag5 bulk metallic glass due to rolling and its influence on the thermal stability, J Alloys Compd. 513 (2012) 75–79. https://doi.org/10.1016/J.JALLCOM.2011.09.083.

[72] Z.J. Yan, J. Yan, L.F. Tuo, Y. Hu, S.E. Dang, Microstructure evolution of Zr60Al15Ni25 bulk metallic glass subjected to rolling at room temperature, J Alloys Compd. 504 (2010) S251–S255. https://doi.org/10.1016/J.JALLCOM.2010.04.130.

[73] W.H. Jiang, M. Atzmon, The effect of compression and tension on shear-band structure and nanocrystallization in amorphous Al90Fe5Gd5: a high-resolution transmission electron microscopy study, Acta Mater. 51 (2003) 4095–4105. https://doi.org/10.1016/S1359-6454(03)00229-5.

[74] A. Inoue, T. Zhang, K. Kita, T. Masumoto, Mechanical Strengths, Thermal Stability and Electrical Resistivity of Aluminum-Rare Earth Metal Binary Amorphous Alloys, Materials Transactions, JIM. 30 (1989) 870–877. https://doi.org/10.2320/MATERTRANS1989.30.870.

[75] H. Gao, Y. Huang, Geometrically necessary dislocation and size-dependent plasticity, Scr Mater. 48 (2003) 113–118. https://doi.org/10.1016/S1359-6462(02)00329-9.

[76] J. Il Jang, B.G. Yoo, Y.J. Kim, J.H. Oh, I.C. Choi, H. Bei, Indentation size effect in bulk metallic glass, Scr Mater. 64 (2011) 753–756. https://doi.org/10.1016/J.SCRIPTAMAT.2010.12.036.

[77] J.P. Chu, J.S.C. Jang, J.C. Huang, H.S. Chou, Y. Yang, J.C. Ye, Y.C. Wang, J.W. Lee, F.X. Liu, P.K. Liaw, Y.C. Chen, C.M. Lee, C.L. Li, C. Rullyani, Thin film metallic glasses: Unique properties and potential applications, Thin Solid Films. 520 (2012) 5097–5122. https://doi.org/10.1016/J.TSF.2012.03.092.

[78] M. Liu, C. Lu, K.A. Tieu, C.T. Peng, C. Kong, A combined experimental-numerical approach for determining mechanical properties of aluminum subjects to nanoindentation, Scientific Reports 2015 5:1. 5 (2015) 1–16. https://doi.org/10.1038/srep15072.

[79] D. Tabor, The Hardness of Metals, OUP Oxford, 2000.

[80] M. Abboud, S. Özerinç, Size-independent strength of amorphous-HCP crystalline metallic nanolayers, J Mater Res. 34 (2019) 2275–2284. https://doi.org/10.1557/JMR.2019.74/FIGURES/5.

[81] M. Abboud, A. Motallebzadeh, Ö. Duygulu, R. Maaß, S. Özerinç, Microstructure and nanomechanical behavior of sputtered CuNb thin films, Intermetallics (Barking). 136 (2021) 107249. https://doi.org/10.1016/J.INTERMET.2021.107249.

[82] R. Maaß, J.F. Löffler, Shear-Band Dynamics in Metallic Glasses, Adv Funct Mater. 25 (2015) 2353–2368. https://doi.org/10.1002/ADFM.201404223.

[83] K. Wang, T. Fujita, Y.Q. Zeng, N. Nishiyama, A. Inoue, M.W. Chen, Micromechanisms of serrated flow in a Ni50Pd30P20 bulk metallic glass with a large compression plasticity, Acta Mater. 56 (2008) 2834–2842. https://doi.org/10.1016/J.ACTAMAT.2008.02.015.

[84] S.S. Kulkarni, Adiabatic Shear Band Formation in Metallic Glasses, Metallic Glasses. (2019). https://doi.org/10.5772/INTECHOPEN.87437.

[85] A. Kawashima, Y. Zeng, G. Xie, N. Nishiyama, A. Inoue, Microstructure in a Ni60Pd20P17B3 bulk metallic glass compressively fractured at cryogenic temperature, Materials Science and Engineering: A. 528 (2010) 391–396. https://doi.org/10.1016/J.MSEA.2010.09.029.

[86] J. juan Liu, Q. Wang, K. Sun, S. Gravier, J. jacque Blandin, B. Sun, J. Lu, Serrated plastic flow behavior and microstructure in a Zr-based bulk metallic glass processed by surface mechanical attrition treatment, Journal of Iron and Steel Research, International. 21 (2017) 175–182.

[87] Y. Shao, K. Yao, M. Li, X. Liu, Two-zone heterogeneous structure within shear bands of a bulk metallic glass, Appl Phys Lett. 103 (2013) 171901. https://doi.org/10.1063/1.4826117.

[88] J. Fan, W. Rao, J. Qiao, P.K. Liaw, D. Şopu, D. Kiener, J. Eckert, G. Kang, Y. Wu, Achieving work hardening by forming boundaries on the nanoscale in a Ti-based metallic glass matrix composite, J Mater Sci Technol. 50 (2020) 192–203. https://doi.org/10.1016/J.JMST.2020.02.036.

[89] M. Slemrod, The Becker-Döring Equations, in: M. Bellomo Nicola and Pulvirenti (Ed.), Modeling in Applied Sciences: A Kinetic Theory Approach, Birkhäuser Boston, Boston, MA, 2000: pp. 149–171. https://doi.org/10.1007/978-1-4612-0513-5_5.

[90] D.B. Duncan, A.R. Soheili, Approximating the Becker–Döring cluster equations, Applied Numerical Mathematics. 37 (2001) 1–29. https://doi.org/https://doi.org/10.1016/S0168-9274(00)00020-9.